SLAC-PUB-2428
November 1979
(T/E)

LEPTON NUCLEON SCATTERING*

W. B. ATWOOD

Stanford Linear Accelerator Center
Stanford University, Stanford, California 94305

Lectures

at

the

SLAC Summer Institute on Particle Physics:

Quantum Chromodynamics

at

Stanford, California

July 9 - 20, 1979

---

* Work supported by the Department of Energy under contract number DE-AC03-76SF00515.

TABLE OF CONTENTS

INTRODUCTION

In our attempt to understand the strong interactions between hadrons, we have inferred a complicated substructure within the particles that we actually observe in our laboratories. Over the years, the understanding of this physics evolved into a constituent model of hadrons. We have not yet been able to detect the constituents by themselves, but most of the observed phenomena involving hadrons can be explained by their presence. The constituents I am referring to are, of course, quarks. The quark model has had particles added to it whose properties would determine how quarks interact with each other. These exchanged particles are called gluons. These ideas (and more) have now been formalized into the theory called Quantum Chromodynamics (QCD).

In the following discussions, some predictions depend only on the existance of point-like constituents inside the hadrons. At a higher level of sophistication some predictions depend on the quark make-up of the hadrons. At a still higher level of sophistication, some predictions depend on the gluon coupling of quarks. At the highest level, the predictions depend on the color structure of the theory ("full blown" QCD). I have endeavored to identify each of these cases as they occur, so that the reader can gain a clearer picture of what is in one case a test of QCD and what is in another, merely a test of, say, the coupling of quarks by vector gluons. These concepts form a hierarchy: each successive level is an elaboration of the previous one and contains all of its general features:

HIERARCHY OF THEORETICAL MODELS

Constituent picture - Nucleons are made up of "hard" structureless constituents, from which the lepton probes scatter in deep inelastic processes.

Quark model - The constituents are quarks! The character of nucleons at high energy is determined by the momentum distribution of the quarks inside.

Quarks with gluons - The way the quarks interact is via (vector) gluon exchange. Evidence of the gluon propagator should be visible in some processes.

Quantum Chromodynamics - Quark and gluon couplings are determined by a colored gauge field theory. Vertex renormalization results in a Q^2 dependence of the coupling α_s.

The subject of these lectures is Lepton-Nucleon "Inclusive" Scattering. I will briefly review some of the experiments which provide us with data in the next section of these notes. A discussion of the constituent model of the nucleon and the contribution of various types of experiments follows in Sec. 2.1. In Sec. 2.2., data from the experiments are compared and some simple predictions of the quark model are covered. In Sec. 3. some of the fundamental notions behind quantum chromodynamics are reviewed. The subsequent sections cover detailed tests of QCD. Some well known tests (like anomalous dimensions in Sec. 6) and others which are perhaps less well known (like elastic scattering in Sec. 5, or the ratio of the longitudinal to transverse total photoabsorption cross sections in Sec. 4) are discussed.

My intention in these lectures is to provide the high energy experimental physicist with a better understanding of lepton-nucleon scattering experiments in the context of contemporary theoretical ideas. New results and discoveries will be left to the topical conference which follows the summer school. I hope my lectures will set the stage for a better appreciation of what these new discoveries and results mean.

1. THE EXPERIMENTS

In this Section, I discuss the fodder for all the theoretical ruminations... the experiments! I shall briefly review three of the numerous lepton-nucleon scattering experiments. I have three reasons for doing this. First, I am an experimenter and I couldn't possibly give a lecture which doesn't mention nuts and bolts at least once. Second, I want to show the origin of some of the data that is considered in Sec. 2.2. - Sec. 6. Third, by choosing one electron, one muon and one neutrino experiment, I can display the sensitivity of the various experiments and discuss their systematic errors.

I begin with a discussion of the nature of experimental accuracy and errors and then move on to discuss the specific experiments which form a "data base" for these lectures. I then make comparisons among the experiments with respect to their statistical significance and systematic errors.

1.1. Accuracy and Quoted Errors in Counting Experiments

I will introduce the discussion of deep inelastic lepton scattering experiments by making a few remarks on the statistical and systematic errors in such experiments.

Statistical Accuracy

The statistical precision of a measurement is determined by the number of events in the given kinematic bin. Recall that the statistical error is proportional to the $\sqrt{\text{counts}}$ and hence the relative error changes as $1/\sqrt{\text{counts}}$. The "counts" for an experiment of this type can be represented by

$$\text{counts} = \int \mathscr{L}\, dt \cdot \frac{d\sigma}{d\Omega dE} \cdot d\Omega dE \cdot \varepsilon \qquad (1)$$

$\mathscr{L}$ is the Luminosity (=number of beam particles * number of target nucleons $/(\text{cm}^2 - \text{sec})$). $\frac{d\sigma}{d\Omega dE}$ is the probability of having a scattered particle within the solid angle ($d\Omega$) and the energy acceptance (dE) of the apparatus. ε is the probability that the detector responds in such a way as to make the event identifiable.

For some regions of Ω and E, the cross section becomes very small thus placing an overriding limit on the statistical accuracy of an experiment.

Only by a proportionate increase in luminosity can we hope to obtain a viable result in such regions.

Systematic Accuracy

Time and money eventually result in acceptably small statistical errors for most experiments, but understanding and controlling systematic errors can often be much more difficult. Major sources of such errors are encountered in the measurement of $\mathscr{L}$, $d\Omega dE$ and ε. Verification of the measurements by means of experimental cross checks is usually more reliable than corrections calculated deep in the bowels of a Monte Carlo computer program. For example, in inclusive scattering experiments at SLAC, the intensity of incident electrons is measured using two, non-intercepting toroid flux monitors. The toroids have been calibrated against a Farady cup and a standard capacitor pulse. The spectrometer acceptances and optics are measured by using the primary electron beam as a probe to trace the electron trajectories directly. And so on... The reproducibility of these kinds of experimental cross checks leads to an overall systematic error estimate in the SLAC measurements of about 5%, coming mostly from uncertainties in $\mathscr{L}$ and $d\Omega dE$.⁽¹⁾

The systematic errors entering in the determination of ε can also be significant. Often the information produced by the equipment is sufficiently imprecise to allow misidentification so that some "good" events may be eliminated while some "background" events are retained in the sample. This "grey area" is usually corrected for by using statistical subtraction techniques. The associated systematic errors will be small provided these corrections are small. Therefore, experimenters must take care to design the experiments to have a large signal-to-noise ratio.

Calculated corrections made to the data can also be a source of systematic error. Two such corrections in all deep inelastic experiments are: (1) radiative corrections, and (2) Fermi motion corrections (except for H_2 targets). For electron scattering, radiative effects can be large (typically of the order of 20%). For the muon, the radiative effects are 4 - 5 times less than those for electrons through most of the kinematic ranges covered by present experiments. But near the extremes of the range, muon radiative corrections do become comparable to the largest corrections that occur in the published electron scattering data.(2)

Radiative corrections are usually made only for the incoming and outgoing lepton. No corrections are made for target radiation which (especially in the case of experiments involving muons) could be comparable in size. The radiative correction procedures used are themselves only approximations to "exact" lowest order QED calculations.(3) Exact calculations are still much too costly in computer time. The approximation procedures have been spot checked for accuracy at many kinematic points using the lowest order QED formulas. Data points which have a large radiative correction should be used with caution. These data points are usually located at the extremes of the kinematic region covered in an experiment.

Fermi motion effects exist in all targets except hydrogen but this correction is significant only near threshold. The Fermi motion effects are less well understood than the radiative correction and controversy exists as to the correct method to employ.(4) Fortunately these effects are small and have little influence on the important results to be discussed in these notes.

Quoted Errors

Properly accounting for systematic errors when comparing data with theory is difficult. Some systematic errors are uncorrelated data point to data point while others affect only the overall normalization. A common procedure is to combine systematic errors with the statistical errors in some fashion and then treat the resulting errors as if they were purely statistical. Then, for example, when integrals over the data are calculated or global fits are made, the systematic errors "disappear" as $1/\sqrt{\text{No.-of-data points}}$ used and the correlated errors are not properly accounted for. In this way experimental data with a ±5% overall normalization can be used to produce results with a much smaller (and inaccurate) error. In general, a simple, practical method to treat systematic errors does not exist. Different experimental groups have adopted different procedures, and serious students of the data must familiarize themselves with these procedures before combining data for comparisons with theory or other experiments.

1.2. Three Experiments

The three experiments are: (1) the electron scattering experiments performed here at SLAC,(1) (2) the CHIO collaboration's muon scattering experiments at Fermilab,(2) and (3) the CDHS collaboration's neutrino experiments at CERN.(5) Fig. 1 is a sketch of the three experimental setups.

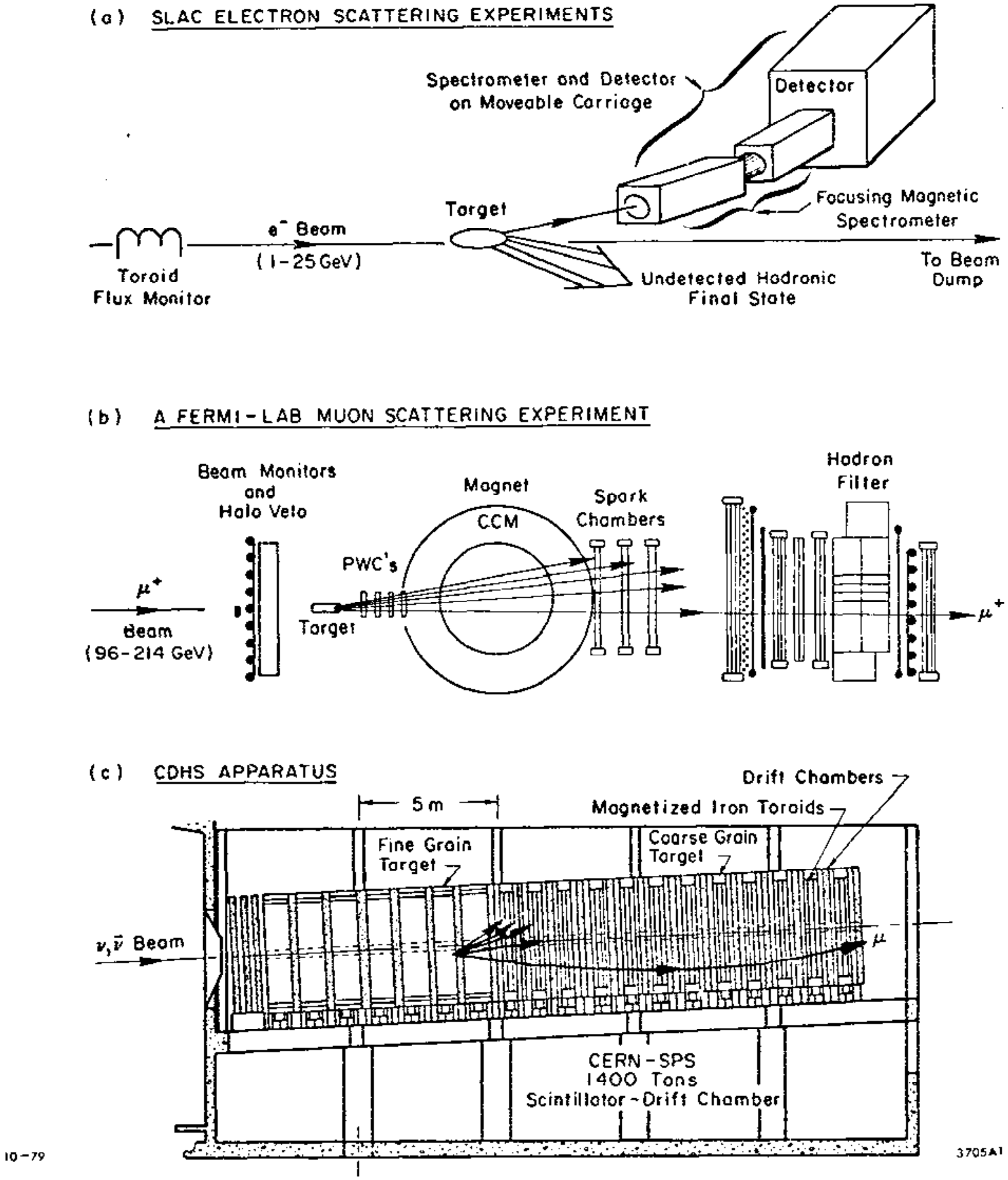

Figure 1. Experiment Setups: a) SLAC, b) CHIO, c) CDHS.

Electron - Proton Scattering at SLAC

A schematic picture of the electron scattering experiments is shown in Fig. 1a. The electron beam (energies 3-24 GeV) from the SLAC linac is momentum analyzed and focused on a target located in End Station A. The setting error in the incident energy is ± 0.1%. Upstream of the target are two precision non-intercepting, toroidal flux monitors which have been independently calibrated against a Faraday cup. In view of these calibration checks we believe the toroids measure the number of incident electrons with an absolute precision of slightly better than 1%.

Liquid hydrogen and liquid deuterium targets of various lengths (7 cm to 30 cm) have been used in the SLAC experiments. The number of nucleons/cm^2 is known to ± 1%. The error comes mainly from uncertainties in determining the density of the liquids. Most of the electron beam passes through the target and into a beam dump behind the end station. A few electrons scatter in the target, lose a fraction of their energy (y), and are deflected through some angle (θ). The scattered electrons may be detected by one of three focusing magnetic spectrometers making up the SLAC spectrometer facility. These spectrometers are located on rails to allow measurements over a range of scattering angles.

The acceptances of the spectrometers (both dΩ and dE) are probably the least understood quantities used in calculating cross sections. The acceptances are determined by using Monte Carlo techniques and magnetic models of the spectrometers. The results of such calculations have been experimentally cross-checked using the primary electron beam as a probe of electron trajectories. Other experimental checks include the "floating wire" technique used to measure the optics of the 1.6 GeV spectrometer and "jail bar" runs used for the 20 GeV spectrometer. In the latter case masks are used to establish patterns in the spatial distribution of electrons entering the spectrometer and the patterns are traced through the spectrometer (See M. Mestayer, Ph.D. Thesis, in Ref. 1). The agreement between the various determinations and comparisons between data taken with the same kinematics but with different spectrometers results in an estimated 1 - 5% systematic error.

Electrons scattered into the acceptances of the spectrometers are detected and identified using threshold gas Čerenkov counters, shower counters, and hodoscopes. The experimental challenge is to identify electrons in the presence of pions. The chance of a pion being identified as an electron is typically 1-in-10^4 to 1-in-10^5 and the electron detection efficiency is typically > 95%. Systematic errors of about 2% have been ascribed to identification of scattered electrons.

The analysis of the electron data requires the application of radiative corrections. These corrections typically range from -20% to +20% and are never larger than 30% for the presently published data. Errors enter this correction through misestimations of the actual radiators in the experiment (target walls, vacuum windows, etc.) as well as in approximations made in the (rather complex) calculation of the corrections themselves.

Because of the high intensity of the SLAC beam, counting rates for most of the attainable kinematic range are large. The many deep inelastic experiments performed at SLAC, accumulating more than 2,000 data points, have almost completely covered the deep inelastic region presently accessible at SLAC. Each data point represents hundreds (usually thousands) of events. The accuracy of the SLAC data is almost everywhere limited by systematic errors.

Muon - Proton Scattering at Fermilab - the CHIO Data

In Fig. 1 b. the setup of the CHIO collaboration is sketched.(4) A muon beam is created by allowing pions and kaons to decay and then absorbing any remaining hadrons in a Be filter. The phase space of the resulting beam is large: the diameter is approximately 4 cm; the angular divergence is ± 1.5 mrad; and the energy spread is approximately ± 2.5%. The trajectories of incident beam particles are individually measured by a system of multi-wire proportional chambers (MWPC's) designed to operate at high instantaneous rates. Since each beam particle is "tagged," the beam is in principle as well defined in position, energy, and angle as the electron beam used at SLAC. Intensities of up to 8×10^5 muons per pulse were used in these experiments.

Muon beams by their nature have large halo: for the experiment under discussion the halo muons illuminating the apparatus were approximately as numerous as the muons "in" the beam. But beam halo is a source of accidental triggers since a beam particle may traverse those portions of the apparatus designed to detect scattered muons. A veto of scintillators located in front of the target was used to suppress this background. The effects of both the fast veto and the (high rate) tagging system introduce dead times into the experiment, with consequent systematic errors.

The target cell in the CHIO experiments was 120 cm long, and 18 cm in diameter. To achieve acceptable statistical levels in the experiment, the target was an order of magnitude longer than targets used at SLAC. The Fermilab target cell could be filled with either hydrogen or deuterium to allow proton-neutron comparisons, but most of the data were measured using the hydrogen target.

Downstream of the target, eight MWPC's were used to establish the trajectories of emerging charged particles. The muons then passed through the large uniform field of the Chicago Cyclotron Magnet. After the magnet, spark chambers again measured particle trajectories so that the deflection of the particles in the 7.5 T-m of magnetic field could be determined. Various other detectors followed the spark chambers, the most important being the hadron filter. It consisted of 2.5 meters of steel (15 hadronic interaction lengths) followed by scintillators and spark chambers to identify penetrating tracks.

The solid angle and momentum acceptance were calculated using Monte Carlo computer simulations of the experimental apparatus. Inputs to the computer model were a set of detailed survey information and magnetic field measurements. The experiment does not include direct experimental cross checks of these calculations. The calculated acceptance varies from less than 10% to greater than 90% over the kinematic range covered. Over most of the range the acceptance is over 70%. The systematic error associated with the acceptance calculation is ± 8%.

Radiative corrections must be applied to these data before comparing with the predictions of theoretical models. As muons are some 210 times more massive than electrons such corrections are considerably smaller (typically < 5%). Fermi motion corrections also do not affect these data as these experiments had insufficient luminosity to make measurements in the threshold region where such effects are important.

The muon beam energies of up to 220 GeV used in the experiment potentially provided for a considerable extension of the kinematic range over that attainable at SLAC. But because of the low intensity of the muon beam and the diminishing cross sections at large scattering angles much of the available kinematic region had negligible numbers of events. Furthermore, many of the reported data points consisted of small numbers of events (less than 100) in large kinematic bins.

Neutrino - Nucleon Scattering at CERN - the CDHS Data

The apparatus of the CDHS collaboration at CERN (5) is shown in Fig. 1 c. A "narrowband" neutrino beam is produced by allowing a well focused beam of (momentum and sign selected) pions and kaons to decay. The remaining hadrons and decay muons are then absorbed and ranged out in over 300 meters of iron and earth shielding. This type of neutrino beam has an energy-angle correlation which results in an energy-radius correlation at the detector. Thus, at the detector, neutrinos at large distances from the beam center line have lower energy than those at smaller distance. This feature is very important for neutral current studies (although the latter are not discussed in these lectures). A level of about 10^8 neutrinos per pulse has been achieved in the narrowband beam at CERN. The flux of neutrinos is calculated from the measured flux of charged particles and the relative abundances of pions and kaons in the incident hadron beam. This measurement is cross checked by measuring the flux of decay muons and the total energy of the remaining hadrons in a calorimeter located at the end of the decay pipe. The largest systematic error in the experiment is associated with the flux measurement of incident neutrinos and is estimated to be around ± 6%.

The CDHS detector itself is a large target-calorimeter-spectrometer comprising toroidally magnetized iron plates interspersed with plastic scintillators and drift chambers. The useful target length is about 6500 gm/cm^2 which would correspond to a liquid hydrogen target almost 1 km long. The calorimetric properties of this device were investigated experimentally with a pion beam. It was determined to have energy resolution for hadrons of $\Delta E/E = 100\%/\sqrt{E(GeV)}$. The momentum resolution for outgoing muons is limited by multiple scattering in the iron and was found to be about 8% (independent of the muon's momentum). The muon momentum measurement and the calorimeter information from the hadron shower are combined to estimate the incident neutrino energy. An experimental cross check can be made by comparing this calculated neutrino energy to the neutrino energy derived from the interaction radius in the detector. The differences between the two methods for measuring the incident neutrino energy are well accounted for by the energy resolution of the detector and the imprecision in the energy-radius correlation due to the finite decay length (300 m) of the hadron beam.

The acceptance of the CDHS apparatus is quite uniform due to its large volume and is nearly 100% except for muons below about 15 GeV. In the analysis of the data the experimenters have placed cuts well inside the edges of the calorimeter to ensure containment of the hadronic showers. They also impose an effective muon momentum cut-off of about 7 GeV by requiring a penetrating muon track. Because of the flat acceptance and detector uniformity only small corrections need be made to the raw data. Thus, the systematic uncertainties associated with these corrections are small.

Muon identification and track reconstruction introduces perhaps the largest correction to these data. Occasionally the outgoing muon from a neutrino interaction will suffer a hard scatter producing a kink in the track, or worse, deflecting the track out of the spectrometer altogether. To estimate the reconstruction efficiency of the computer programs, a few thousand events were hand scanned and compared with the automated procedure. An efficiency of about 93% was observed. The systematic error associated with this correction will be small as the correction is only 7%.

Radiative and Fermi motion corrections are similar to those of the muon scattering experiments: radiative effects are only a few percent, and the experiment doesn't measure in the kinematic region where Fermi motion effects are important.

The energy of neutrinos in the narrow band beam were as high as ~200 GeV. The large neutrino flux and massive target (detector) resulted in large event rates for most of the kinematic region. At present, only data taken in 1977 have been published but much more data exist (taken in 1978) and are being analyzed.

1.3. Comparison of the Experiments

In Table I the three experiments discussed in the last three sections are compared vis-à-vis the quantities used to calculate the cross section in Eq. 1. The specific numbers in this Table represent typical values but may vary widely for some kinematics. The event rate for the electron scattering experiments at SLAC is the largest by an order of magnitude. This allows the SLAC experiments to have more sensitivity in regions where the cross section is small. The neutrino experiments have increasing sensitivity with increasing neutrino energy, as the cross sections are rising linearly with energy.(5) (The typical cross section quoted in Table I for CDHS is for 100 GeV incident neutrinos.) Both the electron and muon cross sections fall rapidly with increasing energy and so become less and less competitive with neutrinos. The estimated overall systematic errors quoted in the last row of Table I are my own estimates arrived at after reviewing these experiments. The various experimenters have tended to claim slightly better systematic errors. Let me emphasize again that only with the greatest care can one reduce the measurement errors on cross sections, or derived results such as moments, below these figures by combining results within experiments or combining data from different experiments. Even trends (i.e. relative changes in data) must be carefully examined if one wishes to eliminate the possibility that the trend is due to some systematic effect.

TABLE 1

Summary of Experiments

Item	Electrons at SLAC	Muons at Fermilab	Neutrinos at CERN
Luminosity (Hz/cm^2)	5×10^{37}	4×10^{29}	3×10^{35}
Cross Section (cm^2/GeV)	10^{-33}	10^{-32}	10^{-36}
$\frac{\Delta\Omega}{4\pi}$	0.0007	0.75	1.0
$\frac{\Delta E}{E}$	0.04	0.95	0.95
ε	> 0.95	0.70	0.93
Rates (Hz)	7	0.4	0.2
Overall Systematics (Main source)	0.05 (acceptance)	0.10 (acceptance & reconstruction)	0.10 (flux)

2. THE SIMPLE QUARK MODEL

2.1. Phenomenological Development

Constituent Scattering Picture

These lectures are concerned with the process shown schematically in Fig. 2. An interacting probe (electron, muon, or neutrino), ℓ, of energy E_o impinges on a nucleon. Usually nothing happens and the trajectory of the probe is unaffected. But occasionally an interaction occurs, scattering the probe particle to a final state, ℓ', of lower energy, E', and deflecting it through an angle, θ. The energy lost by the probe is

$$\nu = E_o - E' \ . \qquad (2)$$

This is also the energy transferred to the hadronic system (i.e. $\nu = E_{HAD}$). Denoting the initial nucleon by the four-vector p_μ and the 4-momentum transfer by

$$q_\mu = (\ell_\mu - \ell'_\mu) \qquad (3)$$

the mass of the final hadronic state can be written

$$W^2 = (p_\mu + q_\mu)^2 = p^2 + 2p\cdot q + q^2 \qquad (4)$$

where p^2 is the nucleon mass squared. Also we have

$$q^2 = -4E_oE' \sin^2(\theta/2) \equiv -Q^2 \qquad (5)$$

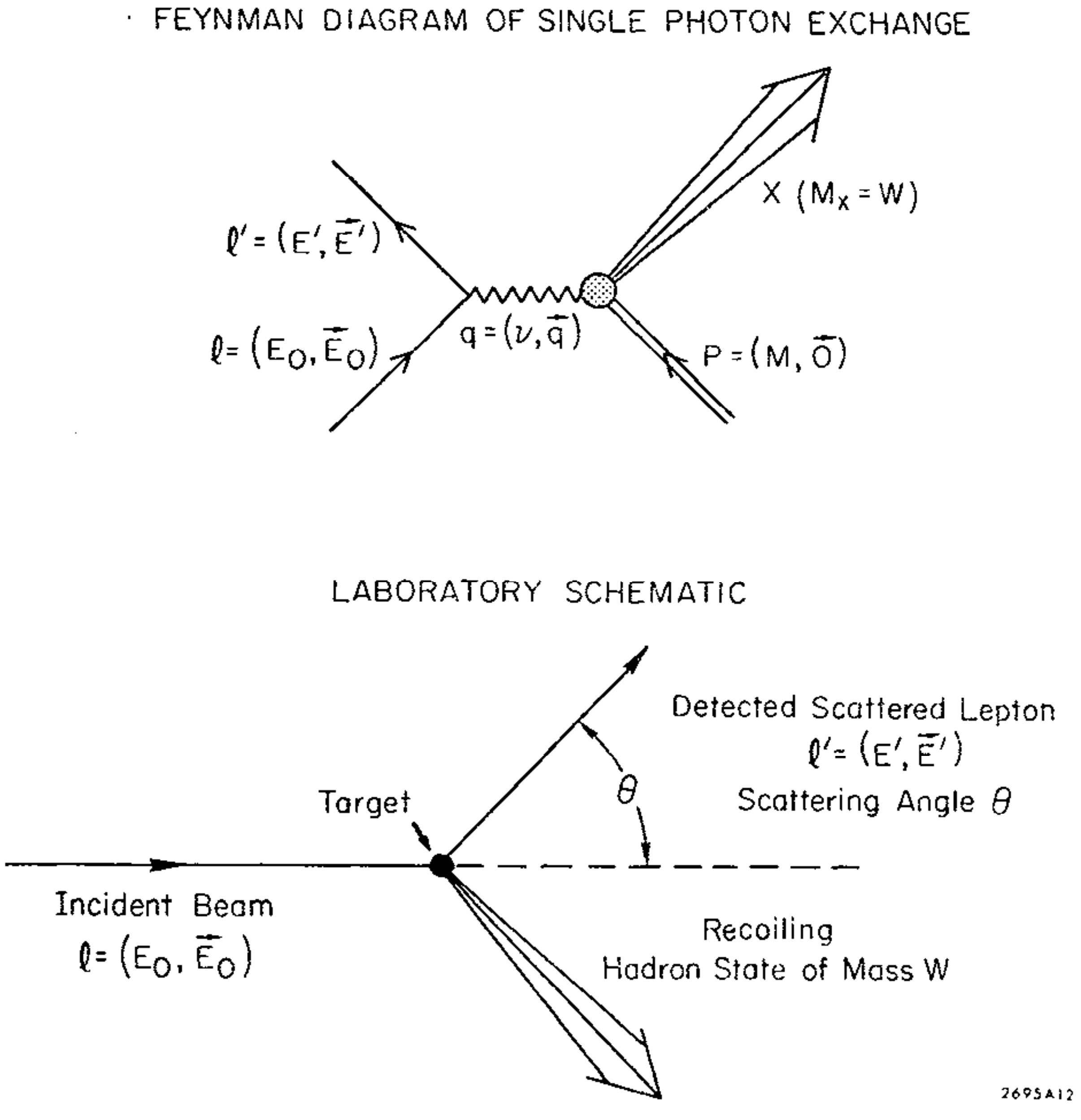

Figure 2. Inelastic lepton-hadron scattering. Definition of kinematic parameters.

and

$$p \cdot q = M\nu \tag{6}$$

Thus, in terms of the above parameters, Eq. 4. can be written

$$W^2 = M^2 + 2\,M\nu - Q^2 \ . \tag{7}$$

For elastic scattering the recoiling hadronic state is the target nucleon itself. This is perhaps the simplest final state and in this case

$$W^2 = M^2 \ , \tag{8}$$

thus

$$\frac{Q^2}{2M\nu} = 1 \ . \tag{9}$$

Now consider the nucleon as a system of interacting constituents. This situation is depicted in Fig. 3. An exchanged quantum, q, is absorbed by one of the constituents which carries a momentum fraction, ξ, of the nucleon. "Quasi" elastic scattering of the constituent would result in the constraint:

$$(\xi p_\mu + q_\mu)^2 = m^2 \tag{10}$$

where m is the mass of the constituent. Multiplying out this expression gives

$$\xi^2 M^2 + 2M\nu\xi - Q^2 = m^2 \tag{11.1}$$

or

$$\xi = \frac{Q^2 + m^2}{M(\nu + \sqrt{\nu^2 + Q^2 + m^2})} \ . \tag{11.2}$$

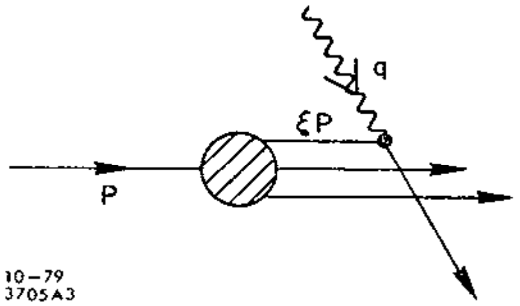

Figure 3. Constituent scattering of nucleon and photon.

If $\nu^2 >> Q^2 >> m^2$, then this becomes

$$\xi = \frac{Q^2}{2M\nu} \equiv x \, . \qquad (12)$$

This "scaling" variable, x, is the original variable introduced by Bjorken in the early days of the parton model and deep inelastic electron scattering(7). For elastic nucleon scattering x = 1, while final hadronic states of larger mass result in x values which are positive but less than 1. In this simple picture x can be interpreted as the fraction of the nucleon momentum carried by the particular constituent which interacts with the lepton probe.

The cross sections for lepton-nucleon scattering can be written as the product of a lepton scattering piece and nucleon structure functions. The constituent scattering picture described above results in structure functions which depend only on the scaling variable x in the limit of large Q^2 and ν. What has traditionally defined the energy scales of "large Q^2 and ν" has been the minimum energies at which the data are observed to "scale". Theory doesn't set values of Q^2 and ν above which scaling should occur but the popular prejudice was that this phenomenon should be observed for energies much greater than the proton mass. To everyone's surprise scaling was observed to begin for $Q^2 > 2$ GeV^2 and $\nu > 2.5$ GeV (which corresponds to $W > 2$ GeV). This discovery was dubbed "precocious scaling".

Why the word "scaling"? This is easy to understand. The value of a structure function (e.g. F_2), measured at Q^2 and ν, will be equal to the same structure function measured at other values of $Q^{2'}$ and ν', provided ν' is scaled along with $Q^{2'}$. That is:

$$\frac{Q^{2'}}{Q^2} = \frac{\nu'}{\nu} \tag{13}$$

implies that

$$F_2(Q^2,\nu) = F_2(Q^{2'},\nu') \tag{14}$$

An "improved" scaling variable which takes into account nucleon recoil effects is (Eq. 11.2 with $m^2 = 0$)

$$\xi = \frac{2x}{\left(1 + \sqrt{1 + \frac{4M^2x^2}{Q^2}}\right)} \tag{15}$$

This variable was first suggested in the light cone analysis of deep inelastic scattering (8) and is now commonly referred to as the Nachtmann variable. Many people believe that this is a more accurate scaling variable to use in the Q^2 and ν ranges currently available at various accelerators. At small values of x, the two choices of scaling variables are equivalent since the Q^2 dependence in ξ vanishes as x^2 (e.g. $\xi \simeq x(1 - \frac{M^2x^2}{Q^2} + ...)$). At large x and low Q^2, the $\frac{4M^2x^2}{Q^2}$ term in ξ (Eq. 15) can result in significant differences between the variables ξ and x. This in turn can effect the physical interpretation of the data as we will see later on.

Examples of Scaling in the Simple Quark Model

In the constituent picture of the nucleon, the structure functions become functions of a scaling variable, rather than functions of Q^2

and ν separately. The data exhibit a strong tendency in this direction as shown in Fig. 4 where the structure function F_2^{ep} , calculated from measured electron scattering cross sections off hydrogen, is plotted against the Bjorken variable, x. In general, F_2^{ep} would be a function of both ν and Q^2. We see that the data scale in this Q^2 range (of $2\ \text{GeV}^2 < Q^2 < 18\ \text{GeV}^2$) and this tends to support the constituent model. A careful observer will note, however, that there is a small but significant spread in the data for any specific value of x. This remaining Q^2 dependence of the data will be discussed in more detail in Sec. 3 - Sec. 6.

Some examples of constituent scattering are shown in Fig. 5 where structure functions are plotted against x. In elastic ep scattering (solid points) (one "constituent"), there is a sharp peak at $x = 1$. Here the electron scatters from the entire proton, which always has a momentum fraction of unity. The peak is broadened by experimental resolution and by radiative effects which produce a tail extending toward lower x values.

Quasi-elastic scattering from deuterium is illustrated by the open data points. The peak is due to scattering from the proton and neutron inside the deuterium nucleus. Each of these constituents has ~half the mass of the deuteron and therefore half the momentum fraction, so the peak appears at $x = \frac{1}{2}$. (Elastic ed scattering would appear at $x = 1$, as I have used the deuteron mass in place of nucleon mass in the definition of x.) This peak is broader than in the elastic nucleon case due to the Fermi motion of the nucleons in the deuteron.

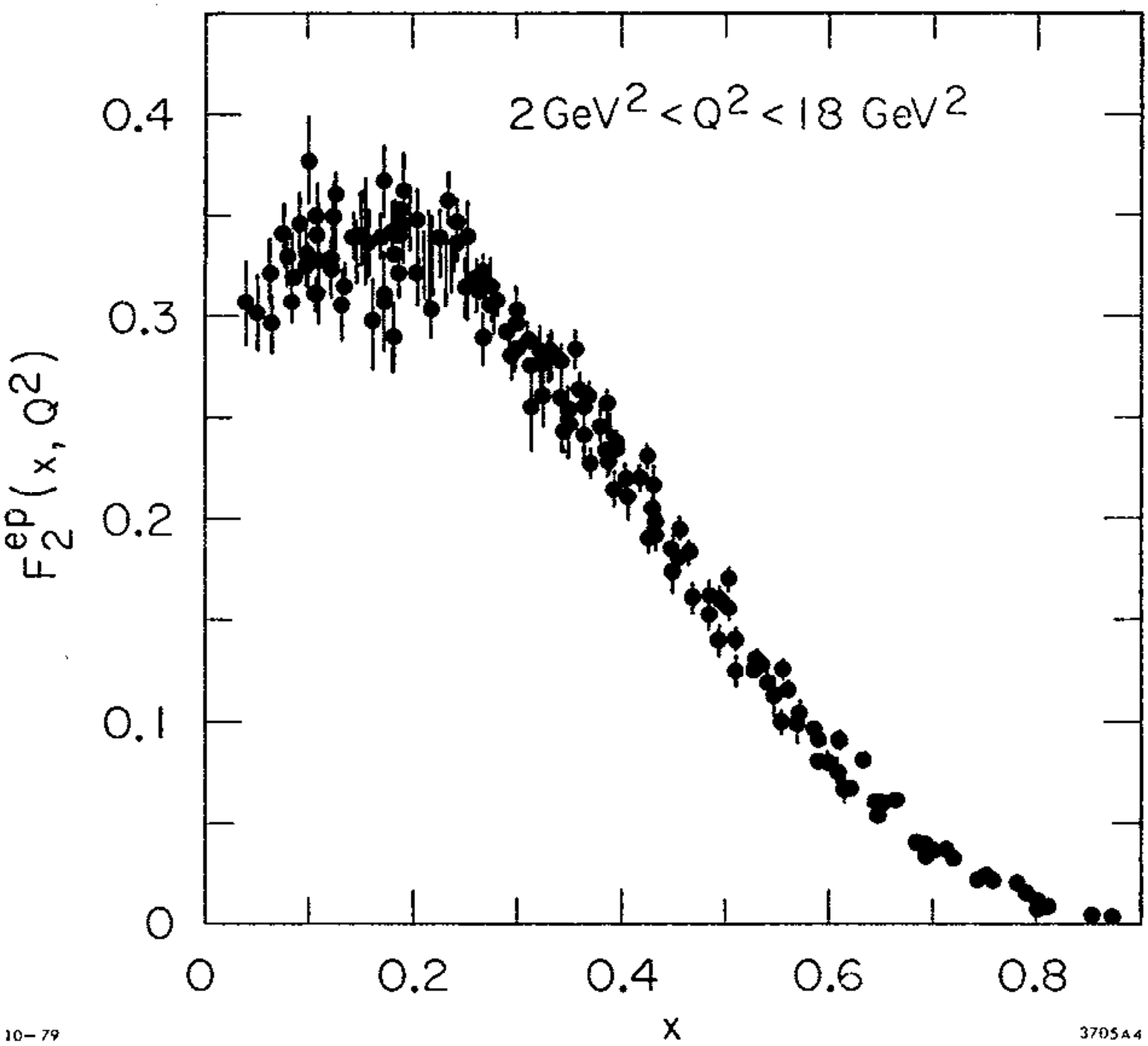

Figure 4. Proton structure function F_2 derived from electron scattering data.

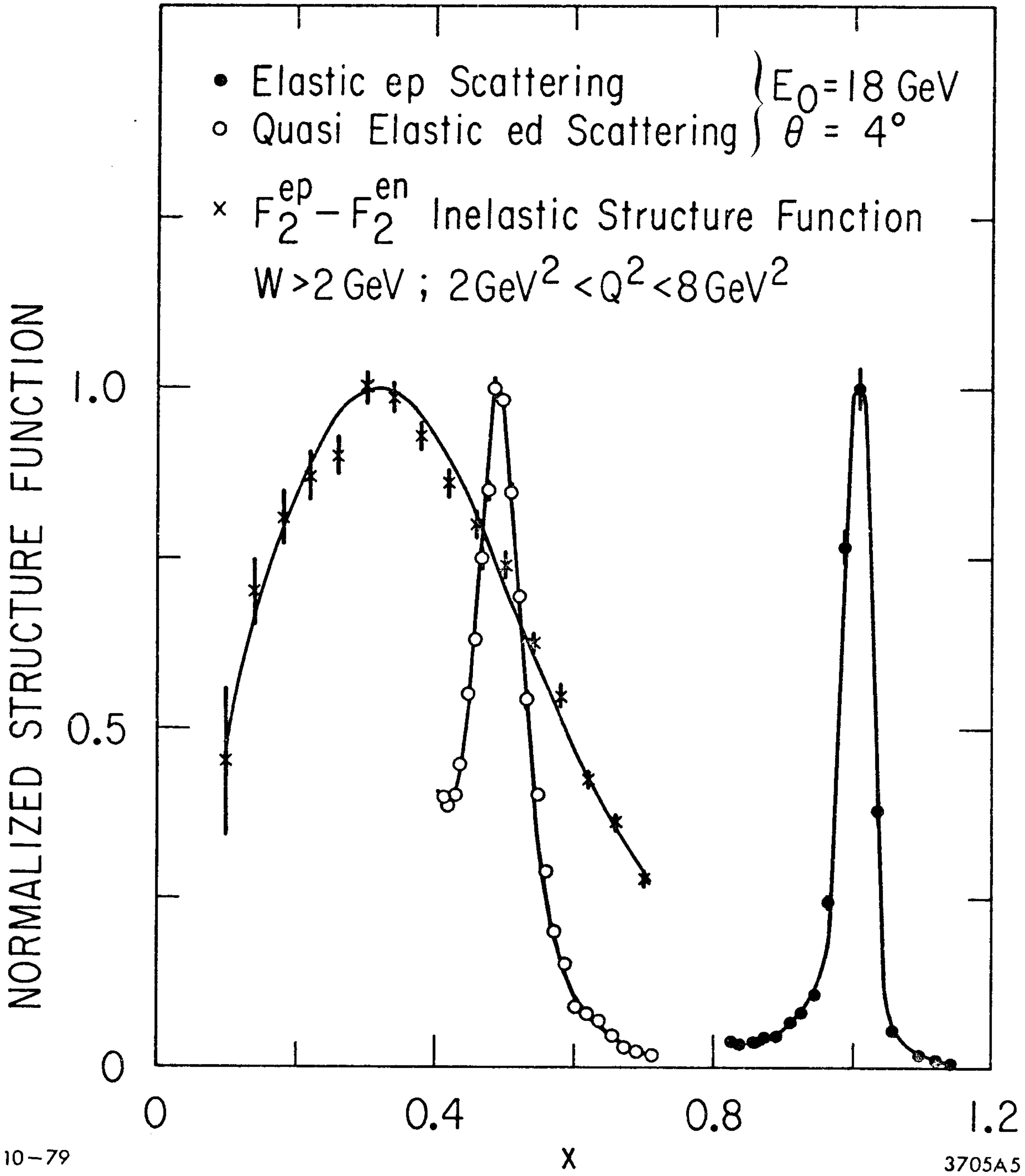

Figure 5. Structure functions as measured in three lepton – nucleon scattering experiments.

Finally, the data points given by "x 's" show the structure function $F_2^{ep} - F_2^{en}$ from inelastic electron scattering measurements. Here we see a fairly broad peak with a maximum near x = 1/3. This suggest an effective mass for the constituents of ~ 1/3 M. The broad peak suggests strong binding for these nucleon constituents. We interpret these data as quasi-elastic scattering from three constituents in the nucleon (the proton-neutron difference has been chosen to eliminate any contributions from q-$\bar{q}$ pairs in the nucleon).

The constituent picture is the basis for the simple quark model which gives quantitative predictions for the connections between charged lepton and neutrino/anti-neutrino deep inelastic experiments and e^+e^- annihilation. This model has been embellished to include particles through which quarks interact with each other and is now formalized into the theory called Quantum Chromodynamics, making possible a more sophisticated account of the interaction of not only leptons with quarks, but of the quarks with each other.

Kinematic Range of the Experiments

Before discussing the lepton-nucleon cross sections in more detail, some kinematics are in order. The variable

$$y = \frac{E_o - E'}{E_o} = \frac{\nu}{E_o} \qquad (16)$$

is often used in describing neutrino scattering because for elastic scattering at energies where E is much larger than the target mass,

$$(1-y) \simeq \frac{1 + \cos\theta_{cm}}{2} \quad . \tag{17}$$

As a consequence, simple angular distributions in the center of mass result in simple y dependences in the data for "quasi-elastic" quark-neutrino scattering.

The variables introduced so far (W^2, Q^2, x, y, and ν) can be related to each other in many ways. Two useful expressions are:

$$Q^2 = 2ME_o xy \tag{18.1}$$

and

$$\frac{1}{x} = 1 + \frac{W^2 - M^2}{Q^2} \quad . \tag{18.2}$$

The kinematics of each structure function data point can be specified by x and Q^2. On an x-Q^2 plot, Eq. 18.1 defines a family of curves for a given E_o and various values of y. Similarly, Eq. 18.2 defines curves of constant W. In Fig. 6, I have plotted the kinematic ranges of the three experiments in x versus $\ln(Q^2)$. Since the QCD theory suggests a deviation from scaling like $1/\ln(Q^2)$, I chose $\ln(Q^2)$ rather than Q^2 itself for the x axis. Where $W = M$ ($x=1$) and $W = 2$ GeV are also shown on Fig. 6. $W = 2$ GeV is traditionally taken as the demarkation between the "resonance region" and the "inelastic region".

From Eq. 18, we see that for $y \simeq 0.95$ and E_o corresponding to the maximum energy in each experiment, we will obtain the maximum values of x for a given Q^2. These curves are shown in Fig. 6. At SLAC most of the kinematic region attainable with $E_o < 20$ GeV has been covered (including the resonance region and elastic scattering). The muon experiments and

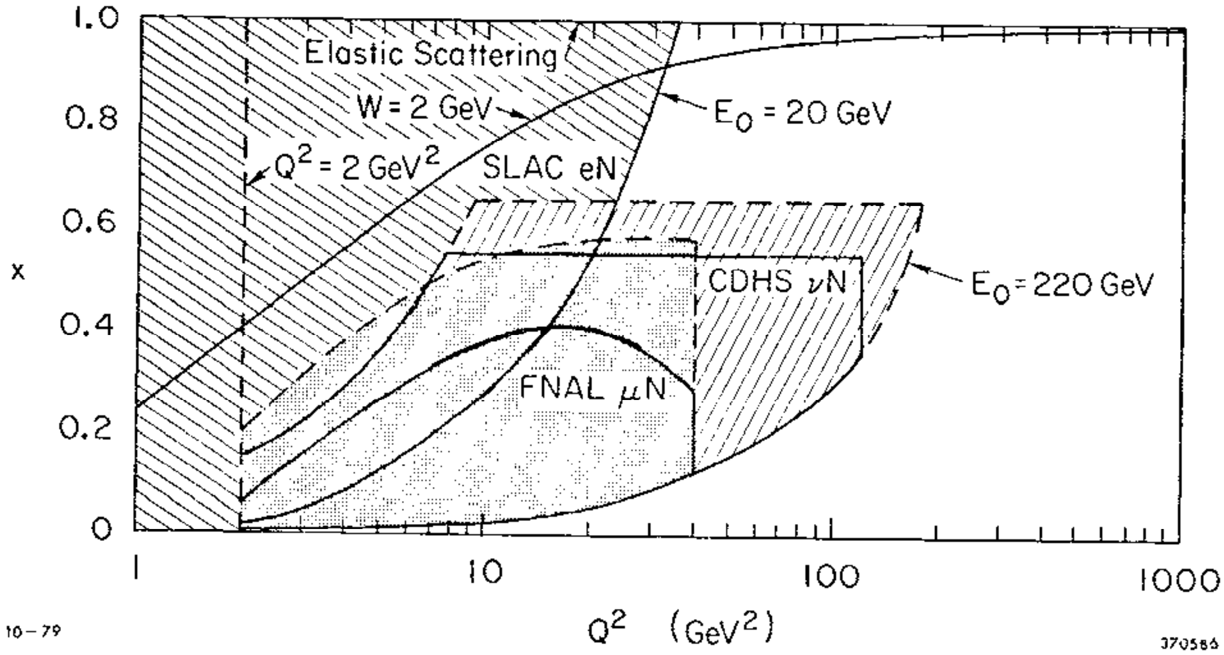

Figure 6. Kinematic range of the experiments.

the neutrino experiments have used beam energies up to about 220 GeV. The kinematic regions covered by these experiments is also shown in Fig. 6. Note that some of the high x region is not accessible to these experiments because the effective luminosity is lower than in the SLAC experiments. The muon and electron experiments undergo an additional decrease in cross section with increasing beam energy (like E_o^{-2}) compared with the neutrino experiments where the cross sections are rising with E_o.

2.2. Lepton - Nucleon Scattering Cross Sections

The cross section for high energy electron (muon) scattering from nucleons may be written (in the one photon exchange approximation) as

$$\frac{d\sigma}{dQ^2dx} = \frac{4\pi\alpha^2}{Q^4}\left[\left(1 - y - \frac{Mxy}{2E_o}\right)\frac{F_2^{eN}(x,Q^2)}{x} + \frac{y^2}{2}\, 2F_1^{eN}(x,Q^2)\right] \qquad (19.1)$$

or, in terms of y,

$$\frac{d\sigma}{dxdy} = \frac{4\pi\alpha^2}{Q^4}(2ME_o)\left[\left(1 - y - \frac{Mxy}{2E_o}\right)F_2^{eN}(x,Q^2) + \frac{y^2}{2}\, 2\,x\,F_1^{eN}(x,Q^2)\right]. \qquad (19.2)$$

Here α is the coupling strength for electromagnetism ($\alpha = 1/137$) and $F_{1,2}^{eN}(x,Q^2)$ are two independent structure functions which describe the interaction of the virtual photon with the nucleon. In an older notation $\nu W_2 (= F_2^{eN})$ and $MW_1 (= F_1^{eN})$ were used to designate those functions but I will use the now popular F_1 and F_2 exclusively.

Gottfried Sum Rule and Callan-Gross Relation

To understand the physical significance of F_1 and F_2 consider the limit of small y. In this case the incident electron (muon) loses a small fraction of its energy and Eq. 19.1 then becomes

$$\frac{d\sigma}{dQ^2dx} \cong \frac{4\pi\alpha^2}{Q^4} \frac{F_2(x,Q^2)}{x} \tag{20.1}$$

An example of a process described by this approximation would be forward elastic scattering from very heavy target particles. Integrating over x in Eq. 20.1 gives

$$\frac{d\sigma}{dQ^2} = \frac{4\pi\alpha^2}{Q^4} \int_0^1 \frac{F_2(x,Q^2)}{x} dx \tag{20.2}$$

This is the old Rutherford formula if we identify

$$\int_0^1 \frac{F_2(x,Q^2)}{x} dx = \sum Z_i^2 \tag{21}$$

where Z_i is the charge of the i^{th} target particle. This relation, equating the integral of F_2 weighted by $1/x$ to the sum of the squared charges, is the Gottfried sum rule $^{(9)}$. In the simple quark model for the proton

$$\sum Z_i^2 = 2\left(\frac{2}{3}\right)^2 + 1\left(\frac{1}{3}\right)^2 = 1 \quad . \tag{22}$$

For the SLAC data, this sum rule has been evaluated:

$$\int_{.02}^{.82} \frac{F_2^{ep}(x,Q^2)}{x} dx = 1.05 \pm 0.09 \tag{23}$$

over the Q^2 range 1 $GeV^2 < Q^2 < 20\ GeV^2$. (10) Since F_2^{ep} is very small at large x, extrapolation to x = 1 would introduce a negligible contribution to the integral. But extrapolating towards x = 0 is problematical. In this region the simple quark model with only 3 valence quarks is a poor model for the data. Quark-anti-quark pairs produce the dominant contribution to F_2 at low x and complicate the simple picture. The apparently good agreement with the simple quark model may just be a coincidence.

Next consider the case of a "point-like", spin ½ target particle of charge Z. The x dependence of both F_1 and F_2 is then proportional to $\delta(x - 1)$. We can write the cross section as

$$\frac{d\sigma}{dQ^2} = \frac{4\pi\alpha^2}{Q^4}\left[\left(1 - y - \frac{My}{2E_o}\right) + \frac{y^2}{2}\right]Z^2 . \qquad (24)$$

Comparing this with Eq. 19.1 suggests the following relationship:

$$2\ x\ F_1(x,Q^2) = F_2(x,Q^2) . \qquad (25)$$

This is called the Callan-Gross relation (11) and is observed to agree fairly well with the measured data. Thus, assuming the Callan-Gross relation holds for electron-nucleon scattering, Eq. 19.2 becomes (neglecting the M/E_o term):

$$\frac{d\sigma}{dxdy} \simeq \frac{8\pi\alpha^2}{Q^4}\,(ME_0)\left[\frac{F_2(x,Q^2)}{2} + \frac{F_2(x,Q^2)}{2}\,(1-y)^2\right] . \qquad (26)$$

Neutrino - Nucleon Scattering Cross Section

For scattering of neutrinos from nucleons, photon exchange is replaced by W^+ or W^- vector boson exchange and the cross section can be written in a form closely resembling that of Eq. 19. The electromagnetic coupling α and the virtual photon propagator $1/Q^2$ are replaced with the weak coupling constant, G^2. The chiral nature of the weak current results in the appearance of a third structure function $F_3(x,Q^2)$ which is absent from the cross sections given in Eq. 19. The neutrino cross section is:

$$\frac{d\sigma^{\nu,\bar{\nu}}}{dxdy}=\frac{G^2}{\pi}(ME_o)\left[(1-y-\frac{Mxy}{2E_o})F_2^{\nu,\bar{\nu}}(x,Q^2)+\frac{y^2}{2}2xF_1^{\nu,\bar{\nu}}(x,Q^2)\pm y(1-\frac{y}{2})xF_3^{\nu,\bar{\nu}}(x,Q^2)\right] \tag{27}$$

The sign of F_3 in the above expression is positive for neutrino scattering and negative for antineutrinos.

Since the lepton changes its charge in (charged-current) neutrino-scattering, so must the target. As such, the constituents must change their charge state. Charged current neutrino scattering, at the outset, requires a more explicit description of the constituents than does electron (muon) scattering. In the quark model, quarks are grouped into left-handed doublets: $\begin{pmatrix}u\\d\end{pmatrix}$, $\begin{pmatrix}c\\s\end{pmatrix}$, and $\begin{pmatrix}t\\b\end{pmatrix}$. The upper member of each doublet has charge +2/3 while the lower member has charge -1/3. There is a small mixing between these doublets parameterized by the Cabbibo angle, but this is a small effect and in order to keep this discussion simple, I will neglect it (i.e. I take $\sin\theta_{Cab} = 0$).

Exchange of a W^+ (neutrino scattering) acts as a raising operator ($\nu + d \rightarrow \mu^- + u$) and exchange of a W^- (anti-neutrino scattering) acts as lowering operator ($\bar{\nu} + u \rightarrow \mu^+ + d$) on the isospin of these quark doublets. As a result the scattering of neutrinos off d quarks is equal to the scattering of anti-neutrinos off u quarks ($F_2^{\nu d} = F_2^{\bar{\nu} u}$). Since protons and neutrons form an isospin doublet we expect $F_2^{\bar{\nu} p} = F_2^{\nu n}$ and, for scattering from an isoscalar target (equal numbers of neutrons protons), $F_2^{\nu N} = F_2^{\bar{\nu} N}$. The difference between neutrino and anti-neutrino scattering thus arises from the change in the sign of the F_3 structure function in the cross section (Eq. 27).

Callan-Gross Relation in Neutrino Scattering

Again, consider the case of a simple Dirac target particle, this time with a beam of neutrinos incident (e.g. $\nu + e^- \rightarrow \nu + e^-$ scattering). Fig. 7 shows two cases: one for an electron target and one for a positron target. In the electron case both the neutrino and the electron have negative helicity resulting in $J_z = 0$ in the center of mass system (CMS). This leads to a flat angular distribution in the CMS which, when transformed into the lab system (electron initially at rest), becomes a flat y distribution. For the positron target, $J_z = -1$ in the CMS giving a $(1 + \cos\theta_{cm})^2$ angular distribution which becomes a $(1 - y)^2$ distribution in the lab (See Eq. 17). In general neutrino scattering off spin ½ Dirac particles results in a flat y distribution and neutrino scattering of spin ½ antiparticles gives a $(1 - y)^2$ distribution.

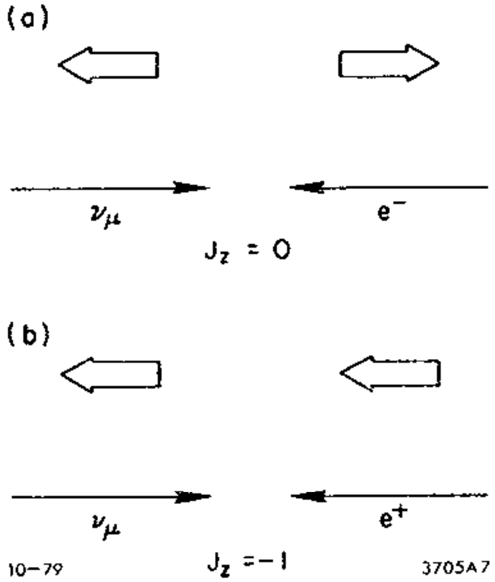

Figure 7. Helicity considerations in scattering of Dirac particles.

Now apply this to quark and anti-quark scattering inside a nucleon. Suppose the quarks have an x distribution, q(x), (similarly antiquarks have a distribution $\bar{q}(x)$); then the neutrino and anti-neutrino cross sections from the nucleon would be

$$\frac{d\sigma^{\nu,\bar{\nu}}}{dxdy} = \frac{2G^2}{\pi}(x\ ME_o)\begin{Bmatrix}(q(x) + (1-y)^2\ \bar{q}(x))\ \text{for}\ \nu\text{'s} \\ \\ (\bar{q}(x) + (1-y)^2\ q(x))\ \text{for}\ \bar{\nu}\text{'s}\end{Bmatrix}\ . \tag{28}$$

If we assume the Callan-Gross relation (Eq. 25), and neglect the M/E_o term, we can write the cross section (Eq. 27) for an isospin symmetry target as

$$\frac{d\sigma^{\nu,\bar{\nu}}}{dxdy} = \frac{G^2}{\pi}(ME_o)\left[\frac{F_2 \pm xF_3}{2} + (1-y)^2\frac{F_2 \mp xF_3}{2}\right] \tag{29}$$

where the upper (lower) signs refer to $\nu(\bar{\nu})$ scattering. Comparing Eq. 28 to Eq. 29, we identify:

$$2\ x\ q(x,Q^2) = \frac{F_2(x,Q^2) + xF_3(x,Q^2)}{2} \tag{30.1}$$

$$2\ x\ \bar{q}(x,Q^2) = \frac{F_2(x,Q^2) - xF_3(x,Q^2)}{2} \tag{30.2}$$

or

$$F_2(x,Q^2) = 2\ x\left[q(x,Q^2) + \bar{q}(x,Q^2)\right] \tag{31.1}$$

$$xF_3(x,Q^2) = 2\ x\left[q(x,Q^2) - \bar{q}(x,Q^2)\right]. \tag{31.2}$$

It is interesting to compare Eq. 29, the cross section for neutrino scattering off nucleons, with Eq. 26, that for electron (muon) scattering off nucleons. In lowest order photons don't distinguish between quarks and anti-quarks; photons couple to the electric charge. Electron (muon) scattering probes the charge structure of the nucleon, and neutrino scattering probes the particle-antiparticle structure of the nucleon.

If nucleons are mostly quarks, then νN scattering should have little y dependence and $\bar{\nu} N$ scattering should behave as $(1 - y)^2$. In Fig. 8 the y distributions of the data from the CDHS collaboration for ν and $\bar{\nu}$ scattering from iron is shown. The open points (ν scattering) have little y dependence as expected while the solid points ($\bar{\nu}$ scattering) show the expected $(1 - y)^2$ behavior. The small $(1 - y)^2$ contribution seen in the ν scattering data and the small constant contribution to the $\bar{\nu}$ scattering data are interpreted as the antiquark contributions coming from the $q - \bar{q}$ pairs inside the nucleon (the so-called "sea" of quarks).

2.3. Consistency and Comparison of the Data in the Simple Quark Model

Before considering detailed tests of QCD, we should check that the data from the different experiments are internally consistent. We want to assure ourselves that the electron and muon experiments are measuring the same structure functions and that these in turn (when adjusted for the various quark charges) are the same as the structure functions measured in neutrino scattering. Furthermore, we wish to show how well the simple quark picture of the nucleon works.

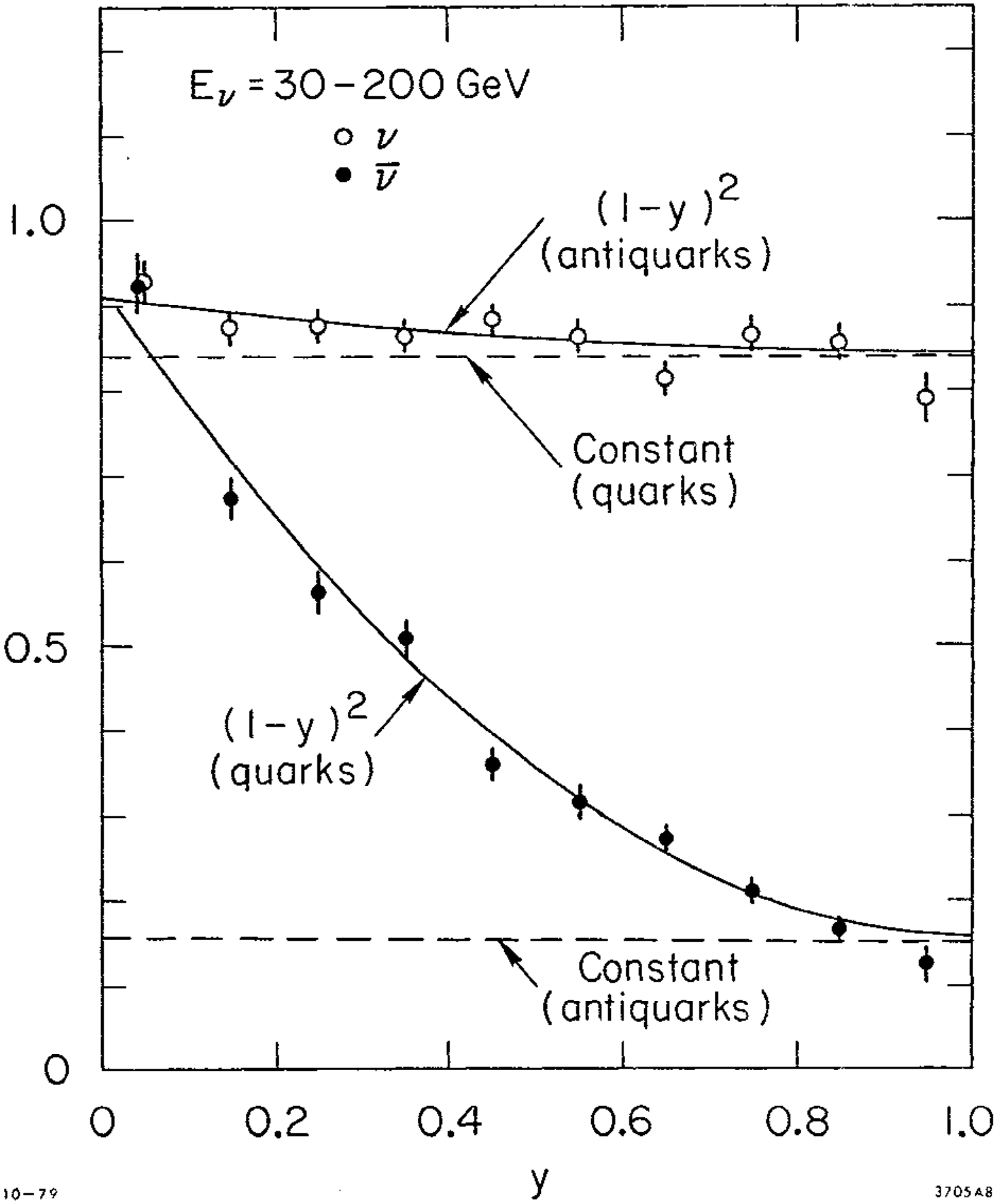

Figure 8. Neutrino - iron scattering cross section versus y.

Electrons Compared with Muons

In Fig. 9, the x distribution of the F_2 structure function measured in muon scattering experiments from hydrogen at Fermilab is compared to similar data taken at SLAC with incident electrons. The solid points (SLAC data) cover lab scattering angles of 10 - 60 degrees (the range in y is about 0.25 - 0.95). The open points (CHIO data) are typically for lab angles of 1 - 2 degrees. The agreement between the two data sets is good for this Q^2 bin. Comparing the two data sets in the entire overlap region in x and Q^2 reveals the muon scattering experiments to be systematically lower than the SLAC experiments by about 15%. This is at the edge of the claimed systematic errors and the χ^2 in the overlap region is 46/34 degrees of freedom indicating that the hypothesis of consistency is only about 5% probable. Clearly more data (particularly muon data) are needed to clarify this situation, but in the rest of this discussion we assume that the e and μ data are measuring the same structure functions.

Neutrinos Compared with Electrons and Muons

I will denote the up quark distribution in the proton as u(x), down quarks in the proton as d(x), s(x) for the strange quarks, etc.

The F_2^{ep} structure function can then be written by inserting the appropriate squared quark charges:

$$F_2^{ep} = x\left[\frac{4}{9}(u+\bar{u}) + \frac{1}{9}(d+\bar{d}) + \frac{1}{9}(s+\bar{s}) + \ldots\right]. \quad (32.1)$$

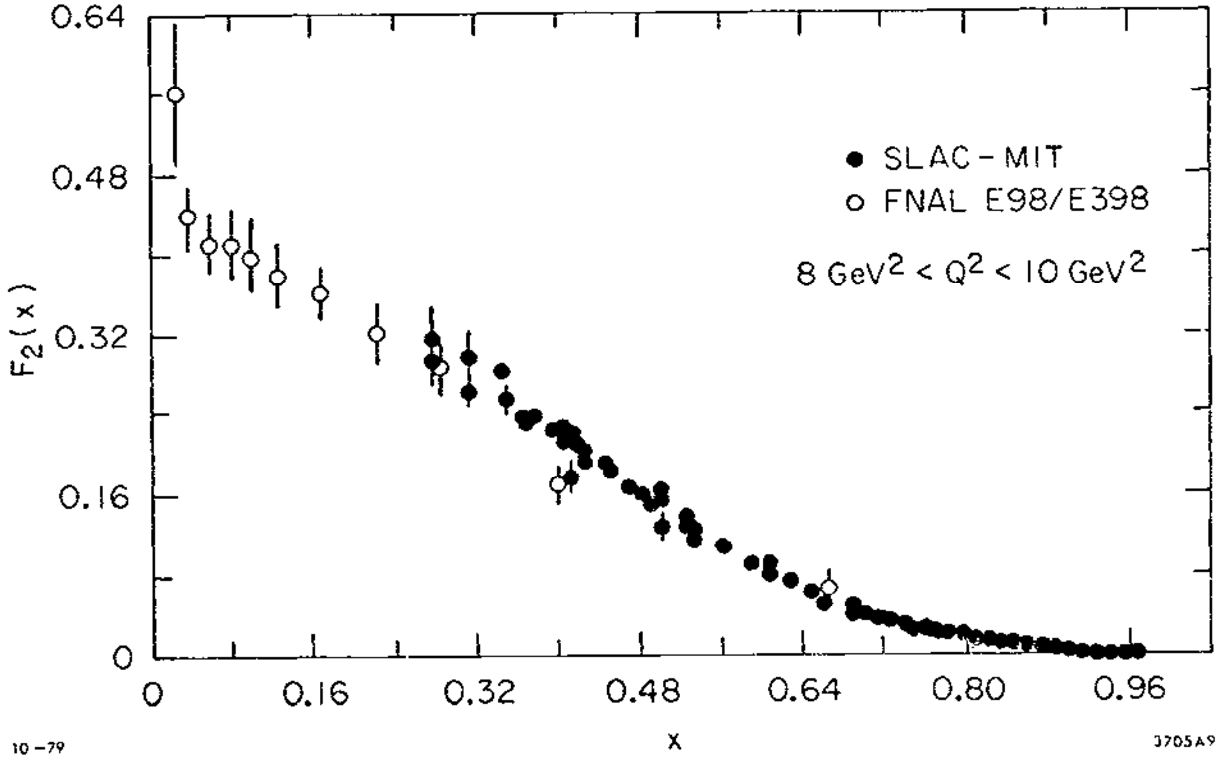

Figure 9. Proton structure function F_2 versus x from electron - proton (solid points) and muon - proton (open points) scattering.

To obtain F_2^{en}, we have a similar expression where u(x) is replaced with d(x) and visa versa. This is an obvious consequence of the isospin symmetry between protons and neutrons: the up quark in the proton has the same distribution as the down quark in the neutron.

$$F_2^{en} = x\left[\frac{4}{9}(d+\bar{d}) + \frac{1}{9}(u+\bar{u}) + \frac{1}{9}(s+\bar{s}) + \ldots\right] . \qquad (32.2)$$

For isoscalar targets, F_2^{eN} is the average of F_2^{ep} and F_2^{en}. Neglecting the contribution of s and $\bar{s}$ and so on, we obtain:

$$F_2^{eN} \cong \frac{5}{18}\, x \left[(u+\bar{u}) + (d+\bar{d})\right] \qquad (33.1)$$

For neutrino scattering all quarks enter with the same coupling strength independent of electric charge so that:

$$F_2^{\nu N} \cong x\left[(u+\bar{u}) + (d+\bar{d})\right] \qquad (33.2)$$

(again only the u and d contributions have been kept). Therefore, in the simple quark model, the ratio of neutrino scattering to electron (muon) scattering should be 18/5 if electrons (muons) and neutrinos are probing the same quark distributions.

To increase the statistical precision of this comparison the practice has been to compare the values of F_2 integrated over x. The integral of F_2 is called the momentum sum rule and using the SLAC-MIT data is found to be $\int F_2^{eN}\, dx = 0.15 \pm 0.01$ (10). The results from the Gargamelle experiments at the PS in CERN is $\int F_2^{\nu N}\, dx = 0.49 \pm 0.05$ (12). The ratio is 3.3 ± 0.4 and is consistent with the value of 3.6 expected in the simple quark model.

These integrals of F_2 over x for both electron and neutrino scattering are only ½ of what would be expected if quarks accounted for the entire four-momentum of the nucleon. Presumably the missing half resides in the particles that bind the quarks together. These unseen particles, gluons, are believed to participate in neither electron nor neutrino scattering.

A comparison of the shapes of $F_2(x)$ for neutrino (CDHS) and electron (SLAC) scattering is shown in Fig. 10. The normalization has been chosen so that the integrals of the distributions are the same. The shapes of the distributions are in good agreement and the accepted conclusion is that all leptons are probing the same quark distributions inside nucleons.

Gross - Llewellyn-Smith Sum Rule and the Antiquark Component

There are two more neutrino results which support the simple quark model. First, the number of valence quarks (as distinct from quarks coming from the sea) can be measured in neutrino scattering. The difference between neutrino and anti-neutrino cross sections measured off an isoscalar target is proportional to

$$xF_3^{\nu N} = x\left[\, q(x) - \bar{q}(x) \,\right] . \qquad (34)$$

The factor of 2 from Eq. 31.2 is cancelled by taking the average of protons and neutrons. The integral of $q(x) - \bar{q}(x)$ should, therefore, equal the number of valence quarks inside the nucleon. This is expected to be exactly 3 in simple quark model. This notion is called Gross-Llewellyn-Smith sum rule,

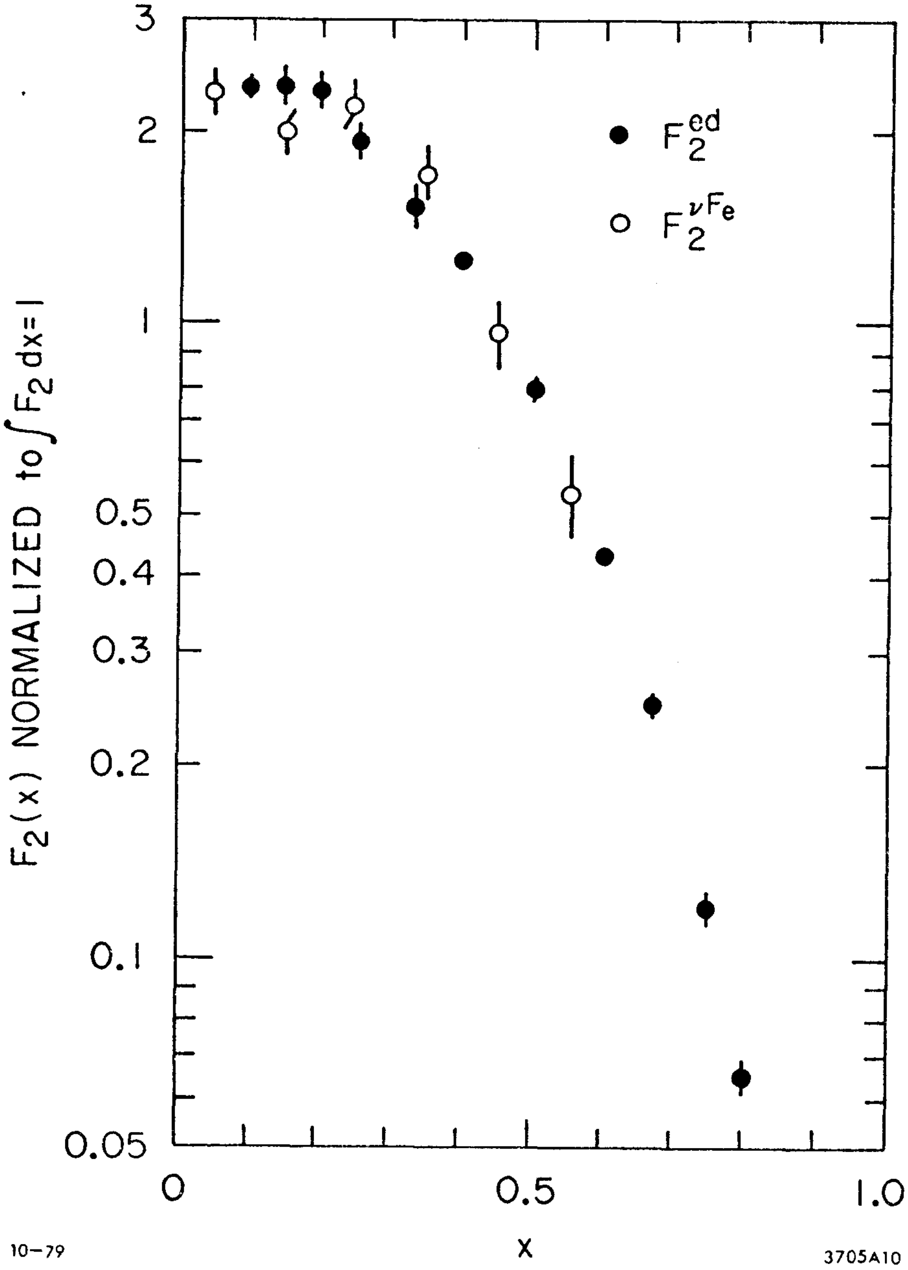

Figure 10. Nucleon structure function F_2 versus x from electron - deuterium (solid points) and neutrino - iron (open points) scattering.

$$\int_0^1 \frac{xF_3}{x}\, dx = \text{number of valence quarks.} \qquad (35)$$

In Fig. 11, the CDHS evaluation of the GLS sum rule is shown. The solid line indicates their extrapolation to $x = 0$ at which point the estimated value is 3.2 ± 0.5 (the error includes the uncertainty coming from the extrapolation procedure). This value is in good agreement with the expected value of 3.

The second result is an estimate of the antiquark component in the nucleon measured in neutrino scattering. As indicated in Fig. 8 the small $(1 - y)^2$ term in neutrino scattering and the small constant term in anti-neutrino scattering can be interpreted as coming from antiquarks. By fitting these distributions (after applying QED radiative corrections to the outgoing muon), the authors quote $\int \bar{q}\, dx / \int (\bar{q} + q)\, dx = 0.15 \pm 0.03$ (5) for the CDHS neutrino data, a value not far from zero, the expected value in the simple quark model.

These experimenters have also used another approach to evaluate the antiquark fraction. They observe that

$$x\bar{q}(x,Q^2) \cong \frac{\pi}{G^2} \frac{1}{ME_o} \left[\frac{d\sigma^{\bar{\nu}}}{dxdy} - (1 - y)^2 \frac{d\sigma^{\nu}}{dxdy} \right] \qquad (36)$$

in the region of high y. They use the neutrino data to subtract out the quark contribution in their anti-neutrino data. The resulting anti-quark fraction is $\int \bar{q}\, dx / \int (\bar{q} + q)\, dx = 0.16 \pm 0.01$ (5). This result agrees with that obtained by the fitting method: the simple quark model of the nucleon seems to be quite good. These results indicate that the nucleon

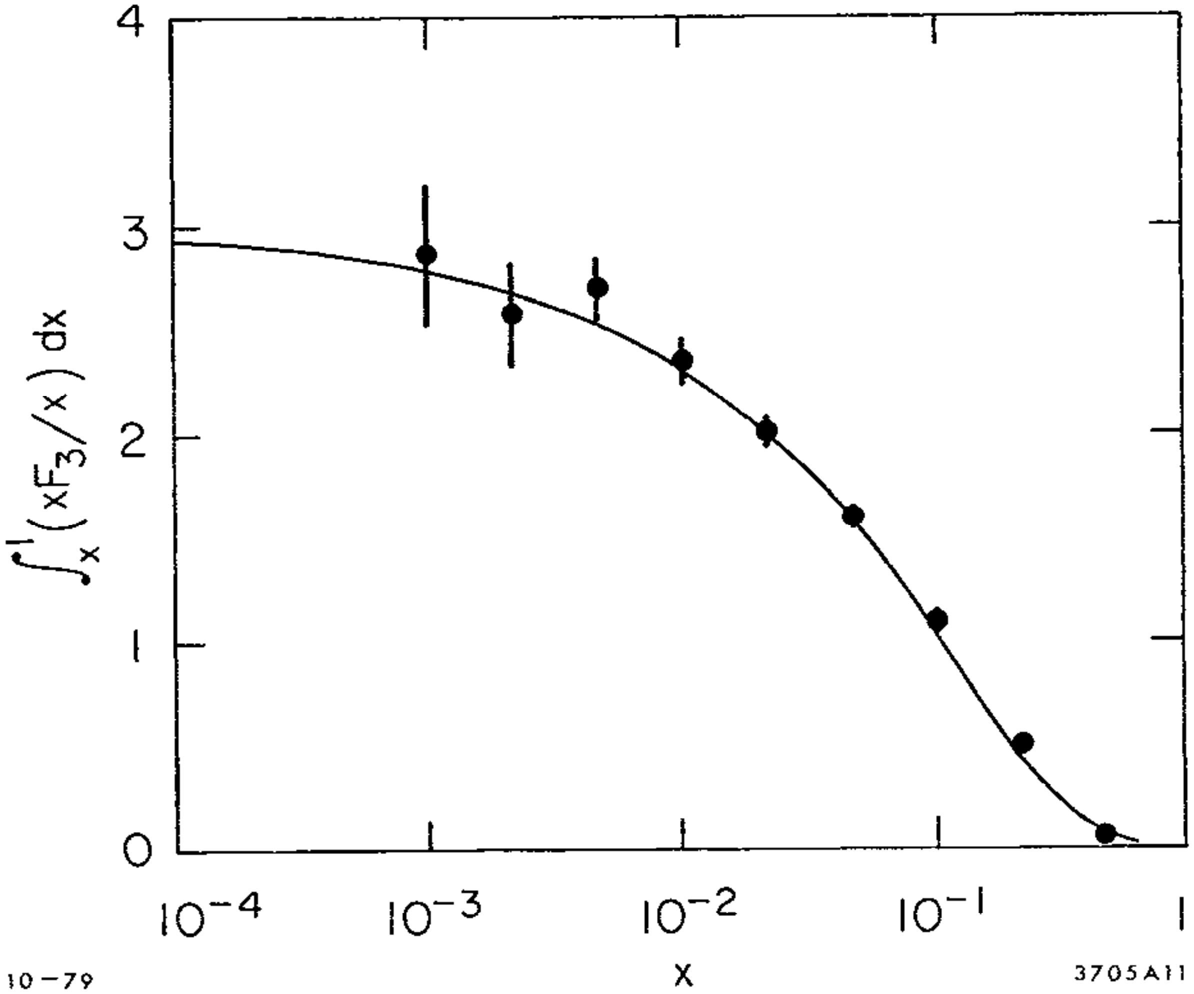

Figure 11. Gross - Llewellyn-Smith sum rule in neutrino scattering presented as a function of the lower integral bound.

is made up of 3 "valence" quarks (~70%) and a smaller "sea" of $q - \bar{q}$ pairs (~30%).

To summarize, we see that most of the expectations of the simple quark model are consistent with the data but there are two indications of a more complicated structure. The first indication is the evidence from the neutrino experiments that there are antiquarks in the nucleon at low values of x, presumably a sea of $q - \bar{q}$ pairs. The second indication is the small value of F_2 integrated over x (momentum sum rule). The integral is about half of the value expected if the nucleon contained only quarks and antiquarks. These observations suggest that the quarks may be bound by objects which dissociate into $q - \bar{q}$ pairs easily, and carry about half of the four-momentum of the nucleon. In Quantum Chromodynamics, these particles are the gluons, and we now turn to a discussion of this theory and its relation to the data.

3. QUANTUM CHROMODYNAMICS IN LEPTON - NUCLEON SCATTERING

In this section, I discuss some QCD phenomena in lepton-nucleon interactions. The presence of the running coupling constant is possibly the most important single aspect of QCD in these phenomena. Three "tests" of QCD are then reviewed: R, the ratio of longitudinal to transverse photon cross sections (Sec. 4); G_M, the nucleon elastic form factor (Sec. 5); and the Q^2 dependence of nucleon structure functions (Sec. 6). The latter topic receives a rather large discussion - in proportion to the number of theoretical discussions lately.

3.1. The General Scheme

QCD is a theory of quark interactions$^{(13)}$ much analogous to QED: the interaction is carried by "gluons" (analogous to photons) which couple to the "color" (analogous to charge) of the quarks. The simple quark model described in Sec. 2 predicts structure functions which, at fixed x, are independent of Q^2. But QCD predicts subtle scale breaking effects: the coupling constant, α_s, as well as the nucleon structure functions should vary in Q^2 like $\ln(Q^2/\Lambda^2)$, where Λ is a scale parameter of about 0.5 GeV. $\alpha_s(Q^2)$ is called the "running" coupling constant.

The main difference between QED and QCD is that gluons carry color while photons don't carry charge. This means that when a quark emits a gluon it changes its color. It also means that gluons couple to each other. In the language of gauge field theories, QCD is non-abelian.

3.2. The Running Coupling Constant

Fig. 12 shows the basic QCD couplings. Fig. 12a represents gluon bremsstrahlung from a quark. Fig. 12b shows quark pair production from a gluon. The coupling strength at the quark-gluon vertex is α_s. In addition to this diagram, a three gluon coupling is also possible as shown in Fig. 12c since the gluons carry the "color charge".

In QED the effective coupling strength varies with the Q^2 of the incident photon. This is due to vertex corrections of the electro-magnetic current. The first order correction to the QED coupling, α, is

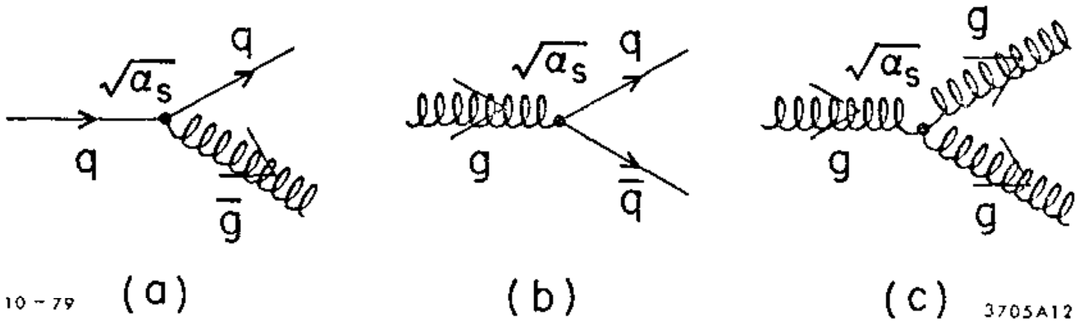

Figure 12. Basic QCD couplings: a) Bremsstrahlung of gluon from quark, b) pair production of quarks from gluon, and c) three-gluon coupling. The latter has no analog in QED.

$$\alpha(Q^2) = \alpha(\mu^2)\left[1 + \frac{\alpha(\mu^2)}{3\pi}\ln\left(\frac{Q^2}{\mu^2}\right)\right] \tag{37}$$

where μ is an arbitrary normalization point at which the coupling strength, α, has been measured. If all terms containing powers of ln (Q^2/μ^2) are summed, the "leading log approximation" results:

$$\alpha(Q^2) = \frac{\alpha(\mu^2)}{\left[1 - \frac{\alpha(\mu^2)}{3\pi}\ln\left(\frac{Q^2}{\mu^2}\right)\right]} \quad . \tag{38}$$

This expression predicts that the effective QED coupling increases in strength with increasing Q^2. The physical content of Eq. 38 is that as Q^2 increases the photons see more of the bare charge and vacuum polarization plays an ever decreasing role in screening this charge.

One may perform the same analysis for QCD. The result is

$$\alpha_s(Q^2) = \frac{\alpha_s(\mu^2)}{\left[1 + B\alpha_s(\mu^2)\ \ln\left(\frac{Q^2}{\mu^2}\right)\right]} \tag{39}$$

where

$$B = \frac{33 - 2N_f}{12\pi} \tag{40}$$

and N_f is the number of quark flavors, such as up, down, strange, etc. The usual choice of $N_f = 4$ results in $B = 25/12\pi$. Eq. 39 can be simplified by the substitution

$$\Lambda^2 = \mu^2 \exp\left(-\frac{1}{B\alpha_s(\mu^2)}\right) \quad . \tag{41}$$

Thus we obtain the convenient form:

$$\alpha_s(Q^2) = \frac{1}{B \ln\left(\frac{Q^2}{\Lambda^2}\right)} \quad . \tag{42}$$

If the number of quark flavors is less than 17, B will be positive and α_s will decrease with increasing Q^2. Contrast this Q^2 variation with that of QED in Eq. 38.

The usual practice is to calculate the lowest order process (in $\alpha_s(Q^2)$) and hope higher orders don't change the results significantly. As such it is interesting to see what the current best estimates for the size of $\alpha_s(Q^2)$ is for various values of Q^2.

TABLE 2

Running coupling constant α_s vs Q^2 (as in Eq. 42) for $\Lambda = 0.5$ GeV and $N_f = 4$

Q^2 (GeV^2)	α_s
1	1.09
5	0.50
30	0.31
60	0.28
35000	0.13

Since $\alpha_s(Q^2)$ is large in the low Q^2 range, lowest order calculations may be quite inaccurate. Also most of the change in $\alpha_s(Q^2)$ occurs for $Q^2 < 30$ GeV^2. Scaling violation should be most pronounced in this lower Q^2 region and become fainter at higher values of Q^2.

3.3. Pattern of Scale - Breaking

QCD predicts a systematic deviation from scaling as Q^2 increases. As the virtual photon's Q^2 increases, the distances at which the target is being probed decreases. What appears at low Q^2 to be a quark may, at a higher Q^2, be resolved into a quark and a gluon. The emission of this gluon reduces the 4-momentum of the quark and hence reduces the fraction, x, of nucleon's 4-momentum carried by the quark. QCD predicts that the x distribution of quarks will be systematically shifted to lower values of x as Q^2 increases. At high x the structure functions should decrease with increasing Q^2 while at low x they should increase with increasing Q^2.

This pattern of scaling violation has been observed in the electron and muon deep inelastic scattering experiments and the neutrino scattering experiments. In Fig. 13 the F_2 distributions from the CHIO data (μp data) combined with the SLAC data (ep) are shown in x bins versus Q^2. At high x the data falls as Q^2 increases. At low x, F_2 increases as Q^2 increases. The same pattern of scaling violation has been observed by the CDHS collaboration in neutrino scattering. Fig. 14 is the analogous plot to Fig. 13 for the neutrino F_2 distributions. This universally observed behavior of the structure functions with increasing Q^2 is counted as a major success of the QCD theory.

4. RATIO OF LONGITUDINAL TO TRANSVERSE PHOTOABSORPTION CROSS SECTIONS

In this section, I discuss our theoretical hierarchy in relation to R,

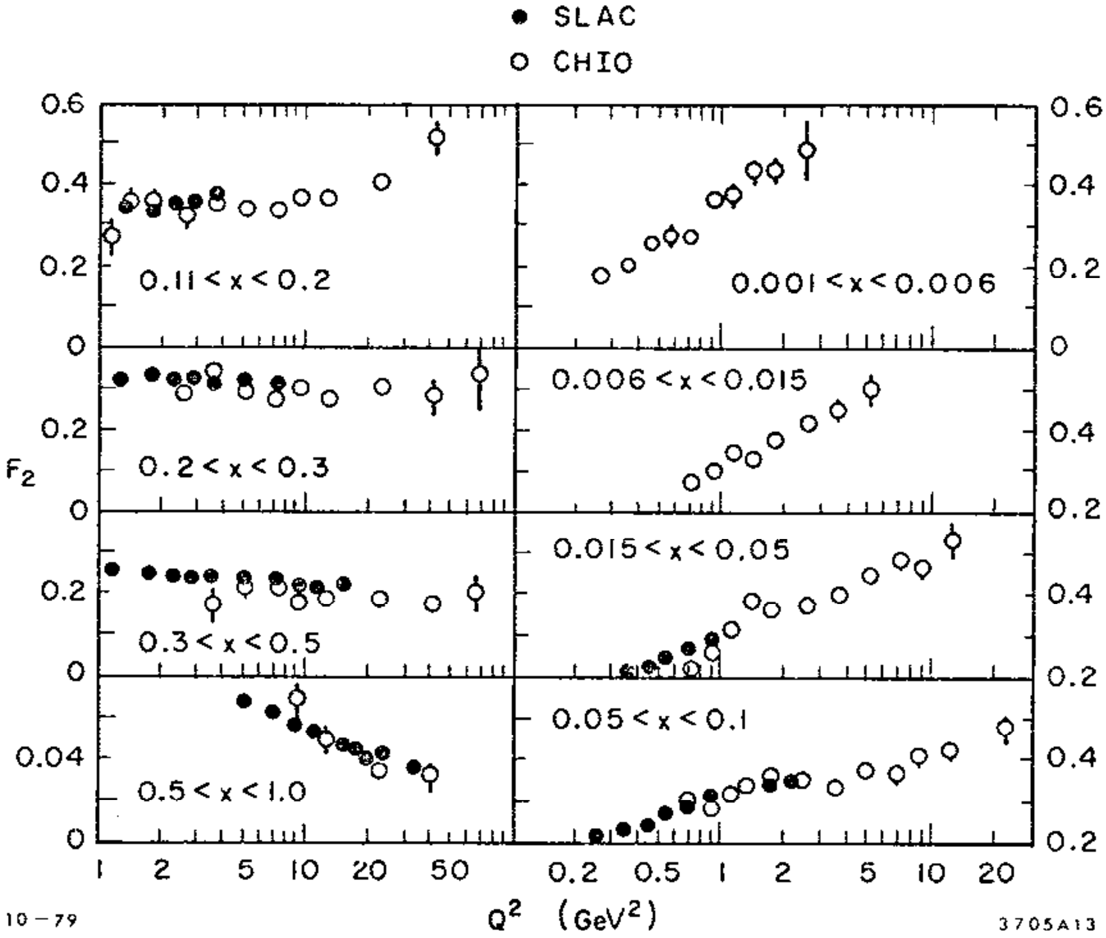

Figure 13. Proton structure function F_2 from ep (solid points) and μp (open points) scattering showing scale breaking.

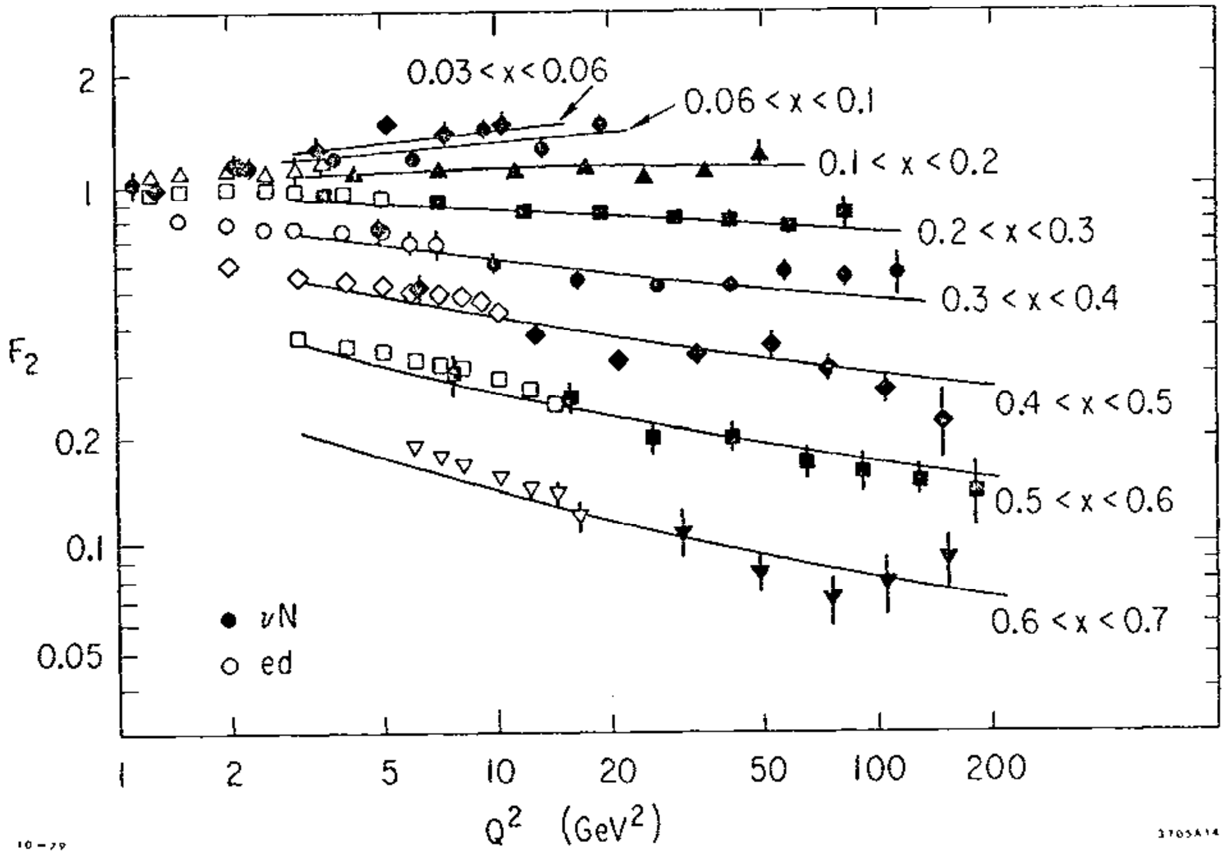

Figure 14. Nucleon structure function F_2 from νN (solid points) and ed (open points) scattering.

the ratio of longitudinal to transverse photoabsorption cross sections. First I discuss the electron (muon) data in terms of the Callan-Gross relation and QCD. Then the neutrino data is treated for which an analogous R_ν can be defined.

4.1. Definition of R

Deep inelastic scattering experiments directly measure cross sections which are in turn combinations of structure functions multiplied by known kinematic factors. As shown earlier the structure functions can be related to each other in the case of structureless spin ½ target particles by the Callan-Gross relation in Eq. 25. The measured cross sections can also be expressed in terms of total (virtual) photo-absorption cross sections: σ_T for transversely polarized photons and σ_L for longitudinally polarized photons (14). These photo-absorption cross sections can be expressed in terms of the structure functions as

$$\sigma_T = \frac{4\pi^2\alpha}{MK} F_1(x,Q^2) \tag{43.1}$$

and

$$\sigma_L = \frac{4\pi^2\alpha}{MK} \left[\frac{M}{\nu} \left(1 + \frac{1}{r_c}\right) F_2(x,Q^2) - F_1(x,Q^2)\right] \tag{43.2}$$

where

$$K = \frac{W^2 - M^2}{2M} \tag{44.1}$$

is the energy of a real photon needed to produce mass W in the final state and

$$r_c \equiv \frac{Q^2}{\nu^2} = \frac{4M^2x^2}{Q^2} \quad . \tag{44.2}$$

These expressions can be inverted to give

$$F_1(x,Q^2) = \frac{MK}{4\pi^2\alpha}\,\sigma_T \tag{45.1}$$

$$F_2(x,Q^2) = \frac{\nu K}{4\pi^2\alpha}\left(\frac{r_c}{1 + r_c}\right)(\sigma_T + \sigma_L) \quad . \tag{45.2}$$

The cross section expression becomes (using σ_L and σ_T):

$$\frac{d\sigma}{dQ^2dx} = \Gamma\ (\sigma_T + \varepsilon\sigma_L) \tag{46}$$

where

$$\Gamma = \frac{\alpha}{\pi}\,\frac{MKy^2}{Q^4}\,\frac{1}{1 - \varepsilon} \tag{47}$$

and

$$\varepsilon = \frac{1 - y - \dfrac{Q^2}{4E_o^2}}{1 - y + \dfrac{y^2}{2} + \dfrac{Q^2}{4E_o^2}} \quad . \tag{48}$$

An alternative expression for ε is

$$\varepsilon = \frac{1}{1 + 2\tan^2\theta/2\left(1 + \dfrac{\nu^2}{Q^2}\right)} \tag{49}$$

In the limit $Q^2 << 4E_o{}^2$ (which is always true when $E_o >> M$) we have the approximation:

$$\varepsilon \cong \frac{2(1 - y)}{2\ (1 - y) + y^2} \quad . \tag{50}$$

The ε parameter is the ratio of the longitudinally polarized virtual photon flux to the transversely polarized virtual photon flux. ε is not the photon polarization: ε = 0 means pure transverse polarization and ε = 1 means a 50/50 mixture of longitudinal and transverse photons.

The ratio of the longitudinal to transverse total photo-absorption cross sections may be expressed as

$$R \equiv \frac{\sigma_L}{\sigma_T} = \frac{F_2(x,Q^2)}{2xF_1(x,Q^2)}\ (1 + r_c) - 1 \quad . \tag{51}$$

R in Elastic Scattering and Finite Mass Effects

If the Callan-Gross relation (Eq. 25) were precisely true, then we would have

$$R = r_c = \frac{Q^2}{\nu^2} = \frac{4M^2x^2}{Q^2} \quad . \tag{52}$$

R for elastic scattering is perhaps easiest to understand. The F_i's for elastic scattering off protons are

$$F_2(x,Q^2) = \frac{2MG_E{}^2(Q^2) + yE_oG_M{}^2(Q^2)}{2M + yE_o}\ \delta(x - 1) \tag{53.1}$$

$$F_1(x,Q^2) = \frac{G_M{}^2(Q^2)}{2}\ \delta(x - 1) \tag{53.2}$$

where G_E and G_M are the electric and magnetic form factors respectively. From these formulas one obtains

$$R_{el}(Q^2) = \frac{2M}{yE_o} \frac{{G_E}^2(Q^2)}{{G_M}^2(Q^2)} = r_c \frac{{G_E}^2(Q^2)}{{G_M}^2(Q^2)} \quad . \tag{54}$$

Using the so-called form factor scaling relation

$$G_M(Q^2) = \mu_p \; G_E(Q^2) \tag{55}$$

where μ_p (= 2.79) is the magnetic moment of the proton, we obtain the simple expression for R_{el}:

$$R_{el} = \frac{r_c}{\mu_p^2} \tag{56}$$

Thus for elastic scattering R is the ratio of the electric to magnetic form factors squared. For spin ½ Dirac particles at rest (no anomalous magnetic moment)

$$R = \frac{4M^2}{Q^2} = r_c \Big|_{x=1} \quad . \tag{57}$$

This serves to remind us that the finite mass of the target particle produces a non-zero value for R for finite values of Q^2. The reason for discussing R_{el} in detail is that the model for understanding deep inelastic scattering has at its core quasi-elastic quark scattering. Finite mass quarks will lead to non-zero R values at finite values of Q^2. If the Callan-Gross relation were true for deep inelastic scattering, this would imply (in the simple quark model) that quarks were spin ½ particles, approximately at rest with an effective squared mass $(\xi p_\mu)^2 \cong x^2M^2$.

Effect of Transverse Momentum of Target Constituents

Other effects also contribute to R. If the target particle has a transverse momentum distribution with respect to the photon direction a finite R value will result even if the target particle has zero mass.(15) The argument for this effect is most clearly demonstrated in the Breit frame with spin ½, massless particles. In Fig. 15, both the cases of zero P_t and finite P_t is sketched. Since these particles can only have one helicity, spin flip must occur for zero P_t. Hence, only photons that have $|J_Z| = 1$ will be absorbed and σ_L will be zero. Similarly, if the target particle has spin zero, only $J_Z = 0$ photons can interact and σ_T will be zero.

Now consider what happens when the target particle has some transverse momentum with respect to the photon's momentum. Spin projection results in an amplitude proportional to $\sin(\theta/2)\cos(\theta/2)$ where $\theta \sim P_t/P_z$. In this way one finds $R \propto {P_t}^2/Q^2$. The transverse momentum distribution for quarks inside nucleons can arise simply from the fact that quarks are bound. This is sometimes referred to as "primordial" transverse momentum.

Effects of QCD on R

In QCD, quarks may also have transverse momentum due to gluon emission. Also at low x quark-antiquark pairs from gluons have transverse momentum.

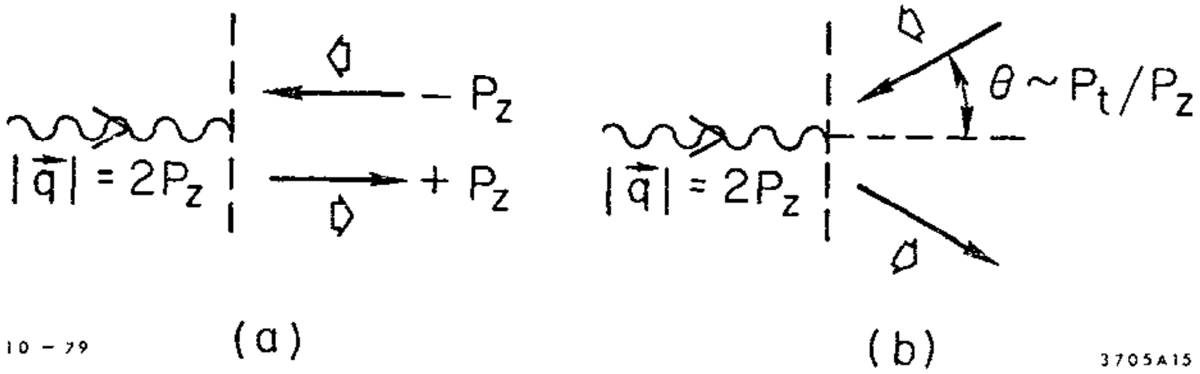

Figure 15. Effect of transverse momentum (P_t) of target particle. Scattering is depicted in the Breit frame.

The QCD effects can be parameterized as

$$R_{QCD} = \alpha_s(Q^2)\ r(x,Q^2), \tag{58}$$

where the function $r(x,Q^2)$ is predicted to be large at small x and small at large x. $r(x,Q^2)$ to lowest order in QCD is proportional to integrals over both F_2 and the gluon distribution.(16) An example of an approximate form for R_{QCD} used by the CHIO collaboration is

$$R_{QCD} = R_o(1 - x)/\ln\left(\frac{Q^2}{\Lambda^2}\right) \tag{59}$$

It differs from the previous expressions for R in that it falls as $1/\ln(Q^2/\Lambda^2)$ rather than $1/Q^2$. This formula predicts a large R_{QCD} at small x, but is unreliable in this region due to uncertainties in the gluon distribution and unaccounted for higher order corrections. There seems to be no theory that has combined the three effects discussed above into one formula which may be compared with the data. As such we should not be surprised if each by itself does not work well.

4.2. Measurement of R in Charged Lepton - Nucleon Scattering

For the data taken at SLAC the following procedure has been used to extract R in a model independent manner. First the data is binned in W^2 and Q^2 (typically the bin size is a few GeV^2). Data taken at different E_o's and θ's will have different values of ε. With the cross section given by Eq. 46, data at fixed W^2 and Q^2 should exhibit a linear behavior on an ε plot. Such a plot is shown in Fig. 16. The intercept of a

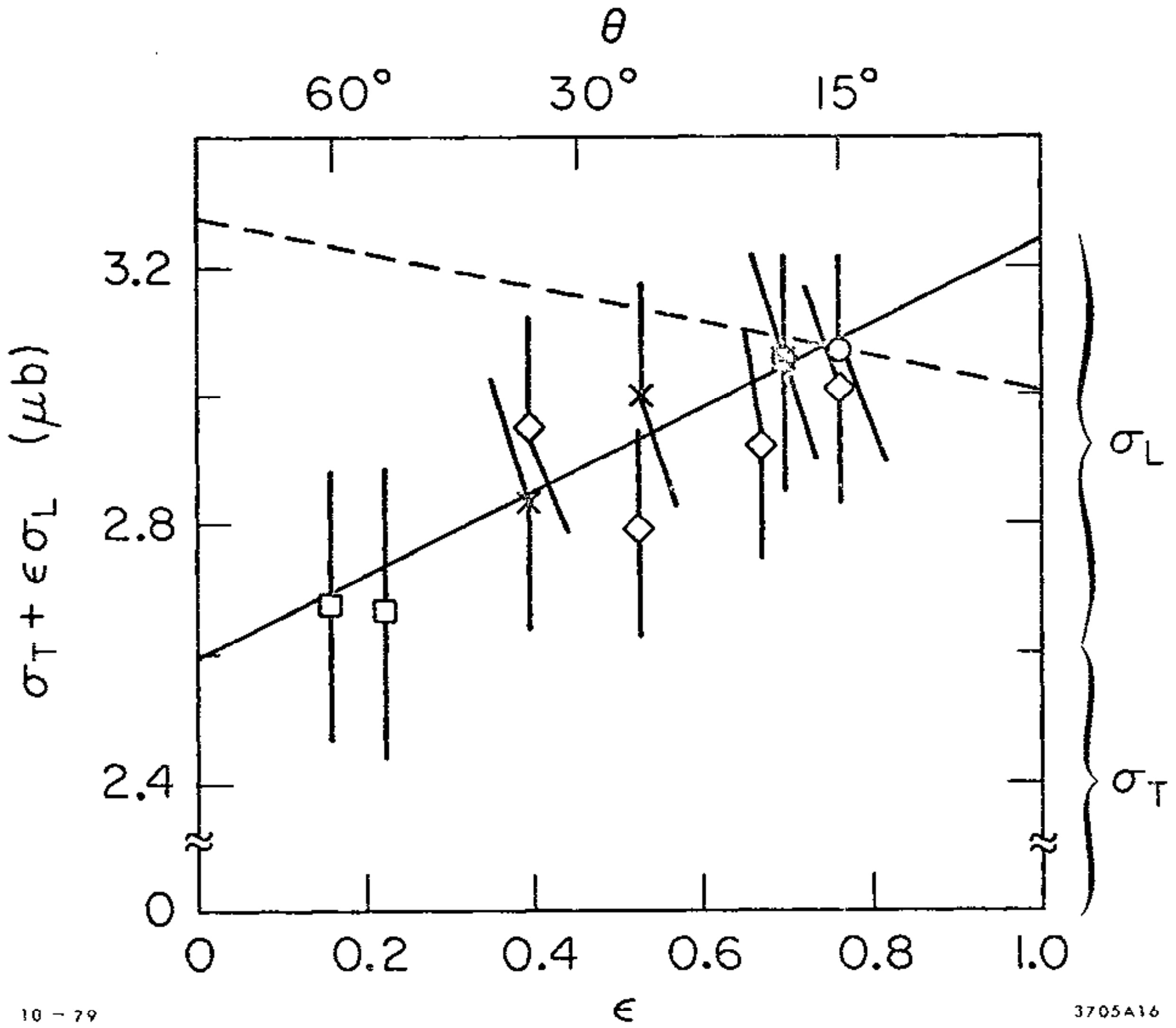

Figure 16. ε plot. ep scattering cross section versus ε for one bin in Q^2 and W^2. $Q^2 \approx 9$ GeV^2 and $W^2 \approx 7$ GeV^2.

straight line fit at $\varepsilon = 0$ is σ_T and the intercept at $\varepsilon = 1$ is $\sigma_T + \sigma_L$. The slope of the line on the ε plot is proportional to R.

The accuracy of the values of R so obtained depend on the range of the data in ε for the W^2, Q^2 bin being fitted and the errors associated with this data. For the SLAC data, each of the three spectrometers used in the experiments covers different ranges on the ε plot: large angles or low scattered energy corresponds to small ε, and vice versa. Thus to get the maximum range in ε, one combines the data from all three spectrometers. The inter-calibration of the spectrometers' acceptances is a major source of systematic error when this is done.

The radiative corrections applied to the SLAC data are another source of systematic error. If one were to make ε-plots for the uncorrected data in some W^2 and Q^2 bins, they would appear to decrease with increasing ε, e.g. the dashed line in Fig. 16. The resulting R value would be negative! The radiative corrections for most SLAC data are not large (typically $\leq 20\%$) but R is very sensitive to the values of the cross sections. This is because the measured cross sections are mostly σ_T with a small σ_L contribution.

The data from SLAC is shown in a grid of W^2 and Q^2 bins in Fig. 17. The vertical scales on each plot have been adjusted so that $R = 0.5$ would be a 45 degree line. The error shown on the data points includes systematic errors. R is seen to have a small but finite value in the SLAC kinematic region. Fitting R to a single number, indicated by the

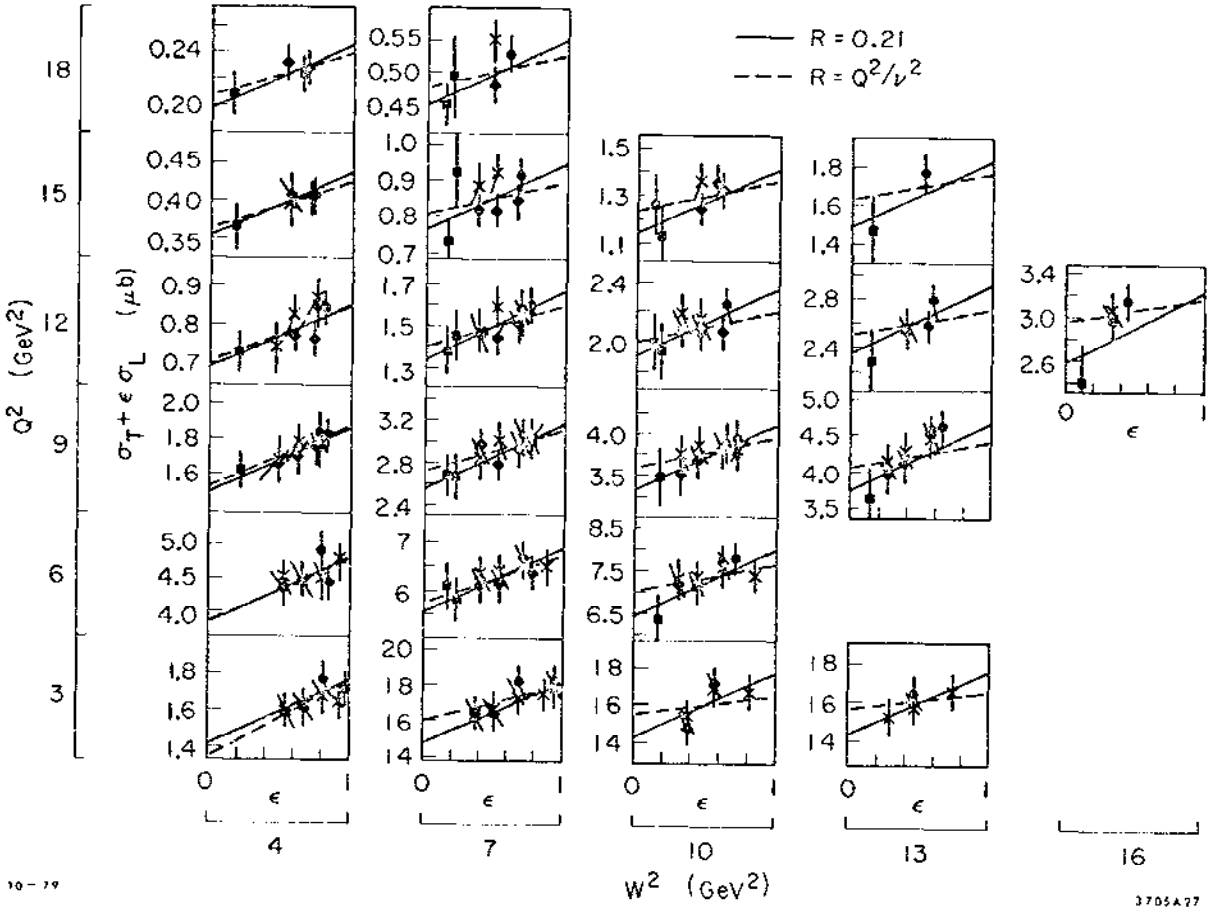

Figure 17. ε plots for the Q^2, W^2 range of SLAC. R = 0.5 would be a line of slope 45 degrees.

solid lines in Fig. 17, gives R = 0.21 ± 0.1. The error is mostly systematic - the statistical error is negligible. No significant trend has been established with either Q^2 or x.(17) Only near the boundry of the SLAC region does the value of R seem to increase (high W^2 and high Q^2), but these points, with their larger radiative corrections, are more suspect. For comparison, the Callan-Gross prediction for R is indicated in Fig. 17 by the dashed lines.

R has also been measured using the muon data of the CHIO collaboration. This data is not of sufficient statistical strength to pursue an ε plot analysis. Instead the experimenters used a global fit to all their data assuming a functional form for $F_2(x,Q^2)$ and various forms for R. For a constant R, their best fit gives R = 0.52 (+ 0.17, - 0.15) (± 0.35) where the first errors are statistical and the second error is the systematic error. This muon data is weighted heavily at low x and small Q^2 ($\langle x\rangle \sim 0.05$ and $\langle Q^2\rangle \sim 2\,\mathrm{GeV}^2$). One might think that this is the effect of QCD - higher R at lower x, but the systematic error is too large to definitely establish this trend.

4.3. R in Neutrino - Nucleon Scattering

For neutrino scattering we need to develop some more phenomenology. The usual structure functions can be rewritten in terms of left handed, right handed and scalar structure functions:

$$F_L^{\nu} = 2xF_1 + xF_3 \text{ (quark scattering)}, \tag{60.1}$$

$$F_R^{\nu} = 2xF_1 - xF_3 \text{ (antiquark scattering)}, \tag{60.2}$$

and

$$F_s^{\nu} = F_2 - 2xF_1 \quad \text{(scalar particle scattering)}. \tag{60.3}$$

The cross section, in terms of these structure functions, is

$$\frac{d\sigma^{\nu,\bar{\nu}}}{dxdy} = \frac{G^2}{\pi}\left(\frac{ME_o}{2}\right)\left[F_{L,R}(x,Q^2) + (1-y)^2\ F_{R,L}(x,Q^2) + 2(1-y)F_s(x,Q^2)\right]. \tag{61}$$

This expression corresponds to Eq. 46 in the case of electron (muon) scattering. Thus y plots for neutrinos are like ε plots for electrons, but the data on a y plot have a quadratic instead of linear behavior. We may define, in analogy to Eq. 51, the quantity:

$$R_{\nu} \equiv 1 - \frac{2xF_1}{F_2} = \frac{R - r_c}{R + 1} \quad . \tag{62}$$

R_{ν} measures the deviation from the Callan-Gross relation and when compared with R used in electro-production and muon-production experiments must be modified using

$$R = \frac{R_{\nu} + r_c}{1 - R_{\nu}} \quad . \tag{63}$$

The CDHS collaborators have performed an R analysis using their charged current neutrino data by measuring the term proportional to (1 - y) in the data. In their first analysis, fits were made to terms proportional to a constant, $(1 - y)$ and $(1 - y)^2$, over the full x and Q^2 range of the data. The result was $R_\nu = - 0.03 \pm 0.04$.

In a second analysis they binned the data in E_{HAD} (i.e. ν). This results in bins that cover their full x range and a portion of the Q^2 range depending on E_{HAD} (recall $Q^2 = 2M\nu x$ and $0 < x < 0.7$ for the CDHS data). By fitting each bin, a value for R_ν was found. These values are shown in Fig. 18. At low E_{HAD}, R_ν is small but increases with increasing E_{HAD}. All of these values, when taken with their systematic errors, are consistent with the small value of R predicted by QCD for this high Q^2 region.

The BEBC collaboration have pursued an analysis more similar to the ε plot techniques used in analyzing the SLAC data.$^{(18)}$ The averages of neutrino and anti-neutrino cross sections are binned in x and Q^2 and then fit to a form

$$\frac{1}{2}\left(\frac{d\sigma^{\nu}}{dxdQ^2} + \frac{d\sigma^{\bar{\nu}}}{dxdQ^2}\right) \propto \left(1 - y - \frac{M^2x^2y^2}{Q^2}\right)F_2(x,Q^2) + \frac{y^2}{2}2xF_1(x,Q^2) \qquad (64)$$

which is suggested by Eq. 27. By fixing both x and Q^2, this analysis becomes model independent like the SLAC analysis. Unfortunately the bins are large due to the limited statistics. They find $R = 0.15 \pm 0.10 \pm 0.04$ where the first error is statistical and the second is systematic.

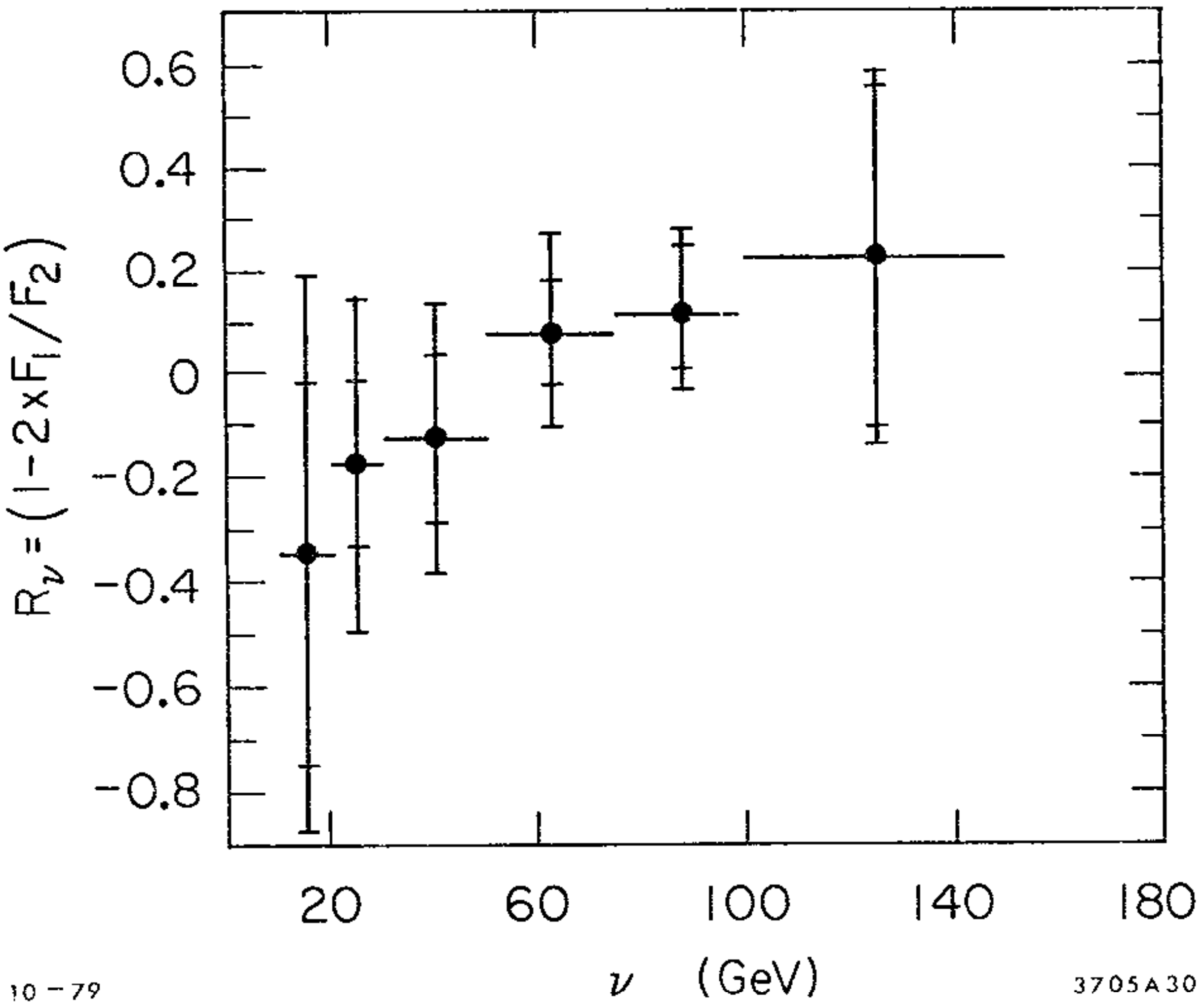

Figure 18. R_ν, the deviation from the Callan-Gross relation, versus $\nu = E_o - E'$ for neutrino - iron scattering.

4.4. Summary and Conclusions on R

To conclude this section, I have plotted the R values from the SLAC, CHIO, and BEBC analyses versus x in Fig. 19. The CDHS measurement was not plotted as it is at much higher Q^2. The BEBC point and the CHIO point were plotted at representative values of x for their respective data sets. The family of solid curves represents $R_{QCD}^{(32)}$ calculated for $3 \text{ GeV}^2 < Q^2 < 18 \text{ GeV}^2$ which is the Q^2 range covered by the SLAC data. The dashed line shows the value of r_c for the average Q^2 of each SLAC data point. The consistently large value of R found in the SLAC data at high x should not be interpreted as posing a serious problem for QCD. The error bars shown are highly correlated point-to-point and the ensemble can only be counted as about 2 standard deviations off from the pure QCD prediction. The $1/Q^2$ terms mentioned earlier would also improve the agreement between experiment and theory.

My present conclusions concerning R are:

1. The Callan-Gross relation works well enough: to assume $2xF_1 = F_2$ in extracting F_2 from cross section measurements probably doesn't result in a large error.

2. The first order QCD calculation for R is in mild disagreement with the data at high x. At present the data are not good enough to see the predicted rise at small x or the overall $1/\ln(Q^2/\Lambda^2)$ dependence.

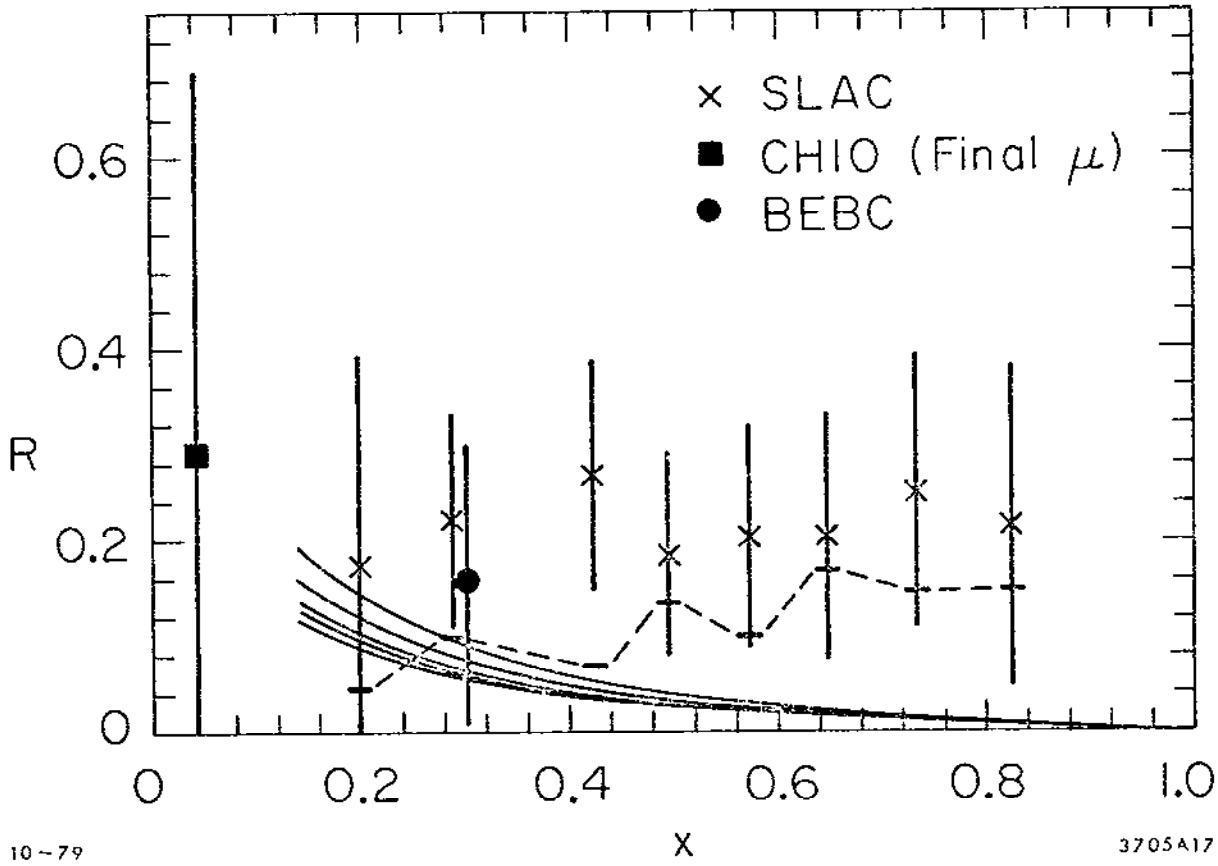

Figure 19. $R = \sigma_L/\sigma_T$ versus x for BEBC, CHIO, and SLAC. The solid curves are R_{QCD}; dashed curve is $R = r_c$ for $\langle Q^2 \rangle$ of each SLAC data points.

3. The SLAC, CHIO and BEBC data are mutually consistent. The CDHS data is typically at much higher Q^2 and, therefore, not directly comparable. However QCD and the Callan-Gross relation prediction that R should decrease with increasing Q^2 are not inconsistent with the lower value of R extracted from the CDHS data.

5. PROTON FORM FACTOR IN ELASTIC ep SCATTERING

In this section I discuss tests of QCD in the context of ep elastic scattering and ep deep inelastic scattering very near the elastic limit. In the former case there is a prediction for the elastic form factor from quark counting.(19) The latter case may be related to elastic scattering by the Drell-Yan and West relation.(20)

5.1. Definition of the Form Factor G_M

The cross section for elastic scattering can be expressed in terms of an electric and a magnetic form factor (G_E and G_M):

$$\frac{d\sigma}{dQ^2} = \frac{4\pi\alpha^2}{Q^4}\left[\left(1-y-\frac{My}{2E_o}\right)\frac{2MG_E{}^2(Q^2) + yE_oG_M{}^2(Q^2)}{2M + yE_o} + \frac{y^2}{2}G_M{}^2(Q^2)\right] \quad (65)$$

This expression can be rewritten using $R_{el}\left(= r_c\,\frac{G_E{}^2}{G_M{}^2}\right)$ as

$$\frac{d\sigma}{dQ^2} = \frac{4\pi\alpha^2}{Q^4}G_M{}^2(Q^2)\left[\left(1-y-\frac{My}{2E_o}\right)\frac{R_{el}+1}{r_c+1} + \frac{y^2}{2}\right] \quad (66)$$

Assuming form factor scaling as in Eq. 55, one can then estimate R_{el}:

$$R_{el} = \frac{4M^2}{Q^2} \frac{1}{\mu_p^2} \tag{67}$$

(for protons $R_{el} = \frac{0.45}{Q^2(\mathrm{GeV}^2)}$). Using this estimate in the elastic cross section expression shows that G_E contributes little to elastic scattering for $Q^2 > 5$ GeV^2. In practice the measured cross sections are reduced to measurements of $G_M(Q^2)$ using the form factor scaling assumption.

5.2. Effect of Simple Gluon Exchange and QCD

We can develop a phenomenological model for $G_M(Q^2)$ by noting that the struck quark must share the momentum absorbed from the photon with the other quarks inside the nucleon.$^{(19)}$ One such possible process is sketched in Fig. 20. In a three quark nucleon there must be at least two gluon exchanges. Counting propagators and vertices one would expect:

$$G_M(Q^2) \propto \left(\frac{\alpha_s(Q^2)}{Q^2}\right)^2 . \tag{68}$$

This behavior should become dominant at high Q^2 but in the region where data exists $\alpha_s(Q^2)$ is still large (see Table 2) and higher order effects are undoubtedly important.

The elastic form factor data obtained from the SLAC experiments covers the Q^2 range of ~ 0 GeV^2 to 33.4 GeV^2. To reduce the large variation in $G_M(Q^2)$ over the range in Q^2, $Q^4 G_M(Q^2)/\mu_p$ is plotted in Fig. 21. The expected $1/Q^4$ behavior is substantiated by the data for 5 GeV^2 $< Q^2 <$ 33.4 GeV^2 (i.e. for $Q^2 > 5$ GeV^2, $Q^4 G_M(Q^2)$ is approximately independent of Q^2).

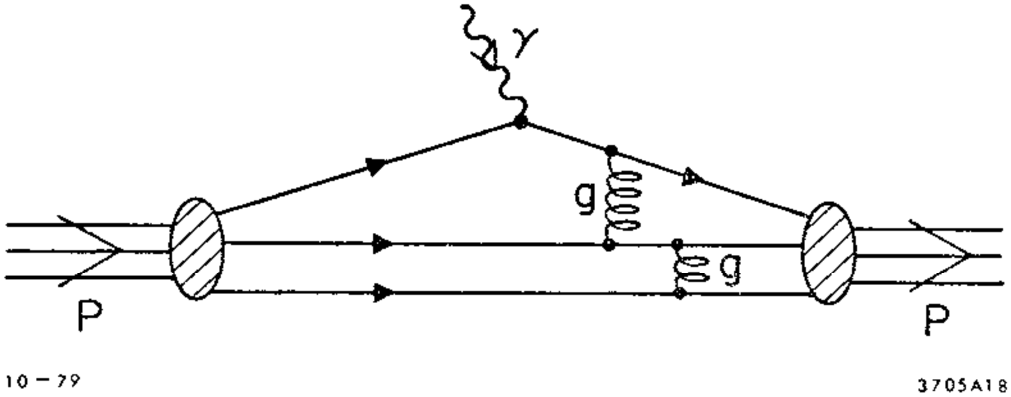

Figure 20. Picture of elastic scatter of a photon from a proton. Exchange of two or more gluons is needed to achieve an elastic scatter.

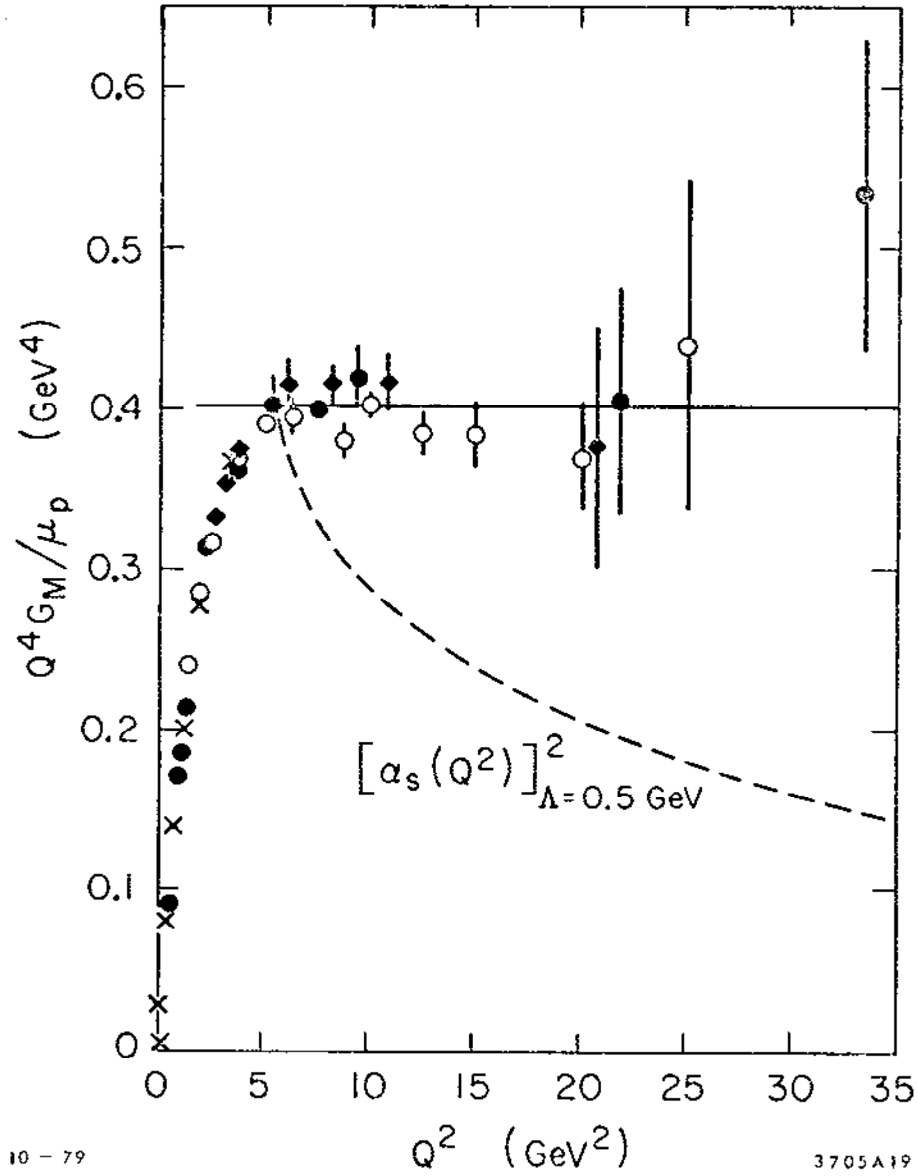

Figure 21. Elastic form factor for ep scattering versus Q^2. Data has been multiplied by Q^4 to reduce its dynamic range. Dashed curve is the QCD prediction.

QCD Effects

The principle QCD expectation is that $Q^4 G_M(Q^2)$ should fall as $(\alpha_s(Q^2))^2$. The dashed line in Fig. 21 shows $(\alpha_s(Q^2))^2$ normalized to agree with the data at $Q^2 = 5$ GeV^2. The large discrepancy between this QCD expectation and the data may come from a variety of sources. First, a more exact calculation gives a slightly different (and much more complicated) form for $G_M(Q^2)$.(21) This calculation does not improve the agreement between experiment and theory. Higher order corrections also will contribute as $\alpha_s(Q^2)$ is still quite large in this Q^2 region. Also, corrections of order $1/Q^2$ to this prediction could improve the comparison with the data, but theorists are at present unable to make firm predictions as to their relative magnitude or even their analytic form.

5.3. Summary and Conclusions on G_M

The conclusions reached about elastic ep scattering are:

1. The magnetic form factor obeys the power law behavior expected from simple gluon exchange: $G_M(Q^2) \sim 1/Q^4$. A different power law would have resulted in enormous effects over the available Q^2 range.

2. However the fall off predicted by QCD due to the running coupling constant is not observed.

An aside: we have now seen three ways to count (valence) quarks in the nucleon and each one has indicated 3 quarks. They are: 1) the "quasi-elastic" peak in $F_2^{ep} - F_2^{en}$; 2) the GLS sum rule: $\int F_3 dx \approx 3$; and 3) the power law for elastic ep scattering.

5.4. Drell - Yan and West Relation in the Threshold Region

This relationship predicts that the power of $1/Q^2$ in elastic scattering should be related to the power of $(1 - x)$ in the inelastic structure functions as x nears 1. In this region, the mass of the out going hadronic system is small. As in the case of ep elastic scattering, gluon exchanges must occur to share the momentum impact of the virtual photon (or W boson) among the nucleon's constituents. As such the relative strengths of these two processes should track in Q^2.

Since the expression for the elastic piece of F_2 contains a delta function, we need to compare integrals of F_2 for the elastic and the inelastic. First consider the elastic piece derived from Eq. 53.1:

$$\int_{x_L}^{1} F_{2el}(x,Q^2)dx = \frac{2MG_E{}^2(Q^2) + yE_oG_M{}^2(Q^2)}{2M + yE_o} \approx G_M{}^2(Q^2) \qquad (69)$$

where the lower limit of the integral, x_L, is close to 1. Now consider the inelastic part of F_2. It is parameterized as $(1 - x)^k$ for x near 1. So, integrating this function from a fixed mass, W_L, to threshold means the lower limit of the integral will behave as

$$x_L = 1 - \frac{W_L^2 - M^2}{Q^2} \doteq 1 - \frac{\Delta M^2}{Q^2} \qquad (70)$$

Then,

$$\int_{x_L}^{1} F_2(x,Q^2)\ dx \ \propto \int_{x_L}^{1} (1-x)^k\ dx \propto - \left.(1-x)^{k+1}\right|_{x_L}^{1} \propto \left(\frac{\Delta M^2}{Q^2}\right)^{k+1} . \qquad (71)$$

The results of the last section showed that the elastic form factor behaved as $(1/Q^2)^{n-1}$ where n is the number of quarks in the nucleon. Equating the two integrals gives the desired relation:

$$G_M{}^2(Q^2) \propto \left(\frac{1}{Q^2}\right)^{2(n-1)} \propto \left(\frac{\Delta M^2}{Q^2}\right)^{k+1} \qquad (72)$$

and thus $k = 2n-3$. This is the Drell-Yan and West relation$^{(20)}$ and states that if the elastic form factor behaves as $(1/Q^2)^{n-1}$, then $F_2(x)$ should behave as $(1 - x)^{2n-3}$ for x near 1. Specifically if $G_M(Q^2) \propto \frac{1}{Q^4}$, then $F_2(x) \propto (1 - x)^3$.

Note that, although the DYW relation can be motivated by gluon considerations, it is actually predicted on arguments that do not require gluons.$^{(20)}$ As such, it should not be interpreted as a test of QCD.

Comparison with the Data

In Fig. 22a I have plotted the quantity $F_2{}^{ep}(x,Q^2)/(1 - x)^3$ in analogy to the Q^4G_M plot of Fig. 21. The data have been binned for various values of Q^2 and are plotted against x. Each Q^2 bin stops where W dips below 1.8 GeV. The expected flat lines are not observed!

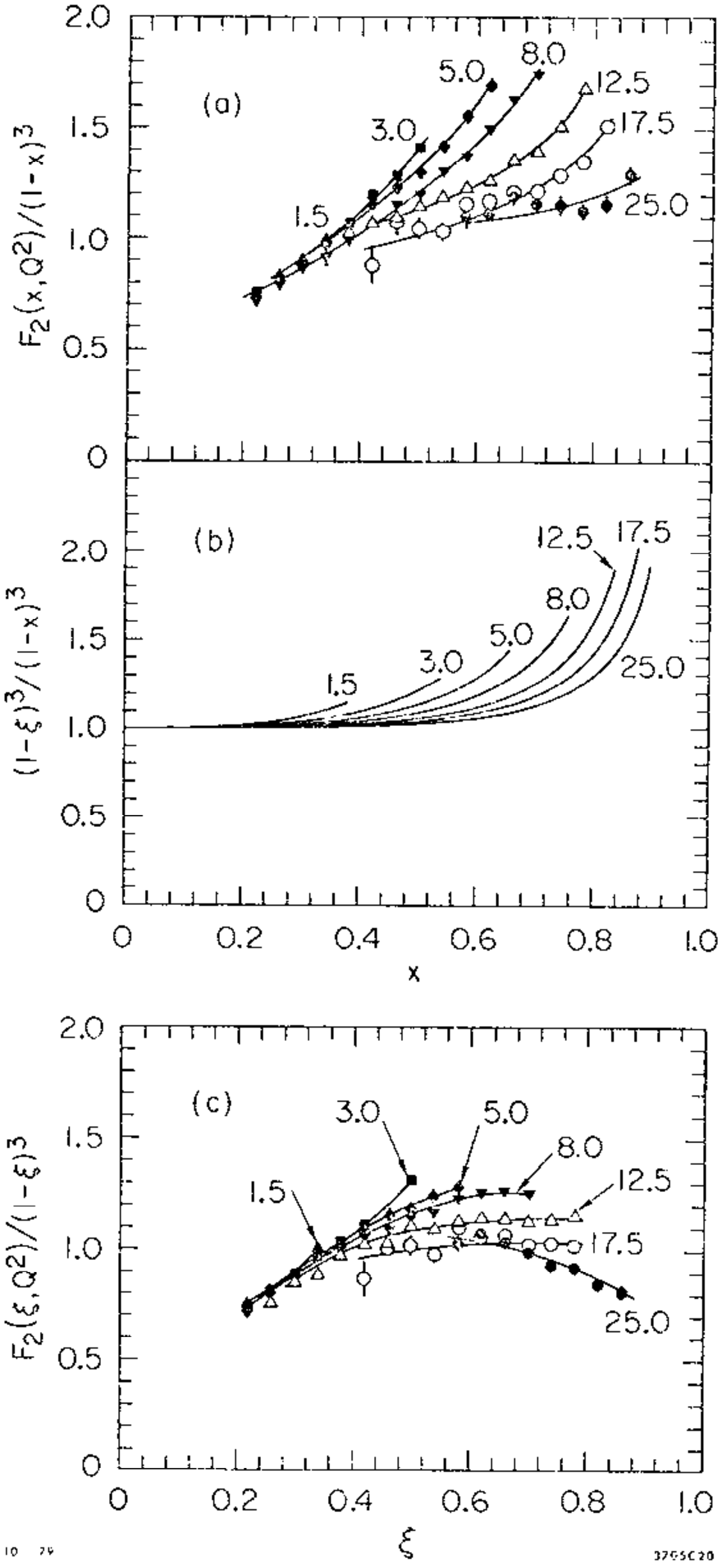

Figure 22. Drell-Yan and West relation in ep scattering. a) in terms of the variable x, b) variables x and ξ contrasted, and c) in terms of the variable ξ.

In Sec. 2 when the scaling variables were introduced it was emphasized that there existed some ambiguity which could result in large effects at low Q^2. The Nachtmann variable ξ (Eq. 15) was introduced as a possible alternative to the variable x. In Fig. 22b, the effect of the x variable versus the ξ variable is shown. Plotted is $(1 - \xi)^3/(1 - x)^3$ for the same values of Q^2 presented in Fig. 22a. This suggests plotting $F_2^{ep}(\xi,Q^2)/(1 - \xi)^3$ (see Fig. 22c). The ξ variable produces flatter Q^2 contours, but still a systematic trend is seen. For low Q^2, the best power is less than 3 while at higher Q^2 the power is greater than 3. It may be pointless at this time to seek a "correct" scaling variable: the data seem to indicate a definite violation of scaling.

An alternative explanation of the behavior seen in Fig. 22c comes from QCD. An approximate form for the structure function predicted using QCD results in the power of (1 - x) increasing with increasing Q^2.(22) The systematic shifting of the x distributions from high x to low x with increasing Q^2 (see Sec. 3.2) produces an exponent of (1 - x) that increases as the $\ln(\ln(Q^2/\Lambda^2))$.

The conclusions concerning the threshold region and the Drell-Yan and West relation are:

1. The comparison of elastic scattering with deep-inelastic scattering through the DYW relation is indecisive and depends on the scaling variable.

2. Using the ξ variable results in a behavior of F_2 consistent with the QCD expectation of high x shifting to low x as Q^2 increases.

6. DEPENDENCE OF STRUCTURE FUNCTIONS ON Q^2

QCD predicts that the nucleon structure functions should show scale breaking effects due to the running coupling constant. This section contains a discussion of these effects in the context of lepton-nucleon scattering experiments.

6.1. The Evolution Equation for the Structure Functions

The unpaired quarks inside the nucleon, the valence quarks, are the simplest to study. The probability distributions for these "flavor non-singlets" should show QCD distortions coming only from gluon bremsstrahling as in Fig. 12a. The $q - \bar{q}$ quark pairs ("flavor singlets") have additional contributions coming from pair production off gluons as in Fig. 12b and are thus more complicated (i.e. both the quark distribution and the gluon distribution enter the equations).

The non-singlet quark distribution has a Q^2 dependence arising from the following mechanism. At low Q^2 a distribution of non-singlet quarks is observed ($xF_3(x,Q^2)$ for example). The distance scale on which this quark distribution is being probed is large. The continual emission and re-absorption of virtual gluons is hidden. But at larger Q^2 the distance scale shrinks. These quarks are now sometimes "resolved" into a quark and a gluon. The gluons thus bremsstrahled take with them a portion of the quark's momentum and the quark is more likely to be at lower x. In pictures this process is shown in Fig. 23a.

The equation describing this situation is:

$$Q^2 \frac{d}{dQ^2} q^{NS}(x,Q^2) = \frac{\alpha_s(Q^2)}{2\pi} \int_x^1 \frac{dw}{w} q^{NS}(w,Q^2)\ P_{qq}(\tfrac{x}{w}) \quad . \tag{73}$$

In other words, the fractional change in the quark distribution $q(x,Q^2)$ is equal to the integral over all quark states that can contribute (i.e. $x < y < 1$) times the splitting function ($P_{qq}(\frac{x}{w})$) for the quark to emit a gluon which carries off a fraction z (= x/w) of the quark's momentum. In particular, the form of $P_{qq}(z)$ [23] for spin 1 particles is:

$$P_{qq}(z) = \frac{4}{3} \left[\frac{1 + z^2}{(1-z)_+} + \frac{3}{2}\, \delta\ (z - 1) \right] \tag{74.1}$$

where $(1 - z)_+$ is defined by:

$$\int_0^1 dz\ \frac{f(z)}{(1-z)_+} \equiv \int_0^1 dz\ \frac{f(z) - f(1)}{(1 - z)} \quad . \tag{74.2}$$

Notice that I called $P_{qq}(z)$ a splitting function and not a probability distribution. It can be related to the probability of a quark to radiate a gluon minus the probability of anti-quark to radiate a gluon. In particular, it has properties that no self-respecting probability distribution would have:

$$\int_0^1 dz\ P_{qq}(z) = 0 \tag{75.1}$$

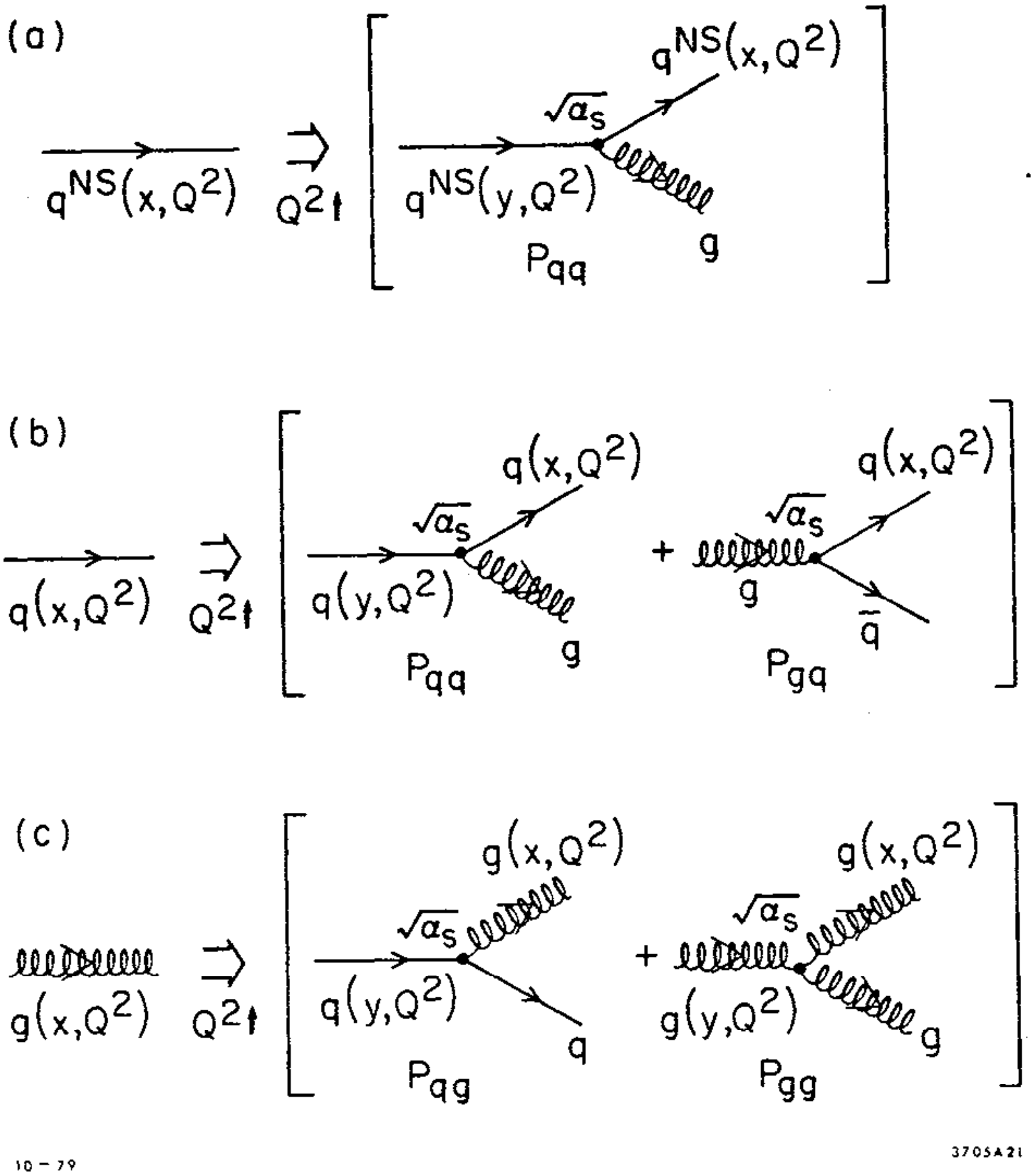

Figure 23. QCD processes which modify quark distributions: a) flavor non-singlet (valence) quarks, b) flavor singlet ("sea") quarks.

and

$$\int_0^1 dz\, z^{n-1}\, P_{qq}(z) < 0 \text{ for } n > 1\,. \qquad (75.2)$$

The flavor singlet case is more complicated and I discuss this only for the sake of completeness. Both the quark and the gluon distributions contribute and two coupled integrodifferential equations result (see Fig. 23b and 23c). The corresponding equations are

$$Q^2 \frac{d}{dQ^2}\, q(x,Q^2) = \frac{\alpha_s(Q^2)}{2\pi} \int_x^1 \frac{dw}{w} \left[q(w,Q^2)\, P_{qq}\left(\tfrac{x}{w}\right) + g(w,Q^2)\, P_{gq}\left(\tfrac{x}{w}\right) \right] \qquad (76.1)$$

and

$$Q^2 \frac{d}{dQ^2}\, g(x,Q^2) = \frac{\alpha_s(Q^2)}{2\pi} \int_x^1 \frac{dw}{w} \left[q(w,Q^2)\, P_{qg}\left(\tfrac{x}{w}\right) + g(w,Q^2)\, P_{gg}\left(\tfrac{x}{w}\right) \right] \qquad (76.2)$$

There are four splitting functions in these equations relating quarks to gluons and two distributions, one for quarks and the other for gluons. The gluon distribution cannot be measured directly in deep inelastic scattering and must be inferred by solving the above coupled equations.

QCD makes specific predictions for all four of these splitting functions. The resulting equations are analogous to the old Weizacker-Williams bremsstrahlung and e^+e^- pair creation formulas. The evolution of the quark and gluon x distributions with increasing Q^2 is thus well specified in QCD. The x distributions themselves are not predicted.

In the rest of this talk I will concentrate on the results of the flavor non-singlet case (Eq. 73). I will give three examples of how it has been used to compare QCD with the data. The first example will be the now (in)famous QCD moments. The second approach (formulated by Buras and Gaemers)(22) is to make a guess for the x, Q^2 distribution that satisfy the evolution equation and then fit this form to the data. The third method (developed by Abbott and Barnett)(24) uses numerical techniques to solve the differential equation and fit the evolved x distribution to the data.

Note that the common thing being tested here is the inevitable process of bremsstrahlung as shown in Fig. 12. As such Eq. 73 and Eq. 76 are perhaps not as much a result of QCD in particular as they are a result of any quark theory with gluons.(25)

6.2. Moments of Structure Functions and their Q^2 Dependence

The Moment Method

The integrodifferential equation for the non-singlet quark distribution is given by Eq. 73. To separate out the effects of the splitting function $P_{qq}(z)$, for which QCD makes an explicit prediction, multiply both sides by x^{n-1} and integrate over x from 0 to 1:

$$Q^2 \frac{d}{dQ^2} \int_0^1 x^{n-1}\, q^{NS}(x,Q^2)\, dx = \frac{\alpha_s(Q^2)}{2\pi} \int_0^1 x^{n-1}\, dx \int_x^1 \frac{dw}{w}\, q^{NS}(w,Q^2)\, P_{qq}\left(\frac{x}{w}\right). \quad (77)$$

Interchanging the order of integration on the R.H.S. and defining

$$M_{NS}(Q^2,n) \equiv \int_0^1 x^{n-1}\, q^{NS}(x,Q^2)\, dx \quad (78)$$

gives

$$Q^2 \frac{d}{dQ^2} M_{NS}(Q^2,n) = \frac{\alpha_s(Q^2)}{2\pi} \int_0^1 \frac{dw}{w}\, q^{NS}(w,Q^2) \int_w^1 dx\; x^{n-1}\, P_{qq}\left(\frac{x}{w}\right). \tag{79}$$

With the substitution z = x/w and the definition

$$A(n) = \int_0^1 dz\; z^{n-1}\, P_{qq}(z) \tag{80}$$

this equation becomes

$$Q^2 \frac{d}{dQ^2} M_{NS}(Q^2,n) = \frac{\alpha_s(Q^2)}{2\pi} M_{NS}(Q^2,n)\; A(n). \tag{81}$$

Success! We have a linear differential equation for the moments $M_{NS}(Q^2,n)$. The calculable A(n) appears as a coefficient in this differential equation. Using Eq. 42 for $\alpha_s(Q^2)$ leads to the solution

$$M_{NS}\ (Q^2,n) = \frac{C}{\left[\ln\left(\frac{Q^2}{\Lambda^2}\right)\right]^{d_n}} \tag{82}$$

where C is a constant and

$$d_n = \frac{-A(n)}{2\pi B} \tag{83}$$

with B as in Eq. 40. The d_n are called the "anomalous dimensions" of the non-singlet quark distributions. Hence the QCD prediction is that the moments of the non-singlet structure functions should vary as calculable, inverse powers of $\ln(Q^2/\Lambda^2)$.

Integrating Eq. 80 for P_{qq} as in Eq. 74 yields:

$$A(n) = -\frac{2}{3}\left[1 - \frac{2}{n(n+1)} + 4\sum_{j=2}^{n} \frac{1}{j}\right] . \tag{84}$$

And with the choice of $N_f = 4$ in Eq. 40, d_n becomes:

$$d_n = \frac{4}{25}\left[1 - \frac{2}{n(n+1)} + 4\sum_{j=2}^{n}\frac{1}{j}\right] . \tag{85}$$

The power law predictions are often compared to the data by noting

$$\frac{d(\ln M_{NS}(Q^2,n))}{d(\ln M_{NS}(Q^2,m))} = \frac{A(n)}{A(m)} = \frac{d_n}{d_m} . \tag{86}$$

This equation indicates that on a log-log plot of the n^{th} moment versus the m^{th} moment, a straight line will result with a slope given by the ratio of the n^{th} to m^{th} anomalous dimension. It is worthwhile emphasizing that the straight line and its slope are a consequence merely of the bremsstrahlung of vector gluons by quarks. But what would constitute a more telling test of QCD (and Eq. 79) is to plot $M_{NS}(Q^2,n)^{-1/d_n}$ versus $\ln(Q^2)$,(26) since

$$M_{NS}(Q^2,n)^{-1/d_n} \propto \ln\left(\frac{Q^2}{\Lambda^2}\right) . \tag{87}$$

There are two possible sources of data with which to perform a non-singlet moment analysis: 1) $xF_3(x,Q^2) = x\left[q(x,Q^2) - \bar{q}(x,Q^2)\right]$ from the difference of neutrino and anti-neutrino scattering and 2) $F_2^{ep}(x,Q^2) - F_2^{en}(x,Q^2)$ from electron (muon) scattering off hydrogen and deuterium. For 2) the flavor symmetric parts (the "sea") of the proton should be subtracted out by an equal contribution in the neutron. The data for these structure functions is binned in Q^2. Moments are formed by summing the data in each bin weighted with powers of x. Here's where the problems begin.

Problems of the Moment Method

Choice of Scaling Variable

First, what scaling variable should be used? The original Cornwall-Norton$^{(27)}$ moments defined by

$$M_i(Q^2,n) = \int_0^1 x^{n-2} F_i(x,Q^2)\,dx \quad (i = 1,2, \text{ and } 3) \tag{88}$$

use the x variable as in Eq. 78. The Nachtmann moments$^{(28)}$ on the other hand use the ξ variable of Eq. 15:

$$M_2(Q^2,n) = \int_0^1 dx\, \frac{\xi^{n+1}}{x^3} \frac{\left[n^2+2n+3+3(n+1)\sqrt{1+r_c}+n(n+2)r_c\right]}{(n+2)(n+3)} F_2(x,Q^2) \tag{89.1}$$

and

$$M_3(Q^2,n) = \int_0^1 dx\, \frac{\xi^{n+1}}{x^3} \frac{\left[1+(n+1)\sqrt{1+r_c}\right]}{n+2} x\, F_3(x,Q^2). \tag{89.2}$$

At large Q^2, the Nachtmann and the Cornwall-Norton moments converge to the same value, but at low values of Q^2 large differences occur. At present the safest bet is to trust neither when the results differ significantly.

In Fig. 24, the fourth moment of $F_2^{ep} - F_2^{en}$ for the Cornwall-Norton and the Nachtmann prescriptions is plotted against Q^2. Below Q^2 of about 5 GeV^2 the two give very different results. This situation becomes worse with increasing moment number since the high x part of the structure functions are weighted more and more heavily (recall the ξ and x variables

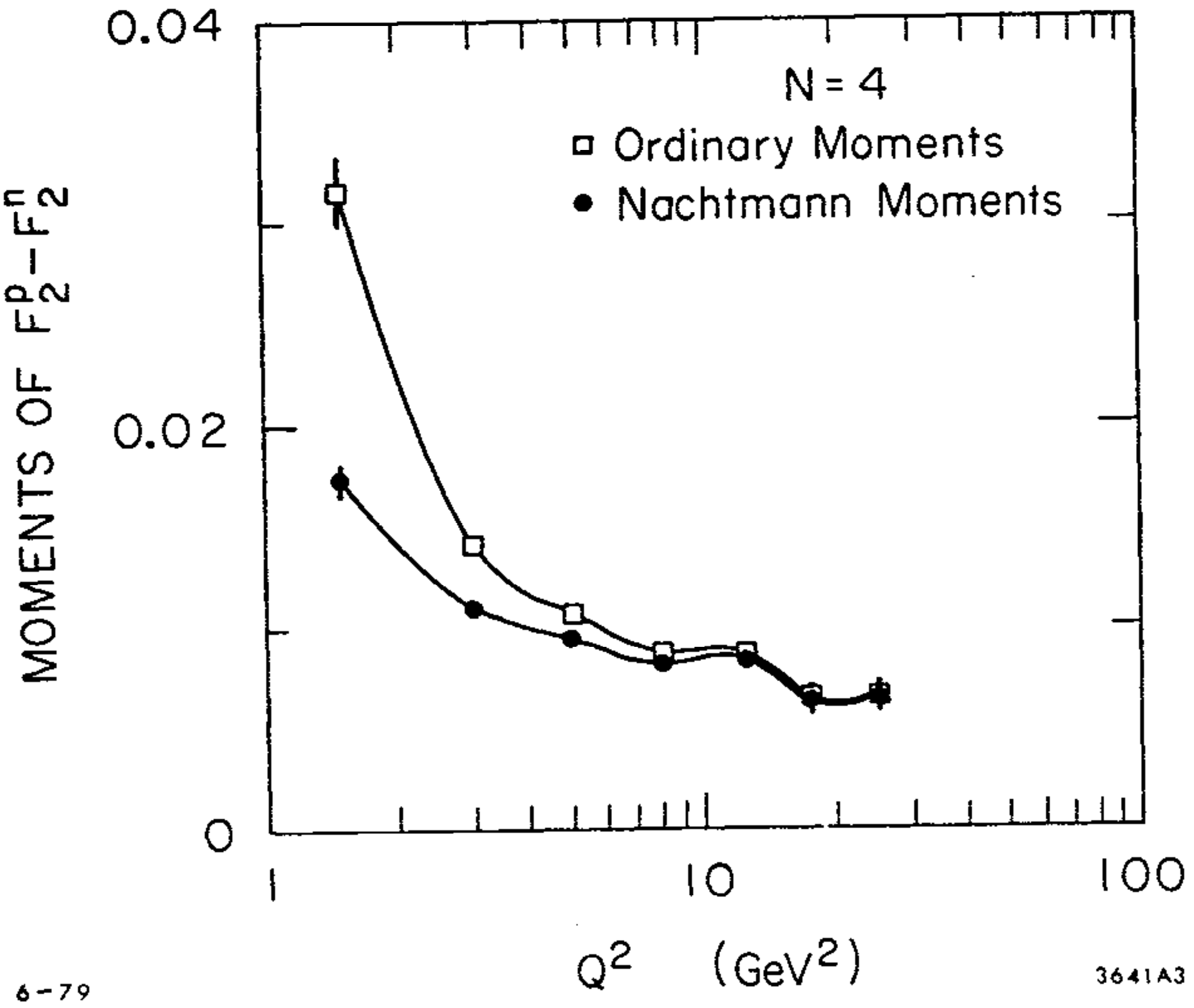

Figure 24. Comparison of Nachtmann and Cornwall-Norton (ordinary) moments for $F_2^{ep} - F_2^{en}$.

have their largest difference at high x and low Q^2). For the 9th moment a Q^2 cut even as high as 12 GeV^2 would not be considered safe by conservatives. I will adopt here a "liberal" posture and propose 5 GeV^2 for the cut in Q^2.

Effect of Fermi Motion

The next problem is the effect of Fermi motion on the moments. All of the data used in non-singlet moment analyses have these so-called "smearing" effects(4): xF_3 is measured off iron and F_2 requires both hydrogen and deuterium data. Smearing has its most pronounced effect for x near 1. Contributions from low x artifically appear at high x by way of the nucleon's motion inside the nucleus. The effect is such that as $x \to 1$, $F_2(\text{smeared})/F_2 \to \infty$. To study the consequences of smearing on the moments, I have compared the moments $F_2^{ep} + F_2^{en}$ (unsmeared) with those calculated using F_2^{ed}. The effect is small but does increase with increasing n. This means that most of the integral comes from the x region where smearing effects are small (i.e. $x < 0.8$). The conclusion is that smearing effects do not have a large influence on the results.

Contribution Due to the Resonance Region and Elastic Scattering

The next problem to consider is where the contributions to the moment integrals come from. Moment enthusiasts claim all the data (even the resonance region and elastic peak) should be included. As Q^2 increases this becomes less questionable since the low W region is squashed up against $x = 1$ and contributes little to the moments.

To illustrate what the moment integrands look like at low Q^2,(= 3GeV^2), I have plotted the Nachtmann moment integrand for F_2^{ep} (x,Q^2) in Fig. 25. Where W = 2 GeV is indicated on the graphs. Fig. 25a is for the N = 2 moment, Fig. 25b is for the N = 5 and Fig. 25c is for N = 9. The point I am stressing is that the resonance region makes a large contribution to the moment integrals at low Q^2. In this region the cross section has large exclusive final state contributions. The basis of this analysis, the impulse approximation picture of quasi-elastic quark scattering, is inadequate.

Another contribution included by moment advocates is elastic scattering. So far as I can tell the main reason for doing so is that the agreement between Eq. 86 and the data, is better when the elastic contribution is included for the low Q^2 region. Arguments that the resonance region and elastic scattering are "averaged" by the scaling curve (i.e. the old duality picture)(29) are used as justification. But one can be sure that had the moments worked well without including these contributions the arguments against including them would have been enthusiastically promoted. In any case, let's see what the fractional contribution of these regions are to the moments.

In Fig. 26a the fractional contribution of elastic scattering is shown for $F_2^{ep} - F_2^{en}$ for moments 2, 5, and 9. Again a cutoff of at least $Q^2 > 5$ GeV^2 is suggested. Below this the 9th moment has > 27% elastics and the 5th moment has > 8% elastics.

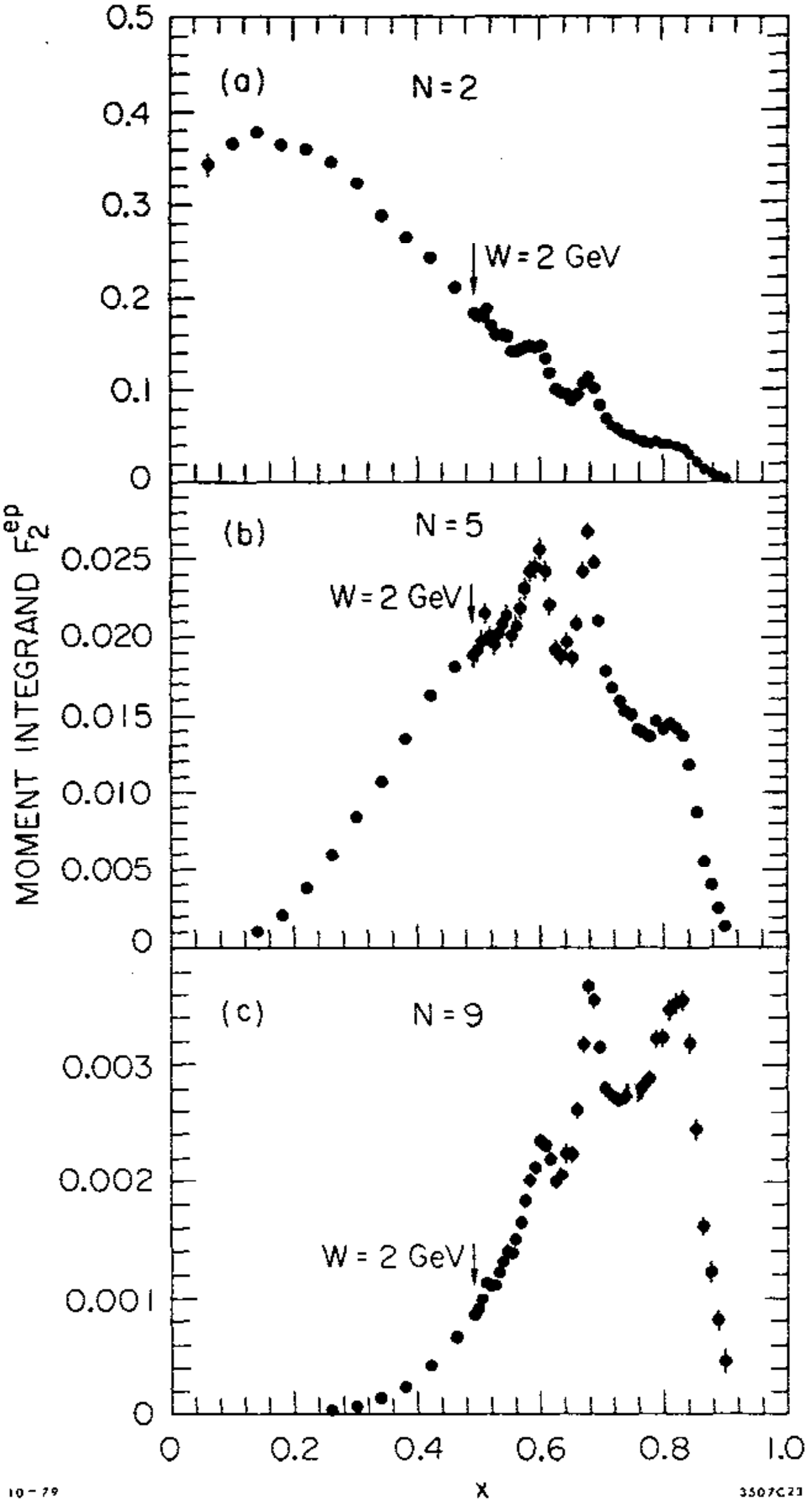

Figure 25. Nachtmann moment integrands from electron-proton scattering for a) N = 2, b) N = 5, c) N = 9 at $Q^2 = 3\ \text{GeV}^2$.

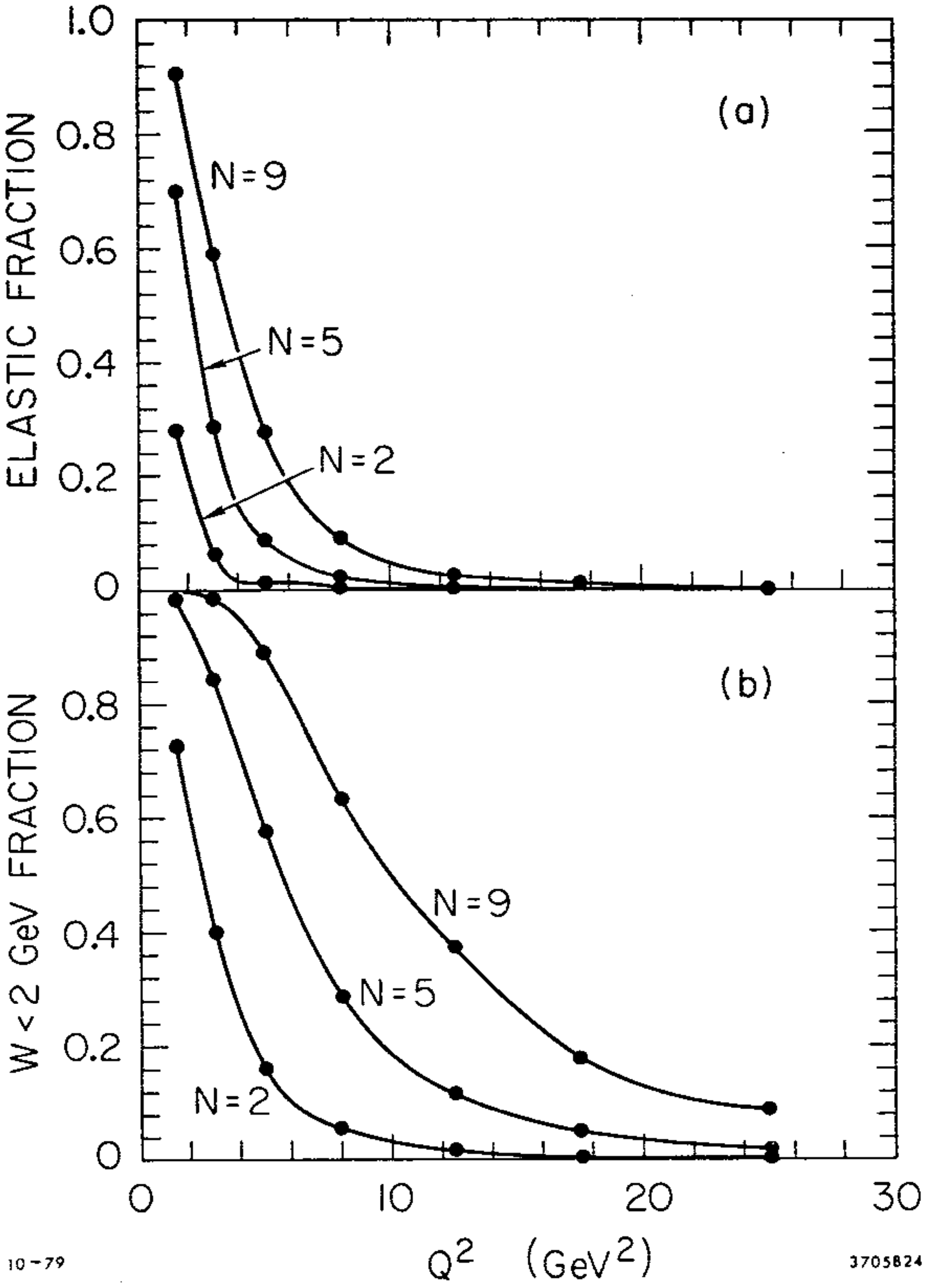

Figure 26. Fraction of n^{th} moment integral due to a) elastic scattering, and b) W < 2 GeV. The latter includes both resonance and elastic scattering.

In Fig. 26b the fractional contribution for $W < 2$ GeV is shown versus Q^2 for the same moments. This fraction includes both the elastic and the resonance contributions. If one wishes to minimize the uncertainties here, a cut of $Q^2 > 15$ GeV^2 would not be too conservative. Unfortunately, as we go to a higher Q^2 cut the data become sparse.

Contribution Due to Models for the Structure Functions

The final problem with moments is that the experiments never fully cover the x range. For those regions containing no data, a model of the structure function must be used. Clearly we don't want this model contribution to be large and in any case we should assign appropriate errors to it. Experimenters have quoted results for which the contribution to the moment of the model is less than 25%.(26) Unfortunately, sometimes the error associated with this contribution is neglected. The model should also be independent of QCD. For example a simple polynomial in $(1 - x)$ times x (or $\sqrt{x}$) fitted to each Q^2 bin could be used. Models formulated to reproduce the QCD moments and fitted globally to the data should be avoided. This "pulls" the answer closer to the QCD predictions as the model contribution to the moments increases.

Comparison with the Data

The results of two xF_3 moment analyses are shown in Fig. 27. The CDHS analysis(26) didn't include the elastic contribution, but its inclusion would change the answers very little because of the large

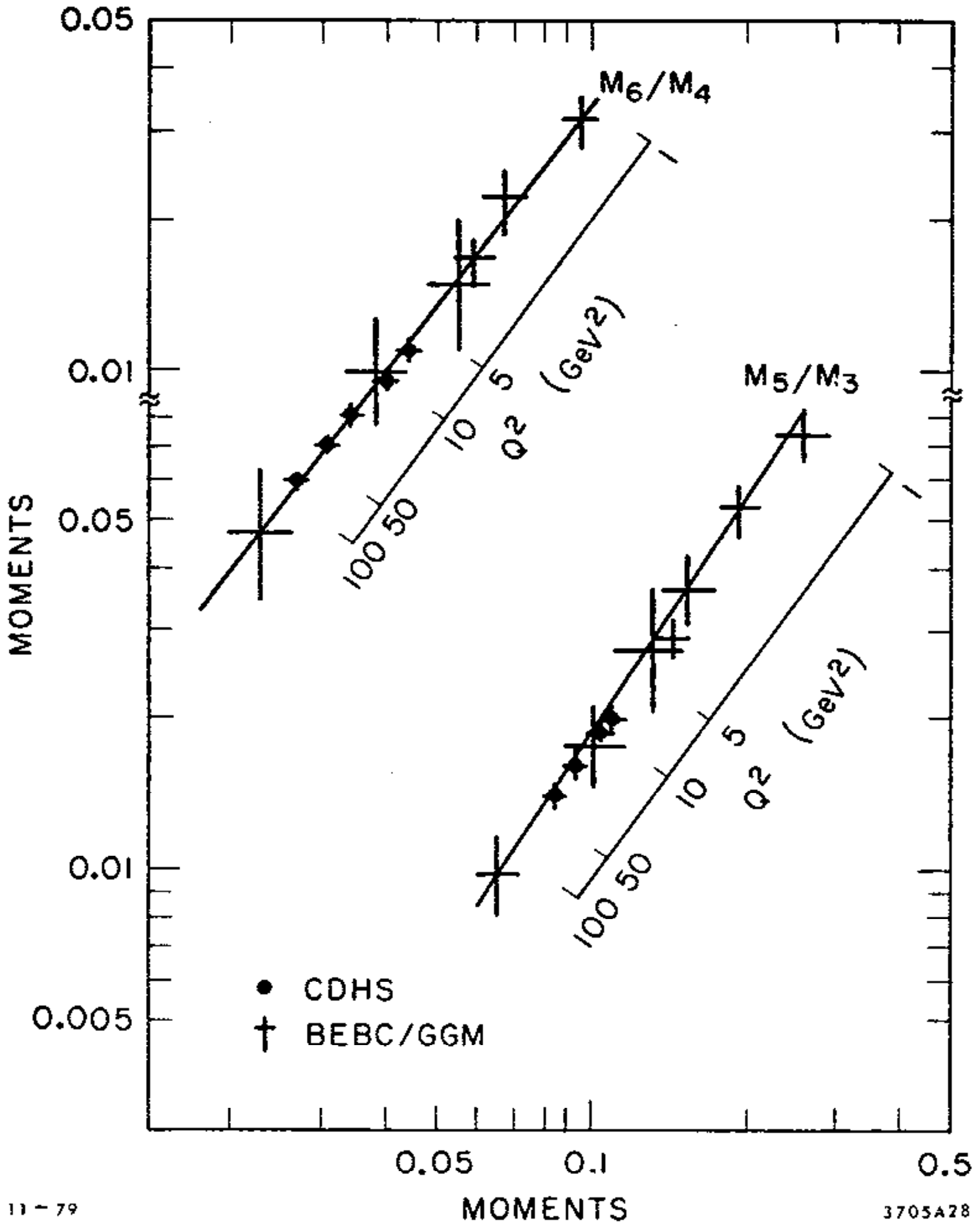

Figure 27. Moments of the xF_3 structure functions from νN scattering, plotted against each other. Solid lines show vector gluon predictions.

values of Q^2 where they report results. In the lower Q^2, high x region the CDHS experimenters have used the SLAC F_2^{ed} data times 9/5 to fill in the gap in their data. They have also used their F_2 data (instead of xF_3) for x > 0.4 because it has better statistical accuracy. They argue that for x > 0.4 the "sea" has "evaporated" and only valence quarks contribute to F_2. The slanted scales on the figure show the respective Q^2 for the CDHS data points on a $\ln(\ln Q^2)$ scale.

The data from the BEBC collaboration is also shown in Fig. 27.(30) This data has only two points with $Q^2 > 5$ GeV^2. For the reasons cited above, the data below 5 GeV^2 should be regarded with caution. Furthermore, the $\langle Q^2 \rangle$ of the highest data point is 60 GeV^2, not > 100 GeV^2 as might be inferred from the Q^2 scale.

The lines on the graphs have slopes as predicted by the ratios of the appropriate anomalous dimensions. The agreement here is impressive. Recall these slope predictions are independent of $\alpha_s(Q^2)$ (and hence the number of quark flavors) and depend only on the (vector) nature of the gluons. Scalar gluons would predict slopes closer to unity than the vector gluons and are disfavored by these results.

Using the combined SLAC(1) and CHIO(2) data, the non-singlet moments of $F_2^{ep} - F_2^{en}$ have been calculated and are shown in Fig. 28. The solid lines represent the QCD slope predictions. The data as presented seem to agree with Eq. 86.

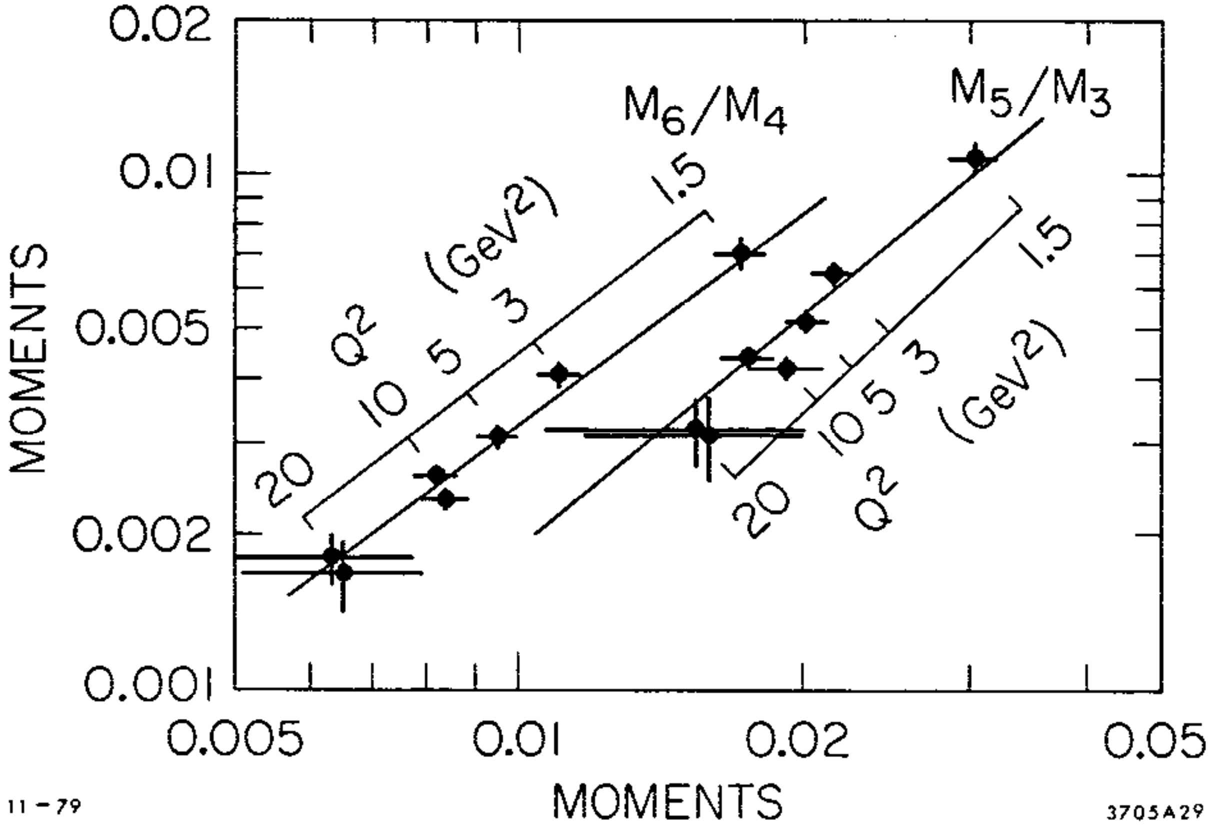

Figure 28. Moments of structure functions $F_2^{ep} - F_2^{en}$ for ep and μp scattering plotted against each other. Solid lines show vector gluon predictions.

Another way of plotting the xF_3 appears in Fig. 29(26) where $M_{NS}(Q^2,n)^{-1/d_n}$ is plotted against $\ln(Q^2)$, as suggested by Eq. 87. The intercept with horizontal scale indicates the value of Λ^2 found by the CDHS experiments.

Summary and Conclusions on Moment Method

The conclusions drawn from the moment analyses are:

1. The logarithms of the Nachtmann moments seem to obey quite well the prescription of Eq. 86 that their ratios be independent of Q^2 and equal to the ratio of the respective anomalous dimensions.

2. The consistency is seen for both neutrino scattering (xF_3) and electron (muon) scattering ($F_2^{ep} - F_2^{en}$).

3. However, when a reasonable Q^2 cut is made (e.g. $Q^2 > 5$ GeV^2), this test of QCD becomes insensitive. Only the CDHS data presently extends to high enough Q^2 with sufficient data to make meaningful comparisons.

4. It is interesting that the low Q^2 moments fall on top of the QCD prediction. But shouldn't this be interpreted as a test of the DYW relation and duality?

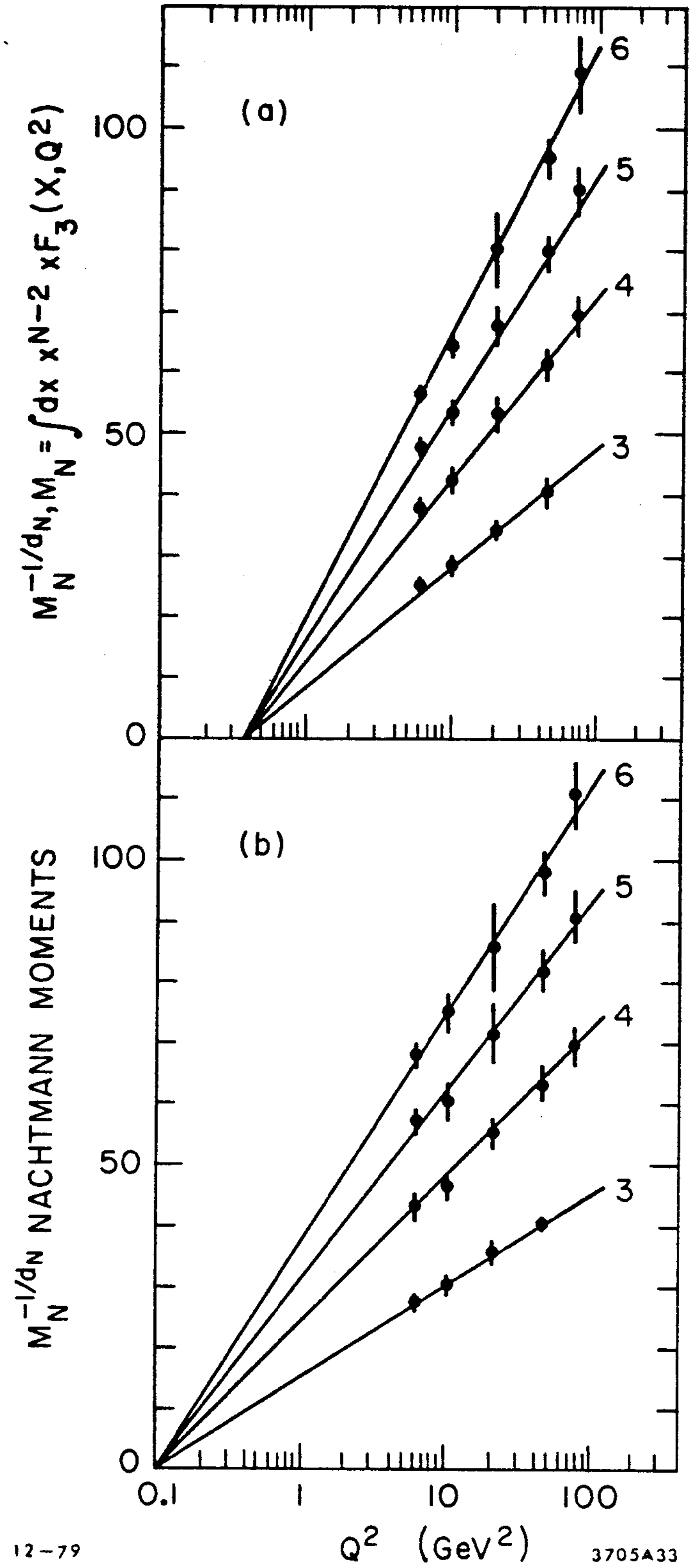

Figure 29. Behavior of xF_3 moments raised to the $-1/d_n$ power. Intercept with Q^2 axis is Λ^2.

6.3. Explicit Functional Form for $xF_3(x,Q^2)$

The problems with the moment analysis have spurred efforts to find alternatives. In this section I will discuss the Buras and Gaemers approach (22) and in Sec. 6.4 I will discuss the Abbott and Barnett(24) approach.

Buras and Gaemers (BG) set out to find an approximate functional form that satisfied the moment equations and would fit the data reasonably well. The DYW relation suggests $(1 - x)^3$ dominates at high x and Regge arguments suggest a $\sqrt{x}$ dependence at low x. The BG approach was to fit a form consistent with these power laws. Explicitly they made the ansatz that

$$xF_3(x,Q^2) = \frac{3}{B(\eta_1,\eta_2+1)} \; x^{\eta_1} \, (1 - x)^{\eta_2} \tag{90}$$

where

$$\eta_1 = \eta_{01} + \eta_{11} \cdot s \cdot \frac{4}{25} \;, \tag{91.1}$$

$$\eta_2 = \eta_{02} + \eta_{12} \cdot s \cdot \frac{4}{25} \;, \tag{91.2}$$

and

$$s = \ln\left(\frac{\ln\left(\frac{Q^2}{\Lambda^2}\right)}{\ln\left(\frac{Q_o^2}{\Lambda^2}\right)}\right). \tag{91.3}$$

where Q_o^2 is an arbitrary fixed value of Q^2. $B(x,y)$ is the Euler beta function which insures the GLS sum rule ($\int F_3 dx = 3$). The Cornwall-Norton moments, calculated with xF_3 as parameterized in Eq. 90, satisfy Eq. 82 to a few percent for the first ten moments $(2 < n < 10)$.

The advantage of using a functional form is that the entire x range is not required for each Q^2 bin. No elastic scattering contribution enters; resonance region data do not need to be included. The disadvantage is that we are now committed to an x distribution that may not fit at all well. Indeed any failure on the part of this method is easily blamed on the "arbitrary" x distribution, rather than on QCD.

Comparison with the Data

The CDHS collaboration have pursued an analysis using the BG functional form for xF_3.(30) They required that the data used in the fit have $Q^2 > 3\ \mathrm{GeV}^2$ and that $M^2x^2/Q^2 < 0.03$ (this reduces the scaling variable problem (ξ versus x) to much less than 10% for most of their data). The resulting fit is shown in Fig. 30. The fitted parameters are:

$$\eta_1 = 0.51\ (\pm\ 0.02) - (0.83) \cdot s \cdot \frac{4}{25} \tag{92.1}$$

$$\eta_2 = 3.03\ (\pm\ 0.09) + (5.0) \cdot s \cdot \frac{4}{25} \tag{92.2}$$

and

$$\Lambda = 0.55 \pm 0.15\ (\pm\ 0.10\ \text{systematic})\ \mathrm{GeV} \quad . \tag{92.3}$$

These values were found for ${Q_0}^2 = 20\ \mathrm{GeV}^2$ and the fit has a $\chi^2 = 56$ for 63 degrees of freedom. The exponents of x and (1 − x) are very close to the expected values of ½ and 3. It is interesting to note that the exponent of (1 - x), η_2, increases with increasing Q^2. Recall that this was the same qualitative behavior observed for $F_2^{ep}(\xi,Q^2)/(1-\xi)^3$ in Fig. 22c.

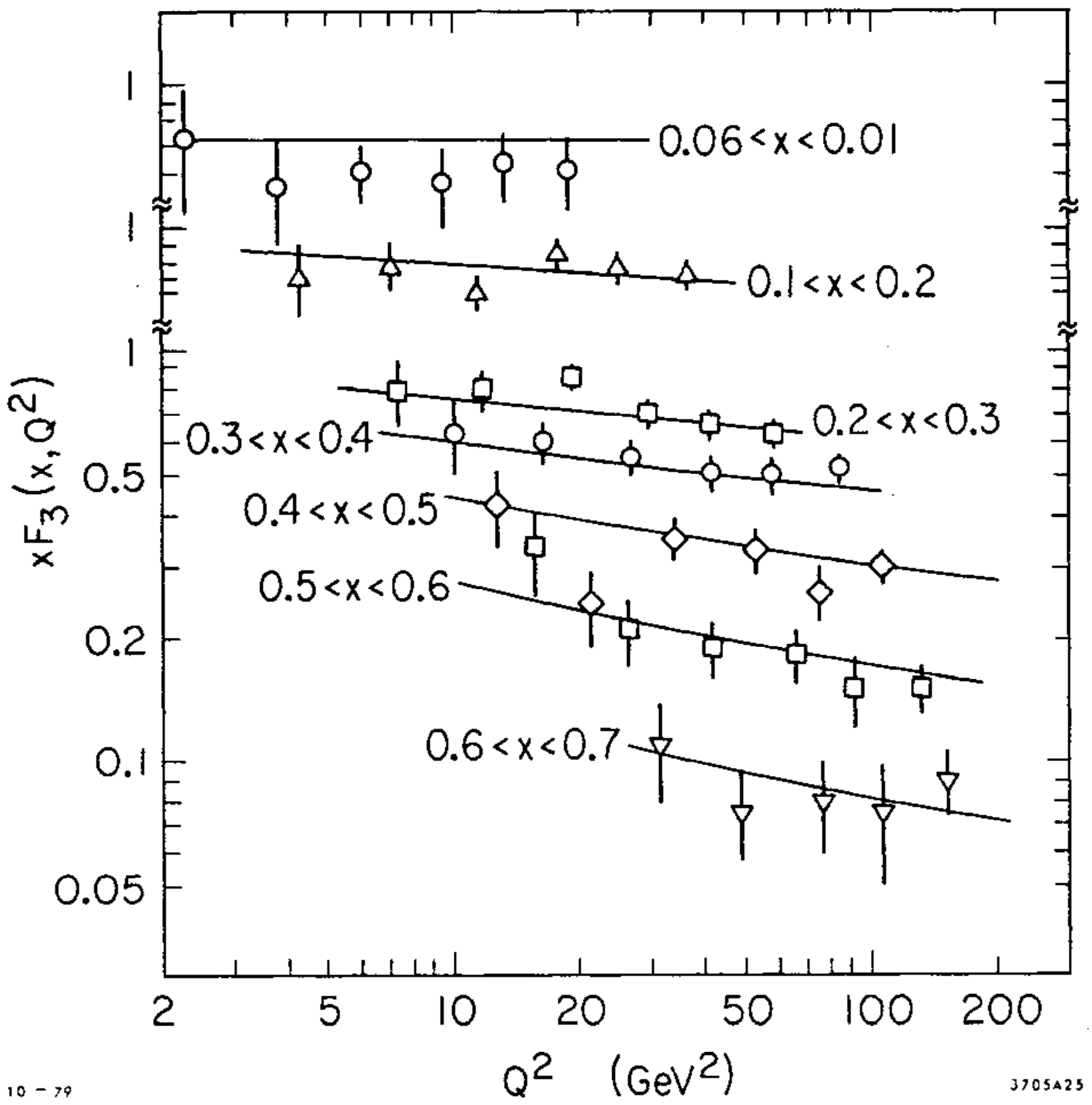

Figure 30. Method of Buras and Gaemers applied to the neutrino-nucleon structure function xF_3. Solid lines give the result of the best fit to the data.

I have tried making similar fits for $F_2^{ep} - F_2^{en}$ without success: the fits tend to be unstable. This may be because of the large number of fitting parameters.

6.4. Evolution Equation Technique

Method

Abbott and Barnett have developed a technique to test the evolution equations directly by numerically solving Eq. 73(24) for the non-singlet structure function $xF_3(x,Q^2)$. After substituting the explicit form for P_{qq} they found

$$Q^2 \frac{d}{dQ^2} \; xF_3(x,Q^2) = \frac{\alpha_s(Q^2)}{3\pi} \left\{ \left[3 + 4 \ln (1 - x)\right] \; xF_3(x,Q^2) \right.$$

$$\left. + \int_x^1 dw \, \frac{2}{1-w} \left[(1 + w^2)\left(\frac{x}{w}\right) \; F_3\left(\frac{x}{w} , Q^2\right) - 2xF_3(x,Q^2)\right]\right\} \tag{93}$$

where $\alpha_s(Q^2)$ from Eq. 39 and B from Eq. 40 are used. Given $xF_3(x,Q^2)$ at a particular value of Q^2 we can predict its value for any other value of Q^2. The form of $xF_3(x,Q^2)$ at the reference Q^2, $Q_o{}^2$, is completely arbitrary. It can be an analytic function, a "look-up" table, or anything such that when the computer asks for the value of $xF_3(x,Q^2)$ a number comes back. Abbott and Barnett chose a functional form with parameters to be determined by fitting.

So, given $xF_3(x,Q_o^2)$ the function can be "spread out" along the Q^2 axis to where the data exists (see Fig. 31). As with the BG approach this technique allows for all the data to be used independent of the particular x range associated with each Q^2 bin. No resonances or elastics need to be included. This approach has the advantage over the BG scheme in that one is not committed to an explicit form for the x distribution of the structure function. Furthermore, no approximations (to within the numerical accuracy requested of the differential equation solving routine) are made. We are simply testing the form of the integro-differential Eq. 73 as prescribed by QCD.

The form for the x distribution used by Abbott and Barnett is

$$xF_3(x,Q_o^2) = C\,x^a\,(1-x)^b \tag{94}$$

This results in a 4 parameter fit (C, a, b, and Λ). Not counting the normalization parameter C (which was fixed in the BG approach such that $\int F_3\,dx = 3$) there are 3 free parameters compared with 5 for the BG techniques.

Comparison with the Data

Both the xF_3 data from the CDHS collaboration (31) and the SLAC $F_2^{ep} - F_2^{en}$ data (32) have been fit using this scheme. The results for the neutrino xF_3 are shown in Fig. 32 and the $F_2^{ep} - F_2^{en}$ fit is shown in Fig. 33. In both cases good fits (in terms of χ^2) were obtained and the fit parameters for these non-singlet structure functions are given in Table 3.

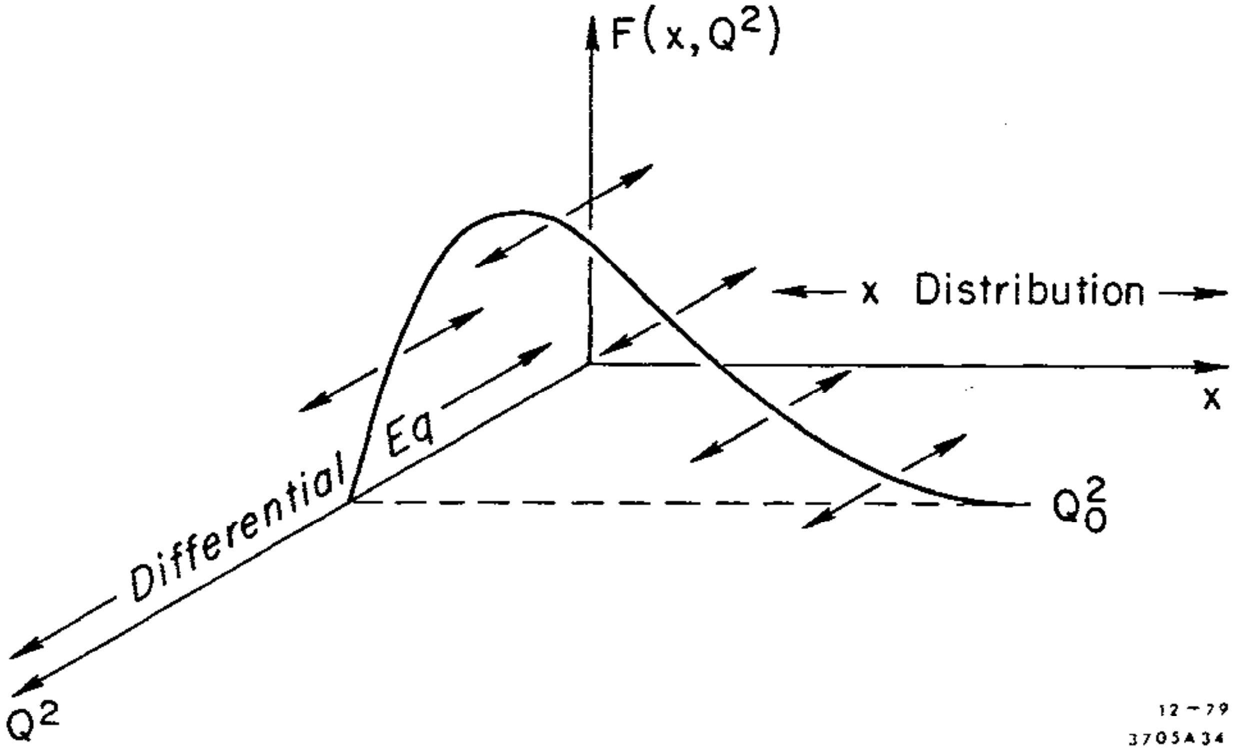

Figure 31. Method of Abbott and Barnett. Given F(x,Q^2), the QCD differential equations "spreads it out" in Q^2.

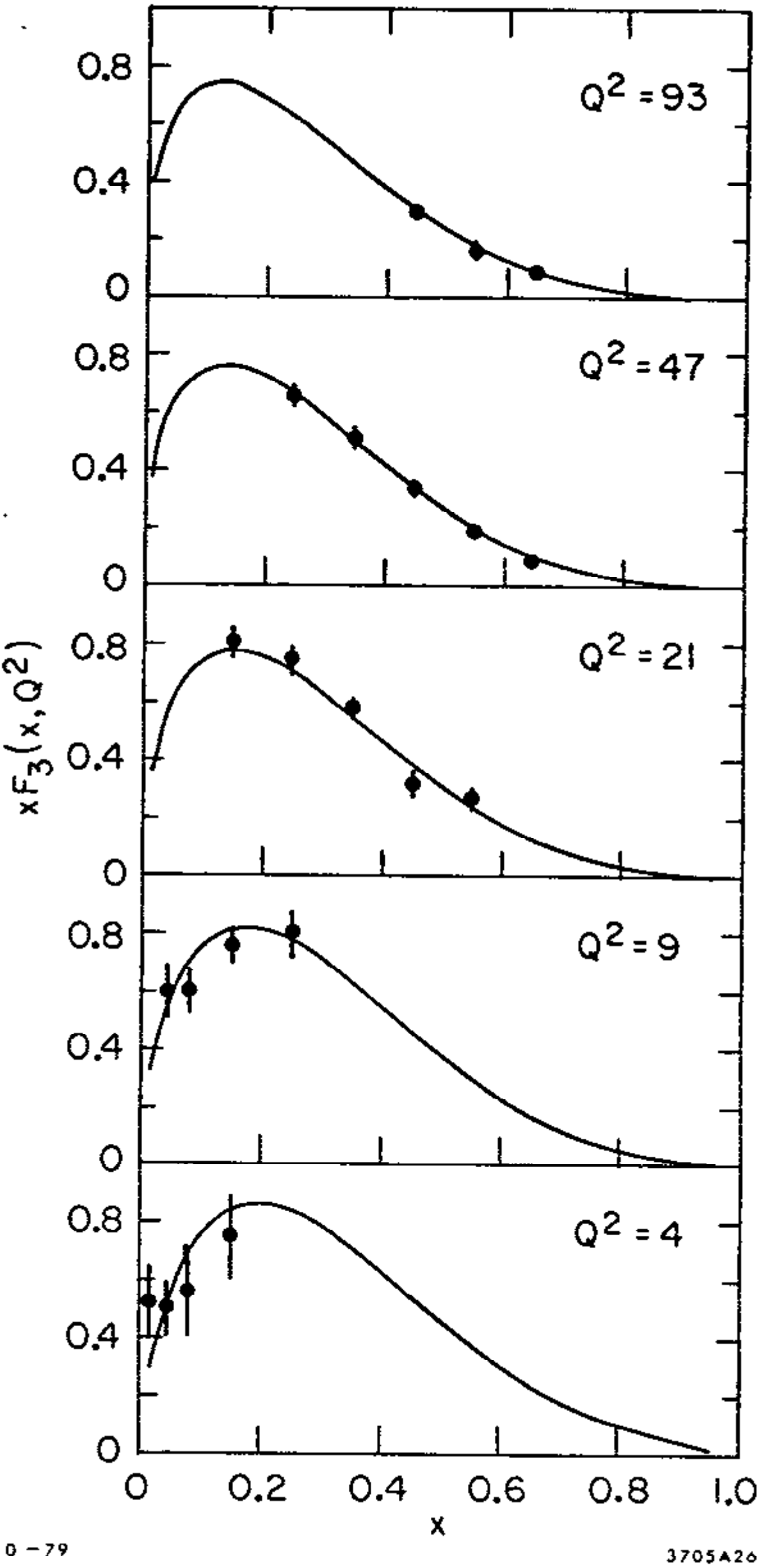

Figure 32. Method of Abbott and Barnett applied to neutrino-nucleon structure function xF_3. Solid curves are the result of the fit.

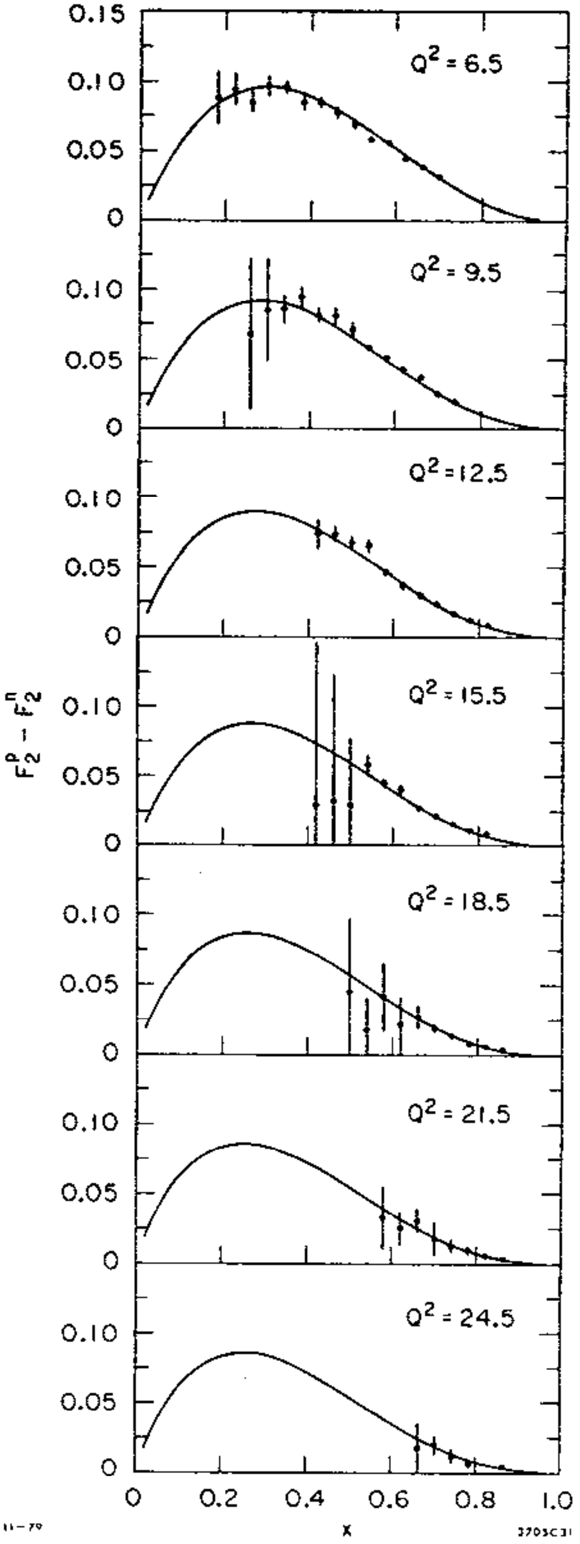

Figure 33. Method of Abbott and Barnett applied to the ep structure function $F_2^{ep} - F_2^{en}$. Solid curves are the result of the fit.

TABLE 3

Structure Function	C	a	b	Λ(GeV)	Q_o^2 (GeV^2)
xF_3	3.76	0.566	3.20	0.594	30.5
$F_2^{ep} - F_2^{en}$	0.59	0.853	2.68	0.628	30.5

Another question addressed by Abbott and Barnett was whether or not other types of "theories" would fit the data as well as QCD. In short does QCD give the best fits of all the reasonable (and unreasonable) alternatives. They found that terms that broke perfect scaling by powers of $1/Q^2$ ("higher twist" effects) by themselves were sufficient to get equally good fits as those obtained for QCD.(29,30) Hence QCD is not unique at present. Better data at even higher Q^2 might help to clarify this situation.

7. CONCLUSION

Let's now assemble in one table all the QCD tests we have seen (see Table 4). As you can see QCD has done quite well. Where it "doesn't work" the theory has many outs (elastic scattering and R). The moment analyses support the prejudice that gluons are vector particles. The lowest order bremsstrahlung effects of quarks radiating gluons does produce a pattern of scale breaking that is observed in both neutrino and electron scattering data. The low Q^2 region where scaling was first

TABLE 4

Summary of Conclusions. Conclusions from Experiments in Parentheses.

MODEL TEST	CONSTITUENT	SIMPLE QUARK	GLUON & QUARK	QCD(THEORY)
Scaling	Good Test (Works to ~ 20%)			
Ratio σ^{ν}/σ^{e} ($\frac{5}{18}$ rule)		Good Test ($\frac{5}{18}$ Consistent with data)		
GLS Sum Rule ($\int F_3 dx$)		Good Test (Data gives 3 quarks)		
Callan-Gross Relation ($r_c = \sigma_L/\sigma_T$)		Poor Test – Too much neglected (ruled out by data – but not far off)		
R_{QCD}				Poor test for Present data – neglects M^2x^2/Q^2 effects (not observed in data)
Elastic Form Factor Propagator ($G_M \sim (1/Q^2)^{n-1}$)			Good Test at high Q^2 (Works well for $Q^2 > 5$ GeV^2)	
Elastic Form Factor $\alpha_s^2(Q^2)$				Fair test at high Q^2 (not observed in data)
DYW Relation	Fair Test (scale breaking effects cloud interpretation)			
Scale Breaking Pattern			Good Qualitative test confirmed by data)	
Moments			Fair test for vector gluons (confirmed by data, but lots of assumptions)	
Evolution Equations Fitting				Good test of evolution equations (Fits data well)

observed seems to be complicated with many higher order effects entering as powers in $1/Q^2$ (e.g. the scaling variable). The future should bring forth much more definitive tests of QCD by greatly extending both the Q^2 and the x region covered by the deep inelastic scattering data.

ACKNOWLEDGEMENTS

I am grateful to Art Ogawa and Dick Taylor for their careful editing and reading of these notes, and Leon Rochester and Hobey DeStaebler for proofreading the final draft. I greatly benefited from discussions with Mike Barnett, Larry Abbott, and Mac Mestayer.

1) SLAC - MIT DATA

EXP #	θ's	Q^2(GeV^2)	x	REFERENCES
		($W \geq 2$ GeV)		
E49a	6°-10°	.05-7.9	.008-.68	J. S. Poucher *et al.*, Phys. Rev. Letters 32, 118 (1974)
E49b	18°-34°	1.0-20.	.09-.83	A. Bodek *et al.*, SLAC-PUB-1327; A. Bodek, Ph. D. Thesis, MIT LNS Report No. COO-3069-116 (1972); E. M. Riordan, Ph. D. Thesis, MIT LNS Report No. COO-3069-176 (1972)
E61	4°	.06-1.7	.01-.35	S. Stein *et al.*, Phys. Rev. D12, 1884 (1975)
E87	15°-34°	1.0-20.	.09-.83	E. M. Riordan *et al.*, SLAC-PUB-1634 (1975); A. Bodek *et al.*, Phys. Rev. D20, 1471 (1979)
E89-1	50°-60°	5.6-30.5	.32-.89	W. B. Atwood *et al.*, Phys. Letters 64B, 479 (1976); W. B. Atwood, Ph. D. Thesis, SLAC Report No. 185 (1975)
E89-2	6°-20.5°	.2-19.1	.02-.86	M. D. Mestayer, Ph. D. Thesis, SLAC Report No. 214 (1978)

These data are available from W. B. Atwood at SLAC on request.

2) H. L. Anderson *et al.*, FERMILAB-PUB-79/30-EXP, May 1979 (Submitted to Phys. Rev. D);
H. L. Anderson *et al.*, Phys. Rev. Letters 38, 1450 (1977);
H. L. Anderson *et al.*, Phys. Rev. Letters 37, 4 (1976), erratum -
H. L. Anderson *et al.*, Phys. Rev. Letters 37, 1034 (1976)

3) L. W. Mo and Y. S. Tsai, Rev. Mod. Phys. 41, 205 (1969);
Y. S. Tsai, SLAC-PUB-848, (1971);
G. Miller, Ph. D. Thesis, SLAC Report No. 129 (1971);
S. Stein *et al.*, Phys. Rev. D12, 1884 (1975)

4) Darmadi Kusno and Michael J. Moravcsik, OITS-118, (1979)
L. L. Frankfurt, M. I. Strikman, Phys. Letters 65B, 51 (1976);
Phys. Letters 64B, 433 (1976);
W. B. Atwood and Geoffrey B. West, Phys. Rev. D7, 773 (1973);
W. B. Atwood, Ph. D. Thesis (Appendix C), SLAC Report No. 185 (1975)
A. Bodek, Ph. D. Thesis, MIT LNS Report No. COO-3069-116 (1972)

5) J. G. H. deGroot *et al.*, CERN PRINT-79-0168 (1978)

6) D. H. Perkins, Proceedings of Summer Inst. on Particle Physics 1978, Pg. 16, SLAC Report No. 215

7) J. D. Bjorken, Phys. Rev. 179, 1547 (1969);
J. D. Bjorken and E. A. Paschos, Phys. Rev. 185, 1975 (1969)

8) Martin Breidenbach and Julius Kuti. Center for Theoretical Physics Publication No. 247 (1971), LNS-MIT;
O. Nachtmann, Nucl. Phys. B63, 237 (1973);
H. Georgi and H. D. Politzer, Phys. Rev. D14, 1829 (1976)

9) K. Gottfried, Phys. Rev. Letters 18, 1174 (1967)

10) S. Stein *et al.*, Phys. Rev. D12, 1884 (1975)

11) C. G. Callan and D. G. Gross, Phys. Rev. Letters 21, 311 (1968)

12) H. Deden *et al.*, Nucl. Phys. B85, 269 (1975)

13) H. D. Politzer, Phys. Rev. Letters 26, 1346 (1973);
D. J. Gross and F. Wilczek, Phys. Rev. Letters 26, 1343 (1973) and Phys. Rev. D8, 3633 (1973) and D9, 980 (1974);
A. Zee, F. Wilczek and S. B. Treiman, Phys. Rev. D10, 2881 (1974);
H. Georgi and H. D. Politzer, Phys. Rev. D9, 416 (1974);
S. Weinberg, Phys. Rev. Letters 31, 494 (1973)

14) L. N. Hand, Phys. Rev. 129, 1834 (1963);
also see Ref. 15

15) R. P. Feynman, *Photon Hadron Interactions*, W. A. Benjamin Inc., (1972)

16) A. De Rújula, H. Georgi and H. D. Politzer, Ann. Phys. 103, 315 (1977);
H. D. Politzer, Nucl. Phys. B122, 237 (1977)

17) M. D. Mestayer, Ph. D. Thesis, SLAC Report No. 214 (1978);
A. Bodek et al., Phys. Rev. D20, 1471 (1979)

18) P. C. Bossetti et al., Nucl. Phys. B142, 1 (1978)

19) Stanley J. Brodsky and Glennys R. Farrar, Phys. Rev. Letters 31, 1153 (1973)

20) S. D. Drell and T. M. Yan, Phys. Rev. Letters 24, 181 (1970);
G. B. West, Phys. Rev. Letters 24, 1206 (1970)

21) G. Peter Lepage and Stanley J. Brodsky, Phys. Rev. Letters 43, 545 (1979)

22) A. J. Buras and K. J. F. Gaemers, Nucl. Phys. B132, 249 (1978)

23) G. Altarelli and G. Parisi, Nucl. Phys. B126, 298 (1977);
also see J. Ellis, Proceedings of Summer Inst. on Particle Physics 1978, SLAC Report No. 215

24) L. F. Abbott and R. M. Barnett, Report No. SLAC-PUB-2325 (May 1979), to be published in Annals Phys.;
L. F. Abbott, Report No. SLAC-PUB-2296 (to appear in the Proceedings of Orbis Scientiae, 1979, Coral Gables);
R. M. Barnett, Report No. SLAC-PUB-2396 (1979);
L. F. Abbott et al., SLAC-PUB-2400 (1979)

25) Haim Harari, SLAC-PUB-2254 (1979) (Submitted to Nucl. Phys. B)

26) J. G. H. deGroot et al., Phys. Letters 82B, 292 (1979)

27) J. M. Cornwall and R. E. Norton, Phys. Rev. 177, 2584 (1969)

28) O. Nachtmann, Nucl. Phys. B63, 237 (1973)
" Nucl. Phys. B78, 455 (1974)

29) E. D. Bloom and F. Gilman, Phys. Rev. Letters 25, 1140 (1970)

30) J. G. H. deGroot et al., Phys. Letters 82B, 456 (1979)

31) R. M. Barnett, Private Communication

32) L. F. Abbott et al., SLAC-PUB-2400, (1979) (Submitted to Physical Review)